ELUCIDATING EXCITED-STATE DYNAMICS IN ORGANIC FUNCTIONAL MATERIALS USING STEADY-STATE AND TIME-RESOLVED SPECTROSCOPIES

by

Emma Kate Orcutt

A dissertation submitted in partial fulfillment
of the requirements for the degree

of

Doctor of Philosophy
in

Chemistry

MONTANA STATE UNIVERSITY
Bozeman, Montana

May 2025

DEDICATION

This work is dedicated to my family. I appreciate every moment of their support. You are the best part of my life, and I am indescribably happy to be yours.

ACKNOWLEDGEMENTS

I would first like to thank my advisor, Dr. Erik Grumstrup, for his mentorship and expertise. His guidance, tutelage, and support were foundational to the following work. I am incredibly grateful for the opportunity to learn from him. I would like to thank the Grumstrup group members, past and present, for their collaboration, training, and friendship. The Grumstrup group members I worked with exemplified curiosity, kindness, and encouraged me to strive for excellence during my graduate program. I would like to acknowledge my committee members, Dr. Mary Cloninger, Dr. Mike Mock, and Dr. Rob Walker. Their time and guidance shaped the research presented here profoundly.

I want to thank my family. I would first like to thank my husband, Jeremiah. He has enabled me to follow my dreams of being a scientist and a mother. His thoughtfulness and dedication to family bless my life daily. I would like to thank my children: Violet, Lily, and Bruce. They have brought me light in the darkest times and make every day a pleasure. I would like to thank my mother and father, Lara and Mark. They taught me that hard things are worth learning, a principle I have applied regularly over my graduate studies. I would also like to thank my siblings. Tom, Megan, Sam, Ben, and Spencer have shaped me into the person I am today. I would like to thank Anna Scouten. Her example and friendship inspire me.

Lastly, I would like to acknowledge all the wonderful staff and faculty at Montana State University for their encouragement, support, and collaboration.

TABLE OF CONTENTS

TABLE OF CONTENTS CONTINUED

TABLE OF CONTENTS CONTINUED

LIST OF TABLES

Table Page

LIST OF FIGURES

Figure Page

LIST OF FIGURES CONTINUED

Figure Page

LIST OF FIGURES CONTINUED

Figure Page

LIST OF FIGURES CONTINUED

Figure Page

LIST OF FIGURES CONTINUED

Figure Page

LIST OF FIGURES CONTINUED

Figure Page

LIST OF FIGURES CONTINUED

Figure Page

ABSTRACT

The chemical and structural tunability of organic functional materials (OFMs) makes them attractive alternatives to inorganic analogs for industrial applications. However, optimizing these organic systems can be difficult due to heterogeneous electronic structures, which can be traced to two main contributors. First, electronic states in organic materials exhibit intermediate delocalization, occupying a regime between molecular and semiconductor limits. Secondly, even at low concentrations, chemical and structural defects can affect the electronic structure enough to alter the measured photophysical properties of bulk materials. The variability in electronic structures from heterogeneous structural and chemical properties makes elucidating the photophysical properties of organic semiconductors extremely challenging. Nevertheless, combining steady-state and time-resolved optical techniques can help resolve the electronic characteristics and excited-state behavior in challenging OFM systems.

This work utilizes steady-state and time-resolved spectroscopies and microscopies to resolve the electronic structures and excited-state dynamics in two OFMs: graphitic carbon nitride (gCN) and a zinc porphyrin (ZnP) molecular aggregate. Chapter one introduces materials and relevant considerations. Chapter two describes the theory and the optical components of time-resolved spectroscopies used in this work. Chapters 3-5 strive towards the same goal: resolving intrinsic photophysical pathways in OFM systems before and after structural or chemical perturbation. Chapter three highlights the difficulties of extracting structure-function relationships in heterogeneous gCN photocatalysts by comparing photocatalytic degradation rates of rhodamine B to chemical, structural, and optical properties of gCN photocatalysts. Chapter four resolves ultrafast electron transfer in Ag co-catalyzed gCN by monitoring a spectral shift of Ag surface plasmon resonances. Chapter five combines ultrafast broadband transient absorption microscopy and spectroscopy to probe ZnP aggregates in solutions and thin films. These works highlight several optical approaches for deconvolving photophysics in OFMs with complicated electronic structures. We have found that gCN and ZnP systems, like many OFMs, experience variable and often rapid excited-state relaxation due to strong nuclear coupling and structural heterogeneity, which can lead to unfavorable photophysical processes. However, the photophysical limitations arising from strong nuclear coupling can be mitigated by exploiting the exquisite tunability of OFMs.

INTRODUCTION

Motivation

Organic Functional Materials

The rapid expansion of modern industry demands clean energy solutions. Organic functional materials (OFMs), also known as functional organic materials, are carbon-based compounds or structures with unique chemical and physical properties. These materials are normally conjugated and have unique photoluminescence, electroluminescence, redox activity, photochromicity, or mechanochemical properties. [1]

While OFMs are not the current industry standard for most applications, they have the potential to drive technological advancements in environmentally sustainable ways.[2] Their low cost, mechanical flexibility, low mass, and simple fabrication encourage research in OFM design and integration into many different devices, including solar cells, toys, medical equipment, electronic displays, and energy storage materials.[2-5] The organic light-emitting diode market revenue is billions of dollars yearly, with an expected total revenue of $136 billion by 2030, showcasing the huge demand for optically robust, mechanically flexible, cost-effective OFMs.[6] However, most OFMs are inherently limited by localized electronic structures created by weak monomeric interactions, chemical defects, and structural heterogeneity. In organic materials, these three characteristics counteract the long-range wavefunction characteristic of aromatic systems. Unfortunately, this dynamic relationship between localization and delocalization creates optical behavior ranging between that of a classical organic molecule and an inorganic semiconductor, creating unique technical and theoretical challenges. This work focuses on

understanding the electronic and vibrational properties of two specific OFMs to elucidate and mitigate unfavorable photophysical processes.

Photophysics

The term "photophysics" will be referenced frequently throughout this work. Photophysics describes the absorption, movement, transfer, and emission of light through a system.[7] This term references all the processes that occur during and after photoexcitation until the system returns to its unperturbed state, also called the ground state. Photophysical processes can be divided into the following categories: 1) generation, 2) evolution, 3) trapping, and 4) destruction of excited states. The illustration in Fig. 1 gives a simplified depiction of these four photophysical processes that will be individually discussed in the following paragraphs.

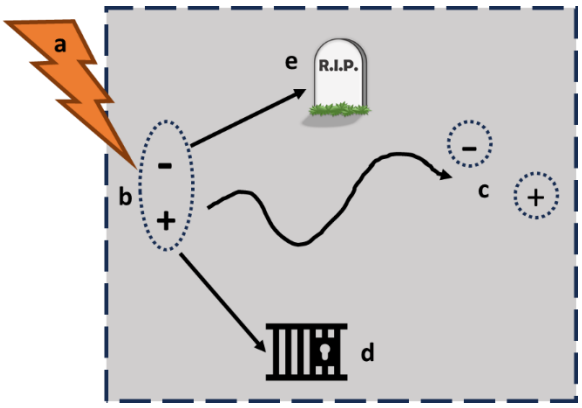

Figure 1: A generalized illustration of photophysical processes in a material (grey box). In organic materials, a (a) photoexcitation creates an (b) exciton. This exciton can evolve (c) through transport and relaxation processes, become (d) trapped, or (e) destroyed through electronic and vibrational relaxation processes.

Excited electronic and vibrational states are created when incident light is resonant with electronic transitions or vibrational modes in a material. The initial interaction between a material and light is called photoexcitation (Fig. 1(a)). The chemical structure and symmetry of

the material determine which transitions are optically allowed. Material characteristics influence which excited states are created by photoexcitation.[8] For example, photoexciting inorganic materials with large dielectric constants creates a ratio of excited states known as free charges and excitons. Photoexciting organic materials with small dielectric constants creates excitons (Fig. 1(b)). Free charges are holes or electrons whose Coulombic attraction is generally less than the available thermal energy, k_bT. Excitons are excited states comprised of a Coulombically bound electron-hole pair.[9] Predicting the concentration and nature of the excited states provides foundational insight into subsequent photophysical pathways, as well as their ultimate utility in active devices.

After photoexcitation, excited states can evolve in many different ways.[10] Excited excitonic states can transition from singlet to triplet states.[11] Two excited states can couple together to form new excited states with perturbed optical properties.[12-15] Excitons can dissociate into positive and negative charge-separated excited states (Fig. 1(c)).[16] Additionally, excited states can undergo transport through the material. These processes are often illustrated with simplified schematic models, but interpreting their experimental signatures remains challenging. On paper, modeling exciton dissociation into free charges is easy. In practice, measuring the extent of this Coulombic dissociation requires careful power studies and kinetic modeling.[17, 18]

Trapping of excited states (Fig. 1(d)) in localized defects is an important process in OFMs. Trapped excited states will eventually return to a ground state configuration. However, this trapping process can help or hinder overall device performance. In organic photocatalysts, trapping mechanisms can occur quickly (10^{-12} s), reduce the chemical potential of the system, and prevent chemical work.[19] In organic light-emitting diodes (OLEDs), efficient conversion

between emitting singlet and trapped triplet states is key for optimized device performance.[2] Identifying trapping processes is vital for choosing the application and modification schemes appropriate for intended uses.

Lastly, excited states will decay, returning the system to a pre-perturbed state (Fig. 1(e)). All relaxation processes can be categorized as radiative and nonradiative relaxation. Understanding the timescales (10^{-12} s - 10^{-3} s) of excited-state relaxation helps determine branching ratios and relaxation rates. Branching ratios describe the probability of an excited state proceeding through a particular relaxation pathway. The reaction rate quantifies how quickly the excited population transitions between two states.[17, 20] Rates and branching ratios can be elucidated through spectroscopic measurement of quantum yields, excited state spectra and lifetimes, and fractional amplitudes.

This work seeks to elucidate the photophysical processes occurring in two specific OFMs. We will now briefly describe the two material systems of interest.

Brief Introduction of Materials

This work will focus on graphitic carbon nitride (gCN) and a zinc porphyrin (ZnP) derivative. The chemical structures of both materials are shown in Fig. 2. A brief introduction of gCN and ZnP are given below.

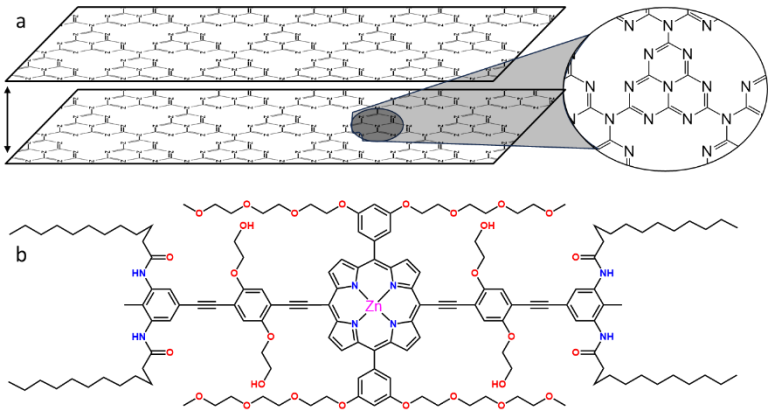

Figure 2: The chemical structure of gCN (a) and the novel ZnP derivative monomer (b) studied in this work.

Graphitic carbon nitride

Graphitic carbon nitride (gCN) is an organic semiconductor comprised of noncovalently interacting planar sheets. There are several phases of gCN, but the tri-s-triazine (heptazine) phase is the most stable under ambient temperatures and pressures.[21] The name tri-s-triazine refers to the monomer subunits comprised of three six-membered heterocyclic aromatic rings called 1,3,5-triazine. These monomer subunits are connected through tertiary amines. The optical transitions in gCN mainly arise from allowed $\pi \rightarrow \pi^*$ transitions. However, nonplanar defects are believed to break symmetry and facilitate forbidden $n \rightarrow \pi$ transitions.[19]

The chemical stability, tunability, and high redox potential of gCN make it an attractive photocatalyst.[20] However, three main intrinsic photophysical properties of gCN lead to suboptimal photocatalytic performance. The first limiting photophysical process is excited-state trapping. After photoexcitation, excitons can charge-separate and relax non-radiatively, reducing the chemical potential of the excited state.[19] The second limiting photophysical process is rapid charge recombination. After photoexcitation, an exciton can rapidly recombine on the picosecond time scale, preventing chemical reactions from having an opportunity to occur.[22] Lastly, excited

states in gCN, like other semiconducting organic polymers, have low excited-state mobility, decreasing the probability of a chemically active excited state interacting with reacting species.[23]

Metalated Porphyrins

The chemical and structural properties of porphyrins can vary greatly both naturally and synthetically, but are characterized by their identical core structure. The porphin core, originally suggested by Kuester in 1912, is made of four pyrrole-type rings joined by four methine bridges, which is referred to as the macrocycle.[24] The macrocycle follows Huckel's aromaticity rule with 26 electrons and 18 π electrons. When the porphyrin ring is complexed to a metal ion, the porphyrin is referred to as a "metalated" while porphyrin rings with hydrogens bonded to the center are referred to as "free-base." Porphyrin monomers can noncovalently interact via delocalized π orbitals and form aggregates.

Porphyrins have been studied for over a century and continue to attract heavy research attention, partially due to their biological prevalence and synthetic tunability. Their visible absorptions and high absorption coefficients make them well suited for light-driven applications such as optical sensors, energy harvesting materials, and photocatalysts.[5, 24-26] However, heterogeneous aggregation, substituents, and thin film properties have obvious effects on the optical properties of porphyrin.[11, 27] Collaborators at the University of New Mexico synthesized a novel ZnP derivative with four meta substituents (Fig. 2 (b)). These substituents combined have four unique chemical properties, including hydrophilic regions, hydrophobic regions, hydroxyl tethering sites, and large aromatic regions directly bonded to the macrocycle. This large monomer was designed to have hydrophobic, hydrophilic, and aromatic groups with reactive

hydroxyl species to facilitate anti-solvation techniques, monomeric tethering, and enhanced optical properties.

Complications in Optical Measurements

Measuring the optical properties of the two previously described systems is challenging for several reasons. Here, we will introduce the most relevant challenges to this work.

Electronic Coupling

The term "electronic coupling" refers to the coupling between the highest occupied molecular orbitals and the lowest unoccupied molecular orbitals in a material, which perturbs the energetics of the electronic states or bands of the molecular or semiconductor system, respectively.[28] The interaction between monomers is dominated by electronic coupling, (H_{ij}), where i and j refer to the two electronic states being considered. Electronic coupling can be described by the short-range (u_{short}) and Coulombic (u_{Coul}) interactions between monomers (Eq. 1.1). The short-range interactions are dependent on orbital overlap and decrease exponentially with increased interchromophore separation. The Coulombic interactions dominate over longer distances and scale asymptotically with interchromophore spacing.[29]

Eq. 1 $$H_{ij} = u_{short} + u_{Coul}$$

Strong electronic coupling can profoundly affect the absorption, emission, and excited-state properties of materials.[11, 13, 28, 30] The coupling between molecular orbitals causes the orbital energy levels to split. In organic semiconductors, stronger electronic coupling leads to larger band gap energies, and in molecular organic materials, stronger electronic coupling creates larger energetic differences between electronic states, which affects measured physical observables like

the optical absorption onsets and emission energies. Elucidating the extent of electronic coupling from physical observables like absorption and emission spectra is difficult when other properties, like chemical composition, also affect physical observables.[31]

Additionally, heterogeneous electronic coupling arises from heterogeneity in the materials. For example, chemical defects and weak π–π interactions create various structural configurations in organic materials.[13] The electronic coupling is strongly affected by orbital overlap and the distance between monomers.[29] Therefore, heterogeneous configurations between monomers and chemical defects will give rise to heterogeneous electronic couplings. Consequently, deciphering which processes give rise to a specific physical observable is difficult because a single measurement probes a superposition of electronic states with various degrees of electronic coupling.

Solvation Effects

The term "solvation effect" refers to changes in measured physical observables resulting from solute-solvent interactions. Solvents affect many measured observables in materials, including the ground and excited-state spectra, dipole moment, and absorption onset.[32] These changes can appear as solvatochromic shifts, bathochromic or hypsochromic shifts, peak broadening, or fine features.[33] Solvation effects make comparing optical phenomena of materials in different solvation environments difficult. Chapter 5 compares the optical properties of ZnP aggregates in the solution phase and solid state. In solution, the solvation environment is dominated by the dielectric properties of the solvent (See Fig. 3(a)). After crystallization, heterogeneous aggregation, air-sample interfaces, substrate-sample interactions, and trapped

solvent create complicated local dielectric environments (See Fig. 3(b)). These different solvation environments lead to differences in the ground state absorption spectra (See Fig. 3(c)).

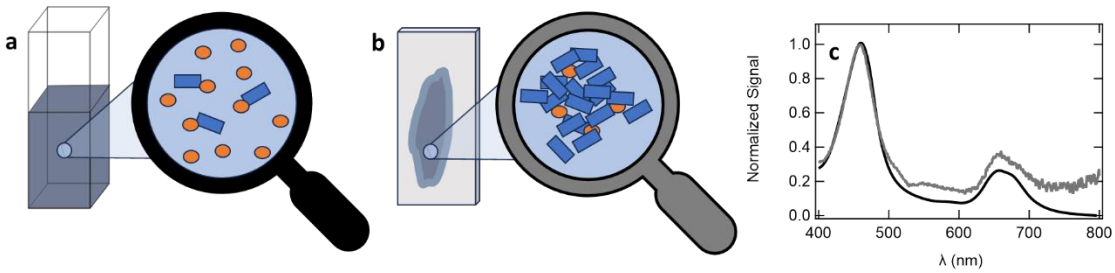

Figure 3: An illustration of different solvent interactions between solvent molecules (orange ovals) and ZnP aggregates (blue rectangles) in (a) solution and (b) thin films. The (c) ground state absorption of the liquid-phase ZnP aggregate (black) and the thin film aggregate (grey).

Light Scatter

Light scatter decreases the detected signal, which can be difficult to distinguish from absorption. Two common types of light scatter are Mie and Rayleigh scattering. Rayleigh scattering is elastic scattering off particles with diameters smaller than the wavelength of the incident light. Rayleigh scattering scales as λ^{-4}. Mie scattering is elastic scattering off particles with diameters similar to or larger than the wavelength of the incident light. Mie scattering is proportional to the square of the particle's diameter. Mie theory was developed for spheres due to the simplicity of computing scatter from a sphere compared to other geometric shapes with more real-world similarities, like irregular spheroids or cuboids. Both materials probed in this work are irregular cuboids.[34] Initial investigations evaluating the efficacy of irregular Mie scattering models indicate that the current models lack the sophistication needed to match experimental results.[34, 35]

Both gCN and the aggregated monomers scatter light, which appears as an exponentially increasing baseline at higher wavelengths in absorption spectra, as seen in Fig. 4(a). Scatter complicates measurements by shifting the apparent absorption onset of a material, which can drastically affect calculated band gaps and absorption onsets. In Ch. 3, scattering effects on the calculated optical absorption onset are extensively discussed. We observed that varying the centrifugation times used to prepare the optical samples can shift the calculated absorption onset ~800 meV, assuming direct, allowed optical transitions (See Fig. 4(b)). We hypothesize that longer centrifugation times yield a smaller, narrower size distribution of the suspended gCN colloids, suggesting that Mie scattering greatly impacts the measured absorption and calculated absorption onset of gCN.[36-38] A discrepancy of almost 1 eV could explain the disparity in reported gCN band gap energies. [36-38]

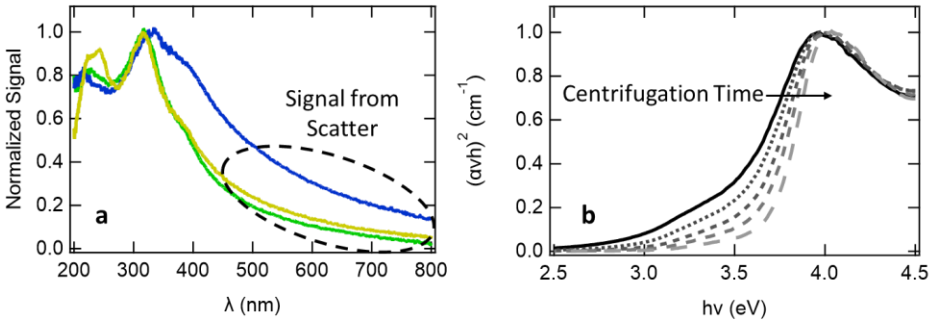

Figure 4: gCN (a) ground state absorption spectra from Ch. 3 of gCN with the signal from scattered light highlighted with a dashed oval. The blue, green, and yellow traces represent the three gCN materials studied. A (b) Tauc plot made from the absorption spectra of melamine-derived gCN assuming direct, allowed transitions. The optical samples were prepared by colloidally suspending the powdered sample in water. The centrifugation times increased from left to right.

Signal Convolution

Disentangling spectrally overlapped excited states is difficult. In Ch. 5, we resolve electronic transitions in the functionalized ZnP chromophore that are separated by hundreds of

wavenumbers with distinguishably different relaxation dynamics. However, the two optically active transitions in the Soret absorption peak are difficult to distinguish. If care is not taken, data can be analyzed in misleading ways. Figure 5(a) displays how one observed steady state absorption (black trace) can be a convolution of two absorbative transitions, indistinguishable from each other, which is very similar to the Soret band absorption discussed in Ch. 5. The red and blue states were then modeled to have unique biexponential decays, which are shown in Fig. 5(b). Kinetic traces often average over many wavelengths to assist with signal-to-noise ratios. However, if the decay traces are averaged over spectral regions with two contributing excited states (Fig. 5(b), black trace), the decay is nonrepresentative of the photophysical processes occurring in the material. Care must be taken to avoid obscuring or misrepresenting physical phenomena during data analysis.

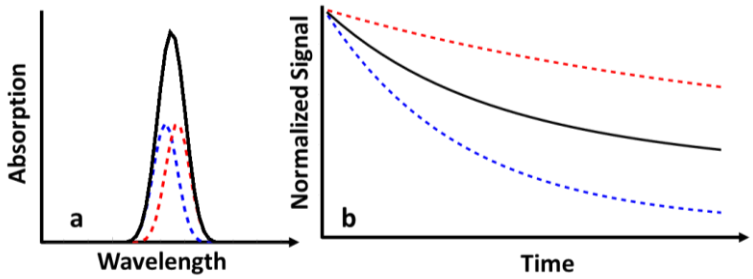

Figure 5: A representation of (a) a measured absorption spectrum (black) that convolves signal from two optical transitions (red and blue traces). If the transitions have different excited-state relaxation dynamics, the (b) kinetics traces would be different (blue and red traces). Averaging the kinetics over the whole spectral region from panel (a) would result in an average decay (black trace) that is not representative of the photophysical system.

Thesis Organization

The remainder of the dissertation will be organized in the following manner:

Chapter 2 will introduce liquid phase transient absorption (TA) spectroscopy and time-correlated single photon counting (TCSPC) spectroscopy, key time-resolved optical measurements used in this work. Chapter 3 presents a prepared manuscript correlating measured photocatalytic activity with twenty-two optical, structural, and chemical characteristics of gCN. We observe that only TA lifetimes correlate to photocatalytic activity, highlighting the complexity of photochemical and photophysical processes in gCN. The work in Chapter 4 has describes how co-catalyzing gCN with Ag nanoparticles suppresses unwanted charge recombination by facilitating electron transfer from gCN to the Ag nanoparticles. Chapter 5 presents the extensive optical characterizations performed on a novel ZnP monomer, aggregates, and thin films, elucidating changes to the structure-function relationship between the four chemically similar materials as intermolecular coupling is increased. Chapter 6 will briefly conclude the main findings and implications of Chapters 3-5.

CHAPTER TWO

METHODS AND METHODOLOGY

The next three chapters (Ch. 3-5) rely on transient absorption (TA) and time-correlated single photon counting (TCSPC) spectroscopy to measure excited-state dynamics in organic systems. Both methods are powerful tools for understanding fundamental photophysical processes. Both time-resolved spectroscopies employ femtosecond pulsed lasers to generate an excited state population and monitor the excited states as they return to equilibrium. The following section will outline the foundational theory and optical design of the homebuilt spectrometers used in this work.

Broadband Liquid-Phase Transient Absorption Spectroscopy

Theory

Liquid-phase TA spectroscopy is a nonlinear pump-probe measurement that time-resolves the evolution and decay of excited electronic states. Pump-probe measurements utilize two pulsed laser beams, the pump and probe. The pump beam creates a population of transient excited states that will decay over time. The probe beam interacts with the perturbed system at various time delays (Δt) relative to the pump pulse and is monitored with a spectrometer. The difference between the probe spectra in the presence (on) and absence (off) of the pump is taken and normalized to the pump off spectrum. Transient spectra can be plotted (See Fig. 6(a)) as the pump-probe signal (y-axis) as a function of probe wavelength (x-axis) at various time delays (different color traces).

The states of the OFMs studied in this work can be generally likened to a 3-level system. Pump-probe spectroscopy can be used to measure the relaxation of nonequilibrium excited states in a sample volume because the nonlinear pump-probe signal ($\Delta A(\omega)$) detected is proportional to the third-order polarizability ($P^{(3)}(\omega)$) and the nonlinear response (ς) of the material. This relationship is given below in Eq. 2.[39]

Eq. 2: $\Delta A(\omega) \propto -2\tilde{\varsigma}(P^{(3)}(\omega))$

The transient effect of the pump pulse on the material's polarizability can be optically observed using the broadband probe as a function of wavelength and time, allowing us to collect excited-state spectra at various time points (Fig. 6(a)) and kinetic decays at specific wavelengths (Fig. 6(b)).

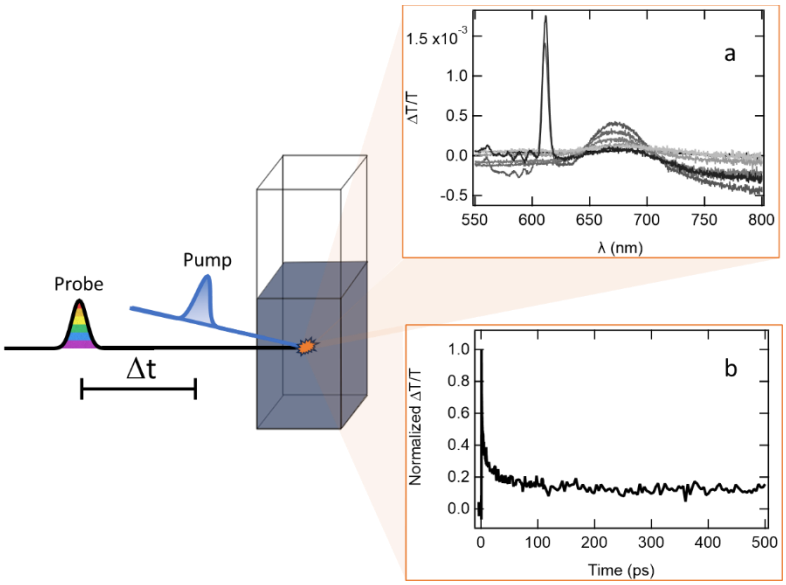

Figure 6: A generalized schematic of temporally delayed (Δt) pump and probe pulses converging in a liquid sample. Both (a) excited state spectra at various time delays and (b) kinetic decay traces taken at specific probe wavelengths can be extracted from TA measurements.

Multiple phenomena contribute to the pump-probe signal (Eq. 2). Three relevant photophysical phenomena for this work are ground-state bleaching (GSB), stimulated emission

(SE), and photoinduced absorption (PIA). Both GSB and SE increase the transmitted light through the sample. As the fraction of excited states increases, the population of absorptive ground states decreases. Therefore, the system's ground state absorption decreases, which leads to more transmitted light and a positive ΔT/T signal, which is referred to as the GSB. After the pump pulse photoexcites the sample, the probe pulse may stimulate radiative relaxation to the ground state. This process, referred to as SE, creates photons that are coherent and colinear with the probe, allowing emitted light to travel with the probe beam to the detector, resulting in a positive ΔT/T signal. The last phenomenon, PIA, decreases the transmitted light through the sample as pump-induced excited states absorb a fraction of the probe beam. A scheme illustrating these three optical phenomena is given in Fig. 7.[40]

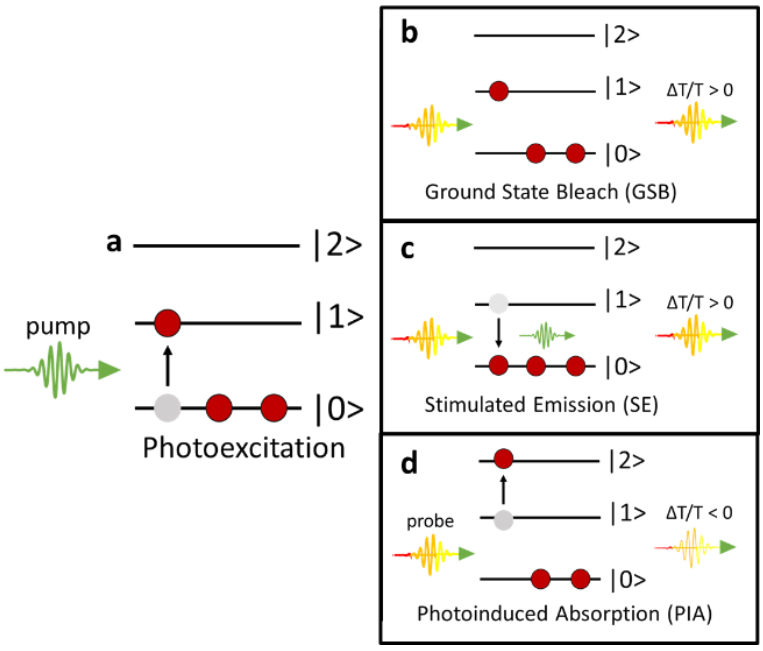

Figure 7: A scheme of how pump-probe (a) photoexcitation leads to three main transient absorption signals, including (b) ground state bleach, (c) stimulated emission, and (d) photoinduced absorption.

The y-axis of the excited state spectra and kinetics vary throughout this work from ΔA, ΔT/T, or ΔS/S, where A, T, and S are abbreviations for absorption, transmission, and signal, respectively. ΔS/S represents the normalized pump-probe signal measured and does not clarify if the probe signal results from reflection or transmission through the sample. However, ΔT/T represents the change of the probe beam transmission through the sample. In this work, ΔT/T and ΔS/S are used interchangeably and refer to the raw transmission signal collected during a TA measurement. In microscopy, scattering and reflections contribute to the detected signal, making qualitative absorption measurements difficult. However, scattering and reflection effects negligibly impact the absorption of most molecular systems. Therefore, liquid-phase TA spectroscopy can qualitatively measure the transient absorption of molecular systems. Raw transmission data were converted to ΔA in Ch. 3 to make absorptivity comparisons more intuitive. This conversion is outlined in Eqs. 3-5. The TA measurement provides ΔT/T, which can be defined as the transmission signal with the pump on minus the transmission signal of the pump off, normalized by the pump off transmission signal (Eq. 3). The relationship between absorption and transmission is given in Eq. 4 where T is the transmission through the sample and T_0 is the transmission through the optical system in the absence of the sample. The change in absorption (Eq. 5) can be written relative to pump on and off measurements using Eq. 4.

Eq. 3: $\frac{\Delta T}{T} = \frac{T_{on} - T_{off}}{T_{off}} = \frac{T_{on}}{T_{off}} - 1$

Eq. 4: $A = -\log\left(\frac{T}{T_0}\right)$

Eq. 5: $\Delta A = -\log\left(\frac{T_{on}}{T_0}\right) + \log\left(\frac{T_{off}}{T_0}\right) = -\log\left(\frac{T_{on}}{T_{off}}\right)$

The ability to transiently and spectrally resolve excited states through TA spectroscopy is an exceptionally useful tool for resolving photophysical pathways in OFM.

Optical Design

The liquid phase-TA spectrometer has undergone several design iterations, aimed at improving stability and simplifying alignment. Simplified schemes of the three main optical design iterations are shown in Fig. 8. The data presented in Ch. 3 was collected using Setup #1. The data presented in Ch. 4 was collected using Setup #2. The data for Ch. 5 was taken using Setup #2 and #3.

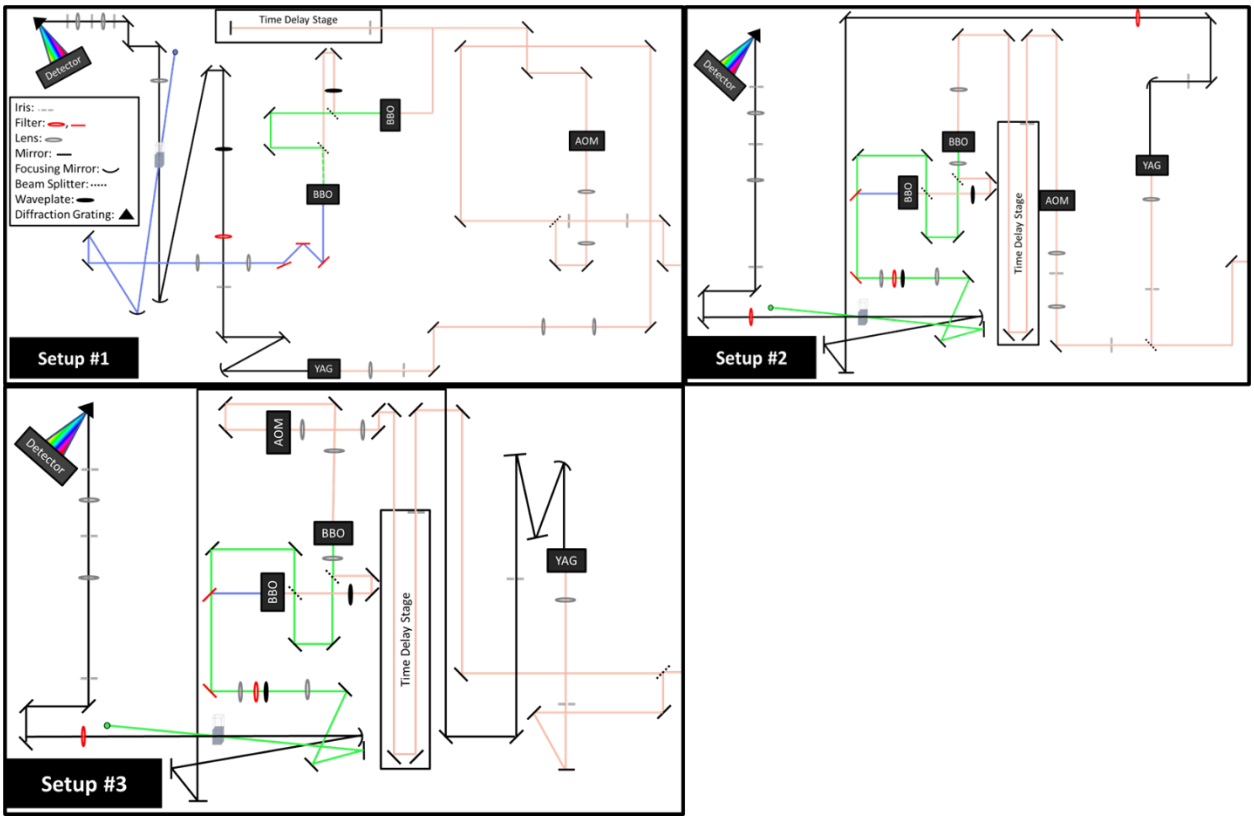

Figure 8: Three liquid phase TA table designs used. The acronyms BBO, YAG, and AOM stand for beta-barium borate, yttrium aluminum garnet, and acousto-optic modulator, respectively.

Regardless of the setup, similar optics were employed in each optical design. The pump and probe pulses were derived using a commercial ultrafast fiber laser (Coherent Monoco 1035, 40 Watt, 1MHz rep. rate, 272 fs pulse duration, 1035(±5) nm). The probe beam was generated by focusing a fraction of the 1035 nm beam into an yttrium aluminum garnet (YAG) crystal, collimating using reflective optics, beam shaping using a spatial filter, and focusing onto the sample using a 250 mm focal length spherical mirror. The other fraction of the 1035 nm fundamental was used to generate the pump beam. The pump beam was amplitude modulated using an acousto-optic modulator (AOM) at 16.125 kHz and coupled onto a 600 mm mechanical delay stage. The delay stage is used to control the delay time, Δt, between the arrival of the pump and probe beams at the sample. The AOM and delay stage configuration is modified between Setup #2 and #3 to reduce the power fluctuations measured at the sample as a function of the stage delay. The fundamental 1035 nm pulse was frequency tripled or doubled using type-I beta-barium borate (BBO) crystals. The polarization of the resultant 345 nm or 515 nm pump beam, respectively, was set to the magic angle using a broadband half-waveplate before focusing onto the sample. The intensities of the probe and pump beams were attenuated using a neutral density filter and the RF control on the AOM, respectively. The broadband probe was filtered before the sample using a 1000 nm short pass (SP) to remove the fundamental beam. After the sample, the probe was filtered using a 420 nm long pass (LP) or a 520 nm LP to remove pump scatter. The pump beam was filtered with dichroic mirrors and SP filters to remove residual 1035 nm light before exciting the sample. If third harmonic generation was used to generate a 345 nm pump beam, a wave plate was placed to change the phase of the fundamental light by 90° before recombining with the 515 nm second harmonic beam before the second BBO crystal. Using the

three systems shown above, we could tailor our measurements of specific material systems using various excitation wavelengths (515 nm and 343 nm) and spectral ranges (~500 nm to ~800 nm).

Time-Correlated Single Photon Counting Spectroscopy

Theory

Time-resolving fluorescence decay kinetics provides valuable insight into excited-state relaxation processes. Instead of monitoring the emissive decay of many excited states at various time delays like TA spectroscopy, TCSPC spectroscopy builds decay statistics from thousands of single-photon events over many cycles. A single pulsed beam is used to photoexcite the sample. The beam is kept at low enough powers that only 1 in 20 to 100 pulses result in a count at the detector. If a light pulse leads to a count on the detector, a series of electronic devices correlates the temporal change of the detector's voltage to the timing of the pulsed beam. This correlation extracts the time between photoexcitation and detected emissions (see Fig. 9). The high-repetition rate pulsed laser and electronics allow thousands of detected emission events to be measured within minutes to hours. The emission times are plotted as a histogram, and the histogram can be fitted for fractional amplitudes and fluorescent lifetimes (see Appendix A). It should be noted that emission events are random and determined by the probability of emissive decay from the excited states. Therefore, the measured histograms and calculated fits describe the probability of the system to emit.[41]

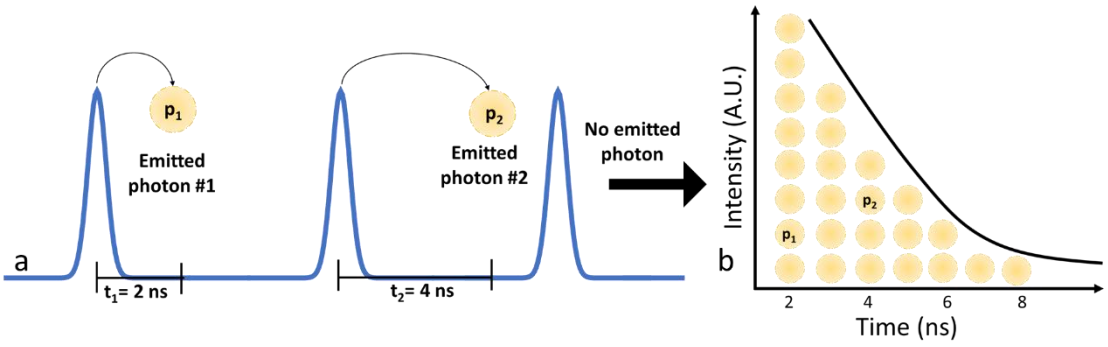

Figure 9: An (a) illustration of multiple excitation pulses (blue) leading to emission of a photon (p_x) at various times or no emission. After thousands of single-photon events, a (b) histogram of emission times is formed.

Optical Design

Samples were prepared with an optical density of ~0.1 at the highest absorption (1 cm quartz cuvette). The excitation beam was derived from a commercial Ti:sapphire oscillator (Coherent Chameleon, 80 MHz rep. rate, 85 fs pulse duration, 680-1040 nm wavelength range). The fundamental beam is then directed into a Coherent Harmonics Generator and frequency doubled or tripled using a BBO crystal to tune the excitation frequency (230 nm to 520 nm). The repetition rate of the beam was then reduced to 4 MHz using a Conoptics model 350-10 electro-optic modulator and directed onto the sample. Long pass filters were placed directly before the detector to remove excitation scatter. Collected emission travels through adjustable slits before entering a monochromator where an emission wavelength is isolated and sent to the detector. Picoquant PicoHarp 300 and FluoTime 200 software were used to control data collection. The highly tunable experimental design of our TCSPC spectrometer allows for robust time-resolved photoluminescence measurements that can help elucidate branching ratios in emissive systems.

CHAPTER THREE

CORRELATING PHOTOCHEMICAL BEHAVIOR WITH MATERIAL AND OPTICAL PROPERTIES IN GRAPHITIC CARBON NITRIDE

Contribution of Authors and Co-Authors

Manuscript in Chapter Three

Author: Emma K. Orcutt

Contributions: Synthesized materials. Collected and analyzed all the chemical, optical, and structural data. Wrote and edited the manuscript.

Co-Author: Erik M. Grumstrup

Contributions: Assisted with analysis and editing of the manuscript for final submission.

Manuscript Information

Orcutt, Emma K.; Grumstrup, Erik M.

Status of Manuscript:
☒ Prepared for submission to a peer-reviewed journal
☐ Officially submitted to a peer-reviewed journal
☐ Accepted by a peer-reviewed journal
☐ Published in a peer-reviewed journal

Abstract

The tunable structural and chemical properties of graphitic carbon nitride (gCN) provide a promising route toward tailored activity in photocatalytic applications. A primary challenge in optimizing gCN toward this end is its intrinsically heterogeneous structure, due in part to the many schemes and parameters employed in its synthesis. Varying defect types, defect densities, extent of polymerization, and degree of interplanar stacking change the catalytic, electronic, and optical properties of gCN, making robust and mechanistic interpretations of photocatalytic activity difficult with standard characterization techniques. Here we elucidate the complicated structure-function relationship of gCN by correlating photochemical activity to numerous structural, chemical, and spectroscopic characterization techniques. We find that transient absorption spectroscopy lifetimes were the only physical observable that trended with photochemical activity. These results suggest that much of the challenge to photocatalytic material optimization stems from material properties that are simultaneously perturbed when material preparation conditions are changed. In some cases, these covariant material properties have competitive influences on photocatalytic activity, making the determination of a systematic structure-function relationship challenging.

Introduction

Carbon nitrides have intrigued researchers for decades[42], with current research focused on exploring and implementing the optical and electronic properties of polymeric carbon nitrides.[43,44,45] In particular, graphitic carbon nitride (gCN) has gained significant attention due to its absorptivity of solar light and high redox potentials capable of driving photochemical

reactions, including water splitting,[46, 47] CO_2 reduction,[48, 49] and dye degradation.[50, 51] Unfortunately, unmodified gCN has not demonstrated sufficient photocatalytic activity to justify wide-scale, industrial implementation.[38] Like many other organic semiconductors, gCN is affected by strong vibronic coupling, material heterogeneity, and low quantum efficiencies, resulting in low charge mobility,[23, 52] rapid charge recombination,[22] and complicated trapping mechanisms.[19] These photophysical processes tend to immobilize or destroy redox-active excited states and limit the photocatalytic activity of gCN.[38]

To improve the photocatalytic performance of gCN, a myriad of synthetic schemes have been implemented, including varying precursor components,[50, 53, 54] changing polymerization conditions,[19, 44,55] doping gCN,[56, 57] functionalizing with co-catalysts,[20, 22, 58] and optimizing exfoliation techniques.[16, 51] While these modifications often improve catalytic performance, consistently predicting how such alterations affect catalytic performance remains challenging. For example, three recent studies compared the photocatalytic performance of gCN synthesized with urea, melamine, and dicyandiamide. A 2018 study photodegraded tylosin and found that melamine-derived gCN showed the highest catalytic performance, with a first-order rate constant of 0.0485 s^{-1} compared to dicyandiamide- and urea-derived gCN, which had rate constants of 0.0476 s^{-1} and 0.0185 s^{-1}, respectively.[54] The same year Yang et. al. photodegraded methylene blue and found that urea-derived gCN could degrade approximately 60% of the methylene blue, while melamine- and dicyandiamide-derived gCN only degraded ~30%.[51] A third study published in 2020 showed no significant difference between gCN synthesized using melamine, urea, or dicyandiamide when photodegrading rhodamine B (Rhd B) under natural sunlight.[50]

While these studies were not performed under identical conditions, the unpredictability within presumably similar material systems is striking.

Defect engineering is another strategy for enhancing the photocatalytic activity of gCN. Work by the Schlenker group found that exfoliated gCN with a higher number of edge sites exhibited lower H-production rates than a bulk/exfoliated sheet mixture. This photocatalytic improvement was attributed to improved electron transfer from the bulk gCN to exfoliated, defect-ridden gCN.[16] Other defect-focused studies have shown that defects can both improve[50, 57, 59] and reduce[31, 60] photocatalytic performance, although the mechanism by which the defects influence activity is often unclear. For example, studies have detected complicated trapping processes in gCN, but surprisingly, these trapping mechanisms are attributed to both improvement and inhibition of photocatalytic performance. [19, 44, 48, 57, 61, 62]

Typically, improved catalytic activities are correlated to changes in defect density (or type), morphology, or interfacial characteristics and supported by, for example, band gap calculations, photocurrent response, steady-state photoluminescence (PL), and (or) time-resolved photoluminescence (TRPL). However, even with careful structure-function correlations, mechanistic relationships between specific morphologies or defect types and catalytic activity remain difficult to generalize. A recent review by Mitchell et. al. compared photoactivity in gCN heterojunctions to photoluminescence and transient absorption lifetimes. The observed photocatalytic improvement was generally linked to two photophysical changes: decreased rapid charge recombination and improved charge transfer mechanisms. However, these photophysical changes sometimes present differently in presumably similar materials.[18] For example, two studies examined the emissive decay of photoinduced states at carbon dot/gCN heterojunctions

in urea-derived gCN. Both studies saw increased H_2 production and correlated improved photoactivity with enhanced charge separation. However, one study correlated enhanced charge transport rates to longer PL lifetimes[63] while the other correlated improved charge separation to shorter PL lifetimes.[64] A 2020 photocatalytic study showed that morphologically and photocatalytically distinct gCN materials have fairly comparable PL lifetimes[50] while other photocatalytic studies observe clear PL differences between materials.[57]

The link between disparate and sometimes contradictory physical observables to improved photocatalytic performance speaks to three intrinsic challenges of studying photocatalysts: 1) the complexity of the material itself, 2) the confounding effect of correlated material properties, and 3) the incomplete information provided by standard characterization techniques. For example, the effect of these three challenges can be seen when time-resolved and steady-state PL measurements are used to elucidate excited-state branching ratios. While PL spectroscopies are powerful techniques for resolving photophysical processes in quasi two-level emissive systems, these techniques provide only limited insight into low quantum yield (QY), heterogeneous materials like gCN. Additionally, defects in gCN create complicated manifolds of states below the band edge of the material.[19, 65] Varying experimental parameters like excitation energies, power densities, and power fluences can affect the branching ratios of resultant excited electronic states, which could profoundly affect the physical observables measured. Given these three considerations, the difficulty in elucidating general photocatalytic trends on specific physical observables is understandable.

To provided a systematic and robust correlation between photochemical activity and commonly available spectroscopic and structural probes, we measure the rate constants of three

gCN samples in the prototypical photochemical degradation of Rhd B. The three gCN samples are produced via thermal polymerization of melamine, urea, and a stoichiometric mixture of the two precursors. We then correlate the determined rate constants to material properties as determined by a series of common characterization techniques. Structural properties like crystallinity, interplanar spacing, and interplanar conjugation were analyzed using X-ray diffraction (XRD) and thermal gravimetric analysis (TGA). Chemical properties were evaluated using Fourier Transform-Infrared (FT-IR) spectroscopy, Time of Flight Secondary Ion Mass Spectrometry (ToF-SIMs), and elemental combustion analysis. Optical properties were determined using steady-state absorption, steady-state PL, TRPL spectroscopy, and transient absorption (TA) spectroscopy.

Surprisingly, we found that TA lifetimes were the only physical observable that qualitatively agreed with the measured trend in photodegradation rates; however, even here, the relationship is complex. Analysis of 22 individual physical observables strongly suggests that TA lifetimes and fractional oxygen content most strongly correlate to variance in catalytic activity. PL QY is weakly anticorrelated to activity, and many commonly attributed characteristics (absorption onset) show little impact on measured reaction rates. These results highlight the complex interplay between structure and excited-state branching ratio, deactivation, and reactivity in heterogeneous materials like gCN and illustrate the importance of statistical analysis tools for elucidating coupled variables.

Experimental Methods

Materials: urea (Sigma-Aldrich, ≥98%), melamine (Sigma Aldrich, 99%), methanol (Fisher Chemical, HPLC grade, 0.2 microns filtered), rhodamine-B (Signal Aldrich, analytical

standard), sodium chloride (Sigma Aldrich, ≥99%), corundum (Sigma Aldrich), and coumarin 440 (Exciton).

XgCN Synthesis: Precursors were weighed out and placed into a mortar. Both urea-derived gCN (UgCN) and melamine-derived gCN (MgCN) used approximately 12.8 g of precursor. The composite material (CgCN) used approximately 7.51g of urea and 5.26g of melamine. The precursor was ground using a mortar and pestle until homogeneous and the consistency of powdered sugar. The fine powder was then added to a ceramic crucible, covered with a flat ceramic lid, and placed in a tube furnace. The furnace was heated to 600°C using a ramp rate of 2°C/min, held at temperature for 2 hours, and then cooled to room temperature naturally. The resulting yellow product was wetted with methanol to reduce static charge before being homogenized with a mortar and pestle. The fine product was transferred to a scintillation vial, and excess methanol was evaporated using compressed air before the product was dried overnight in a 75°C oven.

Photodegradation of Rhd B: Approximately 30 mg of photocatalyst was added to 10 mL of 18 MΩ water and sonicated for 3 hours. After sonication, the photocatalyst slurry was added to 15 mL of 18 MΩ water and 50 mL of 9 μM Rhd B solution. The catalytic solution was stirred for 1 hour in the dark to prevent adsorption/desorption processes contributing to the measured photodegradation rates. After the dark time, a light source (385 nm LUXEON Z Ultraviolet LED, 3.4 $mW \cdot cm^{-2}$) was turned on, and 1.2 mL aliquots of the photocatalytic solution were taken every 0, 10, 20, 30, 60, 90, 120, 150, and 180 minutes from the start of irradiation. These aliquots were centrifuged for 4 minutes at 11,000 RPM to remove gCN particulates before the supernatant absorption was collected and used to calculate the photoreduction rates. The supernatant spectra

were background-corrected to remove scatter-related signal. Appendix A further details the baseline corrections and gives an example of non-corrected data vs corrected data (Fig. A1). This procedure was based on several previously reported studies. [66, 67]

Material Characterization: A Bruker D8 Advanced Power X-ray Diffractometer with a Cu Kα(1.54059Å) X-ray source and a LYNXEYE XE-T detector were used to collect XRD patterns. To ensure that the detected changes in 2θ resulted from crystallite differences, not variations in sample preparation, all samples were standardized with a 1:1 mass ratio of corundum (ICDD# 04-014-1368). The TGA data was collected using a commercially available thermal analyzer from TA Instruments (TGA 5500) and a high-temperature Pt sample boat. Samples were heated to 30°C (10°C/min), held for 15 min, heated to 800°C (5°C/min), held for 30 min, and cooled to 30°C (10°C/min) under a steady flow of inert gas (N_2). The FT-IR spectra were collected using a Thermo Scientific iD7 Diamond ATR in a Thermo Scientific NICOLET iS5 FT-IR spectrometer. Elemental CHNS combustion analysis was performed by Atlantic Microlab Inc. Samples were dried under vacuum at 120°C for 12-24 hours before being tested with detection limits of 0.3% and an error limit of ±0.3%; all three materials were tested in triplicate. The measured mass percent from C, N, and H were summed and subtracted from 100 to approximate the “other,” unaccounted-for mass. The ToF-SIMs measurements utilized an IONTOF GmbH model IV Time-of-Flight Secondary Mass Spectrometer to detect positively and negatively charged mass fragments created from a primary beam of Bi2+ ions. The m/z peaks were assigned to specific chemical species using IONTOF SurfaceLab 7.

Optical Sample Preparation: Approximately 2 mg of the sample was added to 5 mL of 18 MΩ water and sonicated for 3 hours. The resulting colloidal suspension was centrifuged at 1,500 RPM for 2 minutes. The final supernatant was collected and sonicated for 30 additional minutes before diluting to the needed optical density. The optical samples were either made fresh on the day or sonicated until the absorbance profile on the experimental day matched the absorbance profile initially collected during sample preparation. Aqueous samples typically lasted 4-8 days.

UV-Vis absorption spectra were collected using a commercially available UV-Vis instrument (Shimadzu UV-3101PC, 0.2 nm step size, 200 nm-800nm collection range, 1 cm quartz cuvette) and a home-built diffuse reflection spectrometer. Diffuse reflectance measurements utilized a xenon arc lamp (Shutter Instrument Company, Model LB-LS/17) to create the broadband probe beam. The incident probe and the diffuse reflectance were incident on and collected from the sample using a fiber bundle backscatter probe (Thorlabs RP22). The collected scattered light was measured using an OceanOptics USB2000+ spectrometer. Before measurement, approximately 20 mg of sample was ground with approximately 470 mg of KCl and packed in ~1 cm deep sample holder, with special care taken to smooth the powdered surface. Steady-state PL spectra were collected using a Horiba Fluorolog-3 on samples with optical densities near or below 0.1 (1 cm quartz cuvette) at their peak absorption wavelength. Time-correlated single photon counting (TCSPC) spectroscopy was used to measure the PL lifetimes of the samples prepared with an optical density of ~0.1 (1 cm quartz cuvette). The excitation beam was derived from a commercial Ti:sapphire oscillator (Coherent Chameleon, 80 MHz, 85 fs pulse duration, 680-1040 nm wavelength range). The initial beam frequency was doubled or tripled using a beta barium borate (BBO) crystal to tune the excitation frequency of

the beam. The repetition rate of the beam was then reduced to 4 MHz using a Conoptics model 350-10 electro-optic modulator. Long pass filters were placed directly before the detector to remove excitation scatter. Picoquant PicoHarp 300 and FluoTime 200 software were used for data collection, and PL lifetimes were calculated using FluoFit software.

A homebuilt broadband TA instrument was used to collect liquid-phase femtosecond TA spectra. A commercial ultrafast fiber laser (Coherent Monoco 1035, 40 Watt, 1MHz, 272 fs pulse duration, 1035(±5) nm) was used to generate pump and probe pulses. The probe beam was generated by focusing a fraction of the 1035 nm beam into an yttrium aluminum garnet (YAG) crystal, collimating using reflective optics, and focusing onto the sample using a 250 mm FL spherical mirror. The other fraction of the 1035 nm fundamental was modulated using an acousto-optic modulator (AOM) at 16.125 kHz, coupling onto a 600 mm delay stage, and frequency tripling the fundamental through a pair of type-I BBO crystals. The polarization of the resultant 345 nm pump beam was set to the magic angle using a broadband waveplate before focusing on the sample using a 300 mm FL lens. The intensity of the probe and pump beams was attenuated using a neutral density filter and the RF control on the AOM, respectively. The optical density of the colloidal suspensions ranged from 0.25 to 0.5 in a 0.2 cm quartz cuvette. Fluences were varied from 6.4 $\mu J \cdot cm^{-2}$ – 32.9 $\mu J \cdot cm^{-2}$ to ensure that TA kinetics were power independent.

Results and Discussion

Photocatalytic Performance

To compare the photocatalytic performance of the three carbon nitride materials, we monitored Rhd B photodegradation kinetics using a 385 nm LED excitation source with a flux of

3.40 mW/cm^2 at the surface of the reaction solution. Figure 10 shows the photoreaction results, with error bars indicating standard error over three individual runs for MgCN, UgCN, and CgCN. For all three gCN materials, the degradation rate appears to be constant, indicating the degradation kinetics are 0th order, as expected from the low light flux on the reaction vessel. Fits to the kinetics with a 0th-order model show that UgCN and MgCN performed similarly with rate constants of -5.3(±0.2)·10^{-8} mol·min^{-1}·g^{-1} and -4.9(±0.2)·10^{-8} mol·min^{-1}·g^{-1}, respectively. However, the photodegradation rate almost doubled to -9.0(±0.3)·10^{-8} mol·min^{-1}·g^{-1} when using CgCN as the photocatalyst.

The inset of Fig. 10 illustrates the approximate orbital alignment between gCN and Rhd B. The reduction and oxidation potentials of aqueous Rhd B at a pH of 7 are -0.76 eV and 0.74 eV (NHE), respectively.[68] The reported reduction and oxidation potentials (vs. NHE) of gCNs range from -0.18 to -1.2 eV and 1.5 to 2.0 eV, respectively.[49],[57],[46, 62, 69] While the reported bandgap for gCN varies as a function of structural phase and defect density, the bandgap of the bulk material is ~2.7 eV.[46, 52] Based on these potentials, photoexcited gCN has sufficient chemical potential to reduce and oxidize Rhd B. However, while either path toward degradation is possible, low hole mobility may decrease the likelihood of oxidation reactions.[46, 52] In keeping with previous publications studying Rhd B degradation with gCN, we attribute the observed Rhd B degradation to photoreduction driven by gCN.[50] [67]

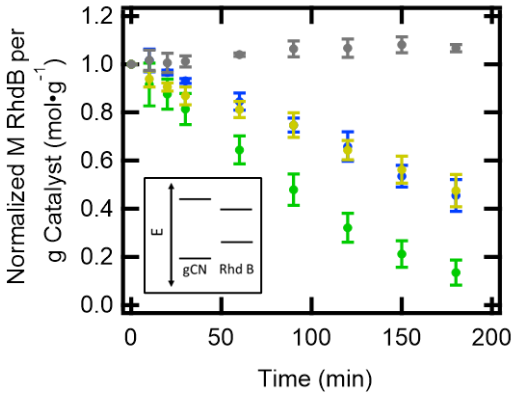

Figure 10: Plot showing the normalized change in the mol·g^{-1} during the photodegradation of rhodamine B catalyzed by MgCN (yellow), CgCN (green), UgCN (blue), and in the absence of catalyst (gray). The normalized values shown in the gray trace have not been normalized to the mass of the catalyst. The inset shows the approximate frontier orbital alignment between gCN and Rhd B.

Structural Characterization

To elucidate the origin of the observed difference in activity, we first turned to structural characterization of the three materials using XRD and TGA. Both XRD patterns and differential thermogravimetric plots can be found in Fig. 11. The XRD samples included a corundum (Al_2O_3) standard, which has a well-defined diffraction peak at 25.6° 2θ.[70] Diffraction patterns from all three bulk materials show peaks near 13.1° and 27.5° 2θ, corresponding to the (100) and the (002) planes of orthorhombic gCN, respectively. These peaks relate to the inter-pore distance between the tri-s-triazine subunits and the interplanar spacing between the gCN sheets, respectively (ICDD# 00-066-0813).[44, 62] The peak positions and the full width at half maximums (FWHMs) were calculated by fitting baseline-corrected diffraction patterns to pseudo-Voigt profiles. The differences in the intensity, FWHM, and peak position between samples are especially noticeable in the (002) diffraction peak. The fitted (002) peak positions were 27.44(±0.01)°, 27.37(±0.01)°, and 26.95(±0.03)° for MgCN, CgCN, and UgCN respectively. The

fitted FWHM of the (002) peaks were 1.54(±0.01)°, 2.16(±0.03)°, and 3.9(±0.1)° for MgCN, CgCN, and UgCN respectively. Analysis of the peak widths using the Scherrer equation indicates that peak broadening results from lattice parameter heterogeneity and not from particle size.[71] The increasing FWHMs and the lower angle (002) peak positions indicate that interplanar order decreases and interplanar spacing increases from MgCN to CgCN to UgCN. Similar effects are seen for the intraplanar peak (100), although weak signals and large backgrounds made quantitative analysis difficult. Nevertheless, the visibly more pronounced (100) peak in the MgCN and CgCN patterns is consistent with a more highly ordered MgCN and CgCN relative to UgCN in the intraplanar direction.

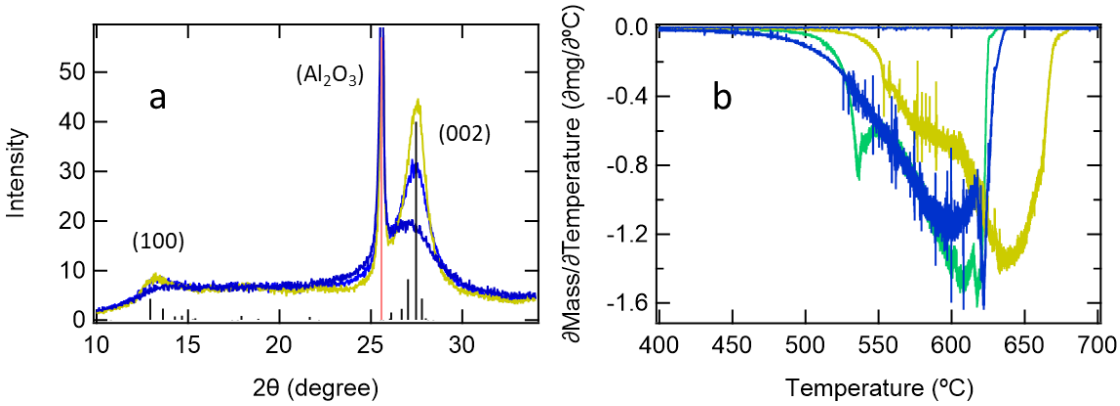

Figure 11: The (a) XRD patterns of MgCN (yellow), CgCN (green), and UgCN (blue). The red and black lines correspond to corundum (ICDD# 04-014-1368) and orthorhombic gCN (ICDD# 00-066-0813) references from the International Centre for Diffraction Data. The full XRD patterns are shown in Fig. A2. The (b) TGA plots comparing the change in mass as a function of temperature in MgCN (yellow), CgCN (green), and UgCN (blue).

The trend of increasing disorder across the series of gCNs is further supported by TGA. Panel B of Fig. 11 shows differential mass loss as a function of temperature for the three materials. Mass loss peaks at 600°C, 610°C, and 640°C for UgCN, CgCN, and MgCN, respectively. While these temperatures are broadly consistent with the decomposition of the

polymeric gCN network,[72] the mass loss at higher temperatures observed for CgCN and MgCN is indicative of materials with fewer impurities and a higher degree of polymerization.[73, 74]

Chemical Characterization

Chemical characterization of the three materials was performed using combustion analysis, FT-IR spectroscopy, and TOF-SIMs. Table 1 shows weight percentages of C, H, and N in UgCN, CgCN, and MgCN determined from combustion analysis. At first glance, the C, N, and H mass percentages do not appear vastly different between samples. However, the small percentage variations compound noticeably. This cumulative effect is seen in the "other" mass percent, calculated by subtracting the summed C, N, and H weight percentages from 100. We assume the unassigned mass primarily results from oxygen-containing defects introduced during the synthesis of the materials, an assignment confirmed by both FT-IR and ToF-SIMs. Under this assumption, UgCN contains the highest mass percentage of oxygen (6.9(±0.1)%), followed by CgCN (3.34(±0.07)%) and MgCN (1.77(±0.08)%). While melamine ($C_3H_6N_6$) does not contain oxygen, side reactions commonly include oxygen into the gCN material.[69, 73, 75] Urea (CH_4N_2O) contains oxygen and must polymerize more than melamine to form gCN.[72] Therefore, UgCN unsurprisingly contains the highest mass percentage of oxygen compared to MgCN, with CgCN falling in between.

Table 1: The average mass percentages measured using elemental analysis and calculated average atomic percents.

	Avg. Mass Percentages (± St. Dev.)				Avg. Atomic Percentages (± St. Dev.)				
Sample	C	N	H	Other	C	N	H	O*	C/N**
M	35.07(0.07)	61.56(0.01)	1.61(0.02)	1.77(0.08)	32.37(0.06)	48.73(0.01)	17.67(0.06)	1.22(0.05)	0.664
C	34.43(0.06)	60.54(0.02)	1.70(0.02)	3.34(0.07)	31.57(0.06)	47.60(0.02)	18.5(0.2)	2.30(0.05)	0.663
U	33.20(0.03)	57.90(0.03)	2.0(0.1)	6.9(0.1)	29.57(0.02)	44.22(0.08)	21.6(0.3)	4.59(0.07)	0.669

*Assuming "other" mass is from O
**ideal C/N ratio for melem ($C_6N_{10}H_6$) and gCN (C_3N_4) is 0.60 and 0.75 respectively.

The right columns of Table 1 show the calculated atomic percentages for each sample and the calculated C/N ratio. For a pristine gCN crystal, the C/N ratio is 0.75. All three samples have similar C/N ratios of 0.664, 0.663, and 0.669 for MgCN, CgCN, and UgCN, respectively. The measured XRD patterns and Scherrer analysis show that these samples consist of heterogeneous crystals with short-range order. While many local chemical structures are possible, we approximate that the shorter-range crystals are primarily comprised of melem ($C_6H_6N_{10}$), the immediate precursor to gCN. Melem, or tri-s-triazine, has a C/N ratio of 0.60. All three C/N ratios range between the ideal C/N ratios of gCN and melem, suggesting all three materials consist of melem or melem-like constitutional isomers with some degree of conjugation. The atomic percentages of H and O are highest in UgCN compared to MgCN and CgCN. Oxygen is calculated to make up 1.22(±0.05), 2.30(±0.08), and 4.59(±0.07) atomic percent, and hydrogen makes up 17.67(±0.06), 18.5(±0.2), and 21.6(±0.3) atomic percent in MgCN, CgCN, and UgCN, respectively. While these percentages do not describe local chemical structures, they indicate various amounts of oxygen and hydrogen (UgCN > CgCN > MgCN) in all samples. The increasing hydrogen percentages in UgCN and CgCN indicate less intraplanar conjugation in UgCN and CgCN compared to MgCN, corroborating the previously discussed structural characterization.

Figure 12(a) shows normalized attenuated total reflectance FT-IR spectra of all three samples. All samples exhibit a sharp peak at 807 cm^{-1} assigned to the breathing mode of heptazine units and multiple peaks around 1600-1100 cm^{-1} from the C-N stretching modes of CN heterocycles.[57] All samples exhibit a broad absorption between 2900-3600 cm^{-1} associated with primary/secondary amides and O-H stretching modes.[49] Although quantitatively resolving differences between MgCN, CgCN, and UgCN is difficult, the FT-IR spectra are comparable to previously thermally derived gCN samples and confirm the presence of amides and hydroxyl groups, as expected.

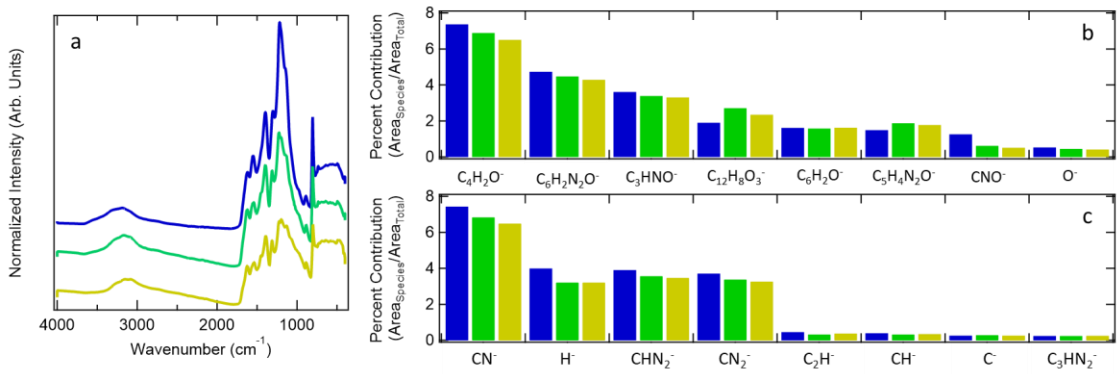

Figure 12: The (a) attenuated total reflectance FT-IR spectra of UgCN (blue), CgCN (green), and MgCN (yellow). The spectra are normalized and vertically offset to help distinguish features. A comparison of negatively charged oxygen-containing (b) and non-oxygen-containing (c) mass fragments measured using ToF-SIMs and their percentage contribution to the overall measured m/z area in UgCN (blue), CgCN (green), and MgCN (yellow). Additional fragmentation information is provided in Fig. A3 and Table A1.

Panels B and C of Fig. 12 show fragment analysis from ToF-SIMs performed on each of the three materials. While ToF-SIMs fragments do not necessarily directly reflect the composition of the bulk material, the fragmentation data can be used to understand chemical stability and composition.[76] Both positively and negatively charged fragments were measured and the full ToF-SIMs spectra are displayed in Fig. A3. We identified fragments with small m/z

ratios (<200 m/z). Species with larger m/z (>200 m/z) were not characterized due to the difficulty of meaningfully identifying larger species. All considered fragments fit well as N, C, H, and O-containing species, further justifying that oxygen accounts for the missing combustion analysis mass. Identified peaks account for 40.7%, 42.3%, and 45.2% of the total measured m/z area in the MgCN, CgCN, and UgCN spectra, respectively. This trend indicates that fragmentation of MgCN with a primary ion beam results in more fragments with higher m/z values, supporting the interpretation of XRD and TGA data that MgCN is characterized by greater intraplanar order. The eight highest contributing oxygen-containing and non-oxygen-containing species are compared in Fig. 12, panels b and c. While a clear trend is not apparent, these 16 species account for a small percentage of the total observed fragmentation area. Considering all fragments, approximately 22.3% of the detected negative fragments came from oxygen-containing species in MgCN, 23.4% in CgCN, and 24.0% in UgCN. This trend mirrors the atomic percentages of oxygen calculated from the elemental combustion analysis. Specific percent contributions from charged mass fragments are given in Table A1.

Steady-State Spectroscopic Characterization

We next turn to steady-state optical characterization techniques. Absorption spectra were collected using diffuse reflectance spectroscopy (DRS). The spectra for each material, plotted in Kubelka-Munk units, are shown in Fig. 13(a). Comparison of the spectra shows that MgCN and CgCN spectra both show a redshifted absorption onset relative to UgCN. MgCN and CgCN spectra also exhibit a subtle absorption peak near 420 nm, likely due to a more well-resolved band edge π-π^* transition.[19] In UgCN, no obvious absorption peak near 420 is present, likely reflecting increased inhomogeneous broadening relative to CgCN and MgCN.

While DRS is an effective approach for measuring the absorption onset of the bulk materials, photocatalytic reactions were performed with mechanically exfoliated gCN samples. Therefore, we also measured UV-Vis absorption spectra of exfoliated, colloidally suspended particles. These spectra are shown in Fig. 13(b). All samples show unique spectral behavior at $\lambda <$ 270 nm. Melamine and urea, the gCN precursors used in this work, absorb at $\lambda <$ 270 nm and $\lambda <$ 240 nm, respectively (Fig. A4), but are not spectrally similar to the features seen in the gCN spectra of Fig. 13(b).[77] Peak absorption features for MgCN and CgCN occur near 315 nm, whereas for UgCN, the maximum absorption occurs at 332 nm. This feature has been assigned to the π-π^* transitions within tri-s-triazine subunits.[78] [44] In contrast to the DRS data, all three spectra exhibit a distinct absorption peak near 400 nm, which we assign to the band-edge π-π^* transition, which is blueshifted (relative to DRS) likely due to size exclusion of larger particles in the suspension. All three spectra show trailing absorptivity at $\lambda > 400$ nm, which is most prominent in UgCN. We assign this spectral region to a convolution of scattering effects, n-π^* transitions, and absorptive mid-gap states[16, 79] [65] due to chemical defects. Interestingly, relative to MgCN and CgCN, sonicated UgCN suspensions easily crash out during preparation of optical samples, indicating that the UgCN suspensions are not as effectively exfoliated as MgCN or CgCN. As a result, larger particles are present in the optical samples, which cause enhanced scattering observed even out to 800 nm.

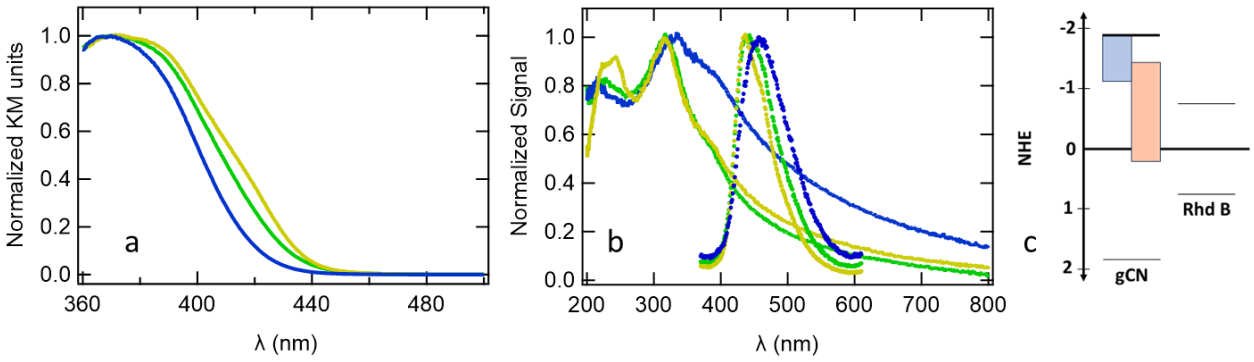

Figure 13: The steady-state absorption of MgCN (solid yellow), CgCN (solid green), and UgCN (solid blue) collected using (a) DRS and (b) transmission spectroscopy. The steady-state PL spectra of MgCN (dotted yellow), CgCN (dotted green), and UgCN (dotted blue) when samples are excited at 315 nm are overlayed with the solution-phase absorption in panel b. A (c) comparison between the oxidation and reduction potentials in gCN and Rhd B near pH 7. The boxes represent the various band edges calculated in this work, assuming indirect (orange) or direct (blue) transitions.

In keeping with common practice, Tauc plots, which assume parabolic valence and conduction bands and either direct or indirect transitions, were calculated to determine the absorption onset. Some studies suggest gCN has a direct bandgap of 1.6 to 2.0 eV,[36, 37] while other studies have shown gCN acts as an indirect bandgap semiconductor in highly condensed domains.[80] A 2019 study by Li et. al. showed that the electronic structure of gCN can be modified from a direct to an indirect bandgap through strain.[81] For this work, the absorption onsets were fit assuming both indirect and direct transitions and are shown in Table 2 for both DRS and transmissive UV-Vis measurements. The onset energy trends are noticeably different between the two collection methods. The DRS spectra indicate that MgCN has the lowest absorption onset, followed by CgCN and UgCN, respectively. However, the transmission data predict the opposite trend, with UgCN having the lowest absorption onset, followed by CgCN and MgCN, respectively. This contradiction likely stems from the differences in the measured

gCN phases. The DRS measurements are performed on the bulk, while transmission samples have been mechanically exfoliated. Indeed, the spectra shown in Fig. 13(b) were collected after 120 seconds of centrifugation; however, for all three materials, the absorption spectra systematically blueshift with increasing centrifugation time (See Fig. A5). This behavior highlights the importance of size selection in determining the apparent bandgap. We observed shifts of up to 800 meV in the Tauc-plot bandgap as centrifugation time was increased from 30 s to 480 s. Fig. A5 shows Tauc plots of the MgCN, CgCN, and UgCN samples for centrifugation times between 30 and 480 seconds, and Table A2 summarizes the absorption onsets from these spectra.

Table 2: The calculated absorption onsets from absorption data assuming indirect and direct transitions.

	Direct, allowed (eV)		**Indirect, allowed (eV)**	
	DRS	Transmission*	DRS	Transmission*
M	2.97 ± 0.04	3.58 ± 0.04	2.6 ± 0.1	2.95 ± 0.08
C	2.99 ± 0.03	3.558 ± 0.008	2.74 ± 0.06	2.95 ± 0.01
U	3.04 ± 0.02	3.30 ± 0.04	2.83 ± 0.04	2.3 ± 0.2

*Samples prepared with 120 seconds centrifugation time.

Normalized steady-state PL spectra, collected after 315 nm excitation, are shown in Fig. 13(b). The emission bands peak near 435 nm, 440 nm, and 455 nm for MgCN, CgCN, and UgCN, respectively. The red-edge emission noticeably red-shifts between samples and trends accordingly: MgCN < CgCN < UgCN. This shift may correlate to a change in the optical band gap of the material or emission from lower-energy crystallite domains and defects. The PL quantum yield (Φ_{PL}) at 315 nm is 2.10% (MgCN), 1.47% (UgCN), and 1.05% (UgCN). The Φ_{PL}

was also calculated at several lower-energy excitations (330 nm, 380 nm, and 400 nm). All the calculated Φ_{PL} are shown in Table 3 and given as percentages. Regardless of the sample, the Φ_{PL} monotonically decreases as the excitation wavelength is redshifted, suggesting that lower energy excitation increasingly excites defect sites that rapidly quench photoluminescence. Time-resolved PL, shown below, is consistent with this quenching mechanism.

The photoreduction QY (Φ_{PR}) of Rhd B, also referred to as apparent QYs, for MgCN, CgCN, and UgCN, are 0.49(±0.01)%, 0.80(±0.07)%, and 0.5(±0.1)%, respectively (see Table 3). The Φ_{PL} computes the ratio of absorbed photons vs. emitted photons at particular frequencies. The Φ_{PR} computes the ratio of absorbed photons vs. the concentration of photodegraded Rhd B. When comparing the Φ_{PR} to the Φ_{PL} near the photoreduction energy used in this work (380nm), the Φ_{PR}:Φ_{PL} ratios are 0.33, 0.85, and 0.65 for MgCN, CgCN, and UgCN, respectively. In all cases, the Φ_{PR} is lower than the measured Φ_{PL}, strongly suggesting that radiative excited states are not predominantly responsible for photocatalytic activity. Further details of the Φ_{PL} and Φ_{PR} calculations are given in Appendix A (Eq. A1 and Eq. A2, respectively).

Table 3: The photoluminescence percent quantum yields of gCN samples as a function of excitation wavelength and the photocatalytic quantum yield calculated from the photodegradation of Rhd B.

Sample	$\%\Phi_{PL\ (315nm)}$	$\%\Phi_{PL(330nm)}$	$\%\Phi_{PL(380nm)}$	$\%\Phi_{PL(400nm)}$	$\%\Phi_{PR(385nm)}$
MgCN	2.10	1.91	1.48	0.74	0.49 ± 0.01
CgCN	1.47	1.24	0.94	0.52	0.80 ± 0.07
UgCN	1.05	0.98	0.77	0.50	0.50 ± 0.1

Time-Resolved Optical Characterization

Figure 14 summarizes TRPL measurements performed on aqueous MgCN, CgCN, and UgCN suspensions. Regardless of excitation or emission wavelength, all PL decays showed multiexponential behavior, confirming that relaxation occurs heterogeneously through a manifold of relaxation pathways. Figure 14(a) shows representative PL decay traces at 460 nm after exciting at 315 nm.

Figures 14 (b-d) compare PL amplitude-averaged lifetimes ($\langle\tau\rangle$) after fitting decay kinetics for the three materials with a multi-exponential model. Panel B shows $\langle\tau\rangle$ after 315 nm excitation, with panels C and D presenting $\langle\tau\rangle$ for 360 nm and 400 nm, respectively. Note that we use a multiexponential fit as a convenient means to calculate an average lifetime for comparative purposes and not necessarily to describe any underlying distribution of lifetimes. Fits to kinetic data using models that explicitly account for underlying densities of states[19, 23] or sub-populations[16] can provide meaningful physical insight into the heterogeneous excited state decay pathways relevant to this complex system. Here, we use the kinetics as a comparative tool for quantifying average PL lifetime differences only. When excited at 315 nm or 360 nm, MgCN has the longest amplitude-averaged PL lifetime, and UgCN has the shortest amplitude-averaged PL lifetime, regardless of the monitored emission wavelength (Fig. 14(b,c)). Although PL lifetimes are generally shorter for lower redder excitation wavelengths, no outstanding PL lifetimes trends (Fig. 14(d)) that correlate to observed catalytic yield emerge from the single-method comparison.

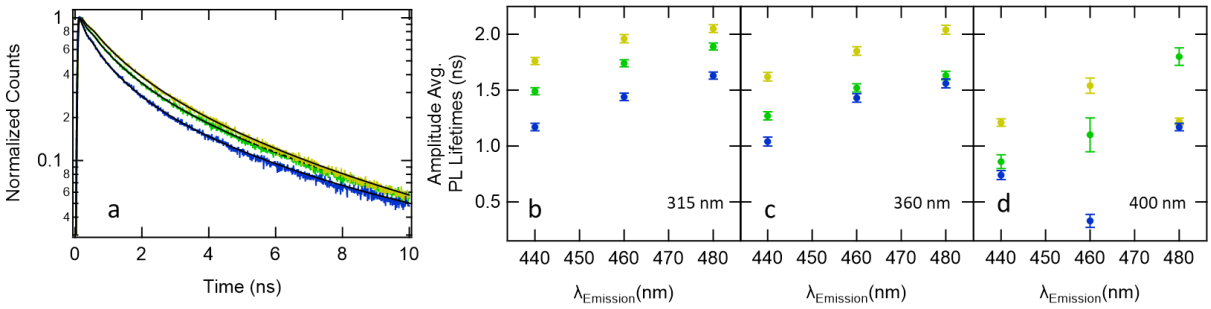

Figure 14: The (a) PL decay of MgCN (yellow), CgCN (green), and UgCN (blue) measured using TCSPC spectroscopy and the corresponding tri-exponential fits (black) calculated using FluoFit software after exciting at 315 nm and detecting at 460 nm. A comparison between the amplitude-averaged PL lifetimes as a function of emission wavelength using a (b) 315 nm, (c) 360 nm, and (d) 400 nm excitation.

Figure 15 summarizes broadband transient absorption data collected on the aqueous suspensions of MgCN, CgCN, and UgCN. Directly after photoexcitation (Panel A) with a 345 nm pump beam (28.3 $\mu J \cdot cm^{-2}$), the excited-state spectra of all samples show a broad photoinduced bleach (PIB) and a lower energy photoinduced absorption (PIA), which persist over the 2 ns scan duration. Figure 15(b) shows wavelength-averaged kinetics of the PIA between 860 nm and 880 nm, a spectral region previously assigned to photogenerated electrons and holes.[16, 19, 82, 83] The kinetics decay with a fast lifetime of 73.19(±9.78) ps, 78.40(±6.19) ps, and 75.21(±7.83) ps while the longer lifetimes component fitted to 747.6(±59.2) ps, 1083(±104) ps, and 720.4(±81.3) in UgCN, CgCN, and MgCN respectively. Although the longer lifetime component suggests a small difference between samples in the longer lifetime component, qualitative comparison of the kinetics in panel B shows no clear difference within error.

On the blue side of the spectrum, the PIB signal likely stems from a combination of stimulated emission, ground-state bleaching, and photoinduced reduction in scattering. Averaged kinetic traces from 550 nm to 570 nm are shown in Fig. 15(c). Here, clear differences between the three

samples are evident, particularly at early times. The decays were fit with a double exponential with an X offset and used to calculate amplitude-averaged lifetimes. The average lifetimes of UgCN, CgCN, and MgCN are 1508 (±238) ps, 1703 (±730) ps, and 492 (±78) ps, respectively. Table A3 summarizes fit-determined parameters for the kinetics shown in Fig. 15(b) and (c).

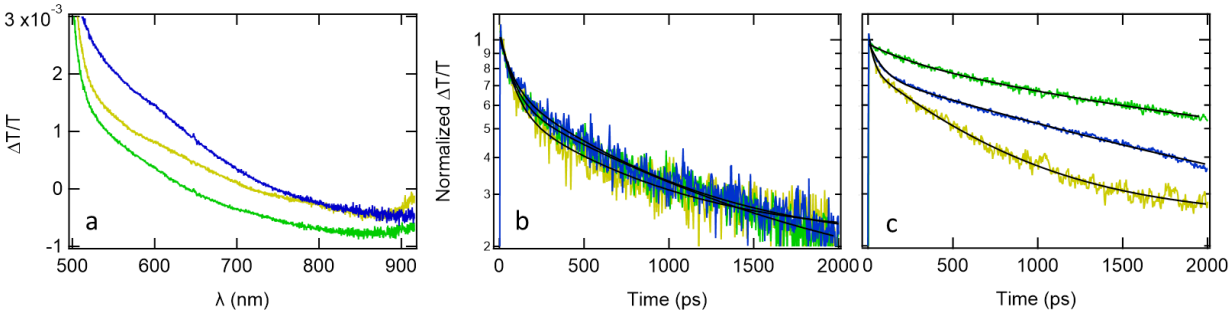

Figure 15: Excited state (a) spectra directly after excitation and excited state kinetic traces of the (b) absorptive feature from 860 nm-880 nm and the (c) transmissive feature between 550 nm-570 nm, respectively. The fits of the decay traces are shown in black, and data from MgCN, CgCN, and UgCN are shown in yellow, green, and blue, respectively.

Discussion

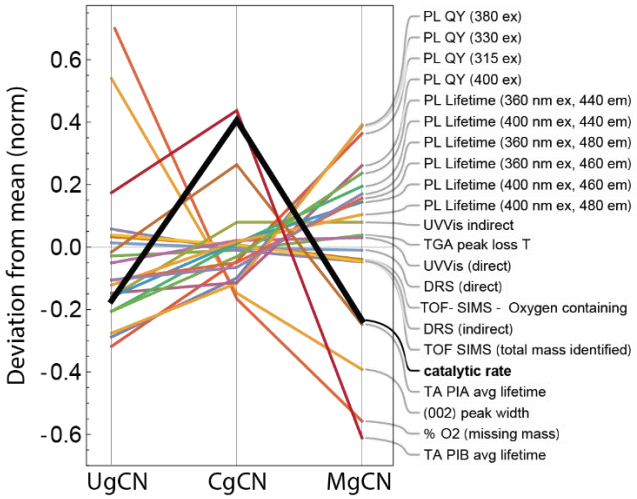

Figure 16: A comparison of the derivation from the normalized mean for all 22 physical observables measured.

The correlation of physical characterization methods to the photocatalytic performance of gCN is essential for developing a mechanistic understanding of the catalytic process, as well as providing a rational strategy toward material optimization. Figure 16 summarizes the correlation of 22 individual physical observables with the measured catalytic rate. A key finding is that the only method that provides a similar qualitative trend to the observed photocatalytic rate is TA PIB lifetimes. Below, we discuss catalytic activity within the context of the various characterization methods.

Structural Correlation

XRD and TGA results indicate that MgCN has the fewest structural defects and the highest degree of polymerization, followed by CgCN and then UgCN. How might structural (dis)order affect photocatalysis? One important structure-determined process relevant to photocatalysis is charge transport. Charges (or excitons) must migrate from the site of generation to the site of reaction, where the substrate is adsorbed. In gCN, smaller interplanar distances are hypothesized to improve the electronic overlap of π-orbitals between adjacent sheets, increase the mobility of excited states, and promote photocatalytic activity as more active species reach the catalyst surface. For example, Merschjann et. al. fit TRPL and TA data to rate equations to elucidate hopping rates, random walk lattice dimensions, mobility, and absorption coefficients. By comparing modeled results with experimental data, these authors showed that electronic transport in gCN is dominated by 1D interplanar transport with small contributions from intraplanar or intrachain transport.[23] Huda et. al. found that electrons and holes are highly localized on C and N atoms and that excitons are spatially confined, suggesting that intraplanar mobility of excited states is slow.[52]

Based purely on the argument that more ordered materials will exhibit faster transport, we would expect that MgCN should show the highest photocatalytic ability compared to CgCN and UgCN. This trend in activity is not observed (Fig. 16), reflecting the challenge in interpreting photocatalytic rates within the context of highly correlated material properties. For example, while intraplanar order might be weakly correlated to activity because intraplanar transport in gCN is slow, greater intraplanar order also implies that fewer edge sites (per mass) are available. Edge sites may be detrimental to activity because edge-localized trapping could result in low mobility and rapid charge recombination.[23, 52, 84] Edge sites could also plausibly be advantageous, as both substrate adsorption and electron transfer are likely to be more favorable in regions where the electronic structure has large gradients.

Chemical Correlation

In principle, chemical analyses can provide important insight into the active site concentration in gCN. Both N- and O-defect densities in gCN have been correlated to improved photocatalytic performances.[57, 59, 60, 62, 65, 85] Defects cause red-shifted optical absorption onsets, slow recombination processes, and provide local sites of enhanced reactivity. Katsumata et. al. suggest that photogenerated electrons delocalize at N-defects and O-replacement sites, preventing rapid charge recombination and increasing catalytic activity. They also suggest that cyano groups effectively separate and transfer photogenerated charge carriers to the surface of the catalyst, where photochemistry normally occurs.[57] Using density function theory, Tu et. al. found that N-vacancies form mid-gap states under the conduction band, broadening the optical absorption onset to lower energies. At intermediate defect concentrations, N-vacancies were found to improve H_2 evolution and CO_2 reduction due to extended visible light absorption,

increased trapping processes within the mid-gap states, reduced rapid-charge recombination rates, and enhanced electron transfer from gCN onto Pt nanoparticles.[49]

The three chemical characterization techniques employed here show that MgCN is the most conjugated of the three materials with the lowest concentration of O-containing defects, while UgCN is the most structurally disordered with the most O-containing defects. On this comparison alone, UgCN would be predicted to photocatalytically outperform both CgCN and MgCN due to the inclusion of more oxygen and edge defects. In contrast (Fig. 16), we find that CgCN, with intermediate characteristics of the three materials, is the highest performing photocatalyst.

Steady State Optical Correlation

Although generally considered a straightforward measurement, acquiring an accurate absorption spectrum is a surprisingly difficult endeavor for heterogeneous materials like gCN. Our results illustrate this challenge. For DRS, the absorption onset of the bulk material was found to increase in energy from MgCN to CgCN to UgCN. UV-Vis measurements performed on suspensions of the materials showed just the opposite trend. These results highlight why quantifying the “bandgap energy” of heterogeneous materials like gCN is exceptionally challenging.

Despite these challenges, lowering the absorption onset of gCN is often attributed to increased photocatalytic behavior.[49, 57] From the perspective of solar absorption, this strategy makes sense - lower absorption onsets may result in more electronic excited states poised to react. However, introducing optically active defects via doping or strain may not increase activity because the states are highly localized and never result in “free” charge carriers. Thus, while

ground state absorption measurements are an important characterization tool for confirming the optical properties of a material, absorption spectroscopy provides little predictive power in determining photocatalytic performance. In the case of the three materials studied here, the optical absorption onsets from DRS and UV-Vis measurements show no correlation to photocatalytic performance (Fig. 16).

Structural and chemical defects have been shown to strongly perturb the PL behavior and photocatalytic activity of gCN.[50, 51, 57, 85] However, general trends between PL behavior and the photocatalytic activity of gCN are not well established. For example, Nui et. al. saw that the gCN samples with the lowest QY had higher H_2 production rates.[60] Yang et. al. measured the highest % degradation of methylene blue in gCN samples with higher QY.[51] However, Xavier et. al. observed no correlation between photocatalytic activity and QY.[50] In this work, we also observe no correlation between QY and photocatalytic activity. Unfortunately, there is a discontinuity between photocatalytic performance and physical observables like QYs. Therefore, we continue to look for optical trends correlating to observed photocatalytic degradation.

Time-resolved Spectroscopy Correlation

Because time-resolved spectroscopies directly create and probe the excited states responsible for photocatalysis, both TRPL and transient absorption spectroscopy have the potential for providing strongly correlated data to photocatalytic activity.

TRPL spectroscopy is often used to elucidate differences in excited-state dynamics in gCN photocatalytic systems. While TRPL techniques provide a facile means to directly probe the dynamics of excited states, the complicated trapping processes in mid-gap states[65 19 60] lead to low PL QY. Because the emissive states are only a small fraction of the overall photogenerated

population, the use of TRPL as a predictive tool of photocatalytic activity is broadly inconsistent. Both longer[86] and shorter[57, 58] PL lifetimes have been correlated to improved photocatalytic activity. Others report no strong correlation between PL lifetimes and photocatalytic activity.[50, 87] The poor correlation between TRPL and photocatalytic activity in gCN heterojunctions has been recently reviewed by Godin et. al. While comparing 23 metal-free gCN PL studies, Godin et. al. found that 20 studies reported larger catalytic activity compared to a gCN reference. Of those 20 studies, 12 reported longer PL lifetimes in more catalytically active gCN materials, 5 reported shorter lifetimes, and 3 saw no significant change.[18]

We found no outstanding correlation between average PL lifetimes and photocatalytic activity at any probed excitations or emission wavelengths. While one set of PL lifetimes (400 nm exc. 480 nm em.– Fig. 14(d)) qualitatively matches the trend in photocatalytic activity, we believe this agreement is spurious. If the 480 nm emission band reports on a subset of catalytically active states, similar trends in PL lifetime wouldn't be observed for 315 nm (Fig. 14(b)) or 360 nm (Fig. 14(d)) excitation wavelengths. Indeed, it would be surprising if a PL trend seen at a singular excitation with a low QY strongly predicted all the photophysical and photochemical processes occurring under broadband illumination.

Generally, three main excited state processes occur in gCN after photoexcitation: exciton dissociation to free charge carriers (~200 fs)[23], rapid recombination (<240 ps)[22], and excited state trapping (ns-s).[19, 88] The observed PIA is likely a convolution of absorbing free electrons and holes.[16] All three materials have similar PIA decay lifetimes (See Table A3). However, the longer lifetimes component of CgCN is ~ 300 ps greater than in MgCN and UgCN. If the PIA decay is indicative of a changing population of free charge carriers, longer PIA lifetimes suggest that

charge carriers are trapped. While trapping events mitigate rapid charge recombination and facilitate photocatalytic activity, trapping can also significantly lower the reduction potential of gCN by ~1 eV, hindering photocatalytic activity.[19]

The PIB feature is likely a convolution of ground-state bleach, stimulated emission, and photoinduced reduction in scattering. Free charge carriers may reunite and form singlet or triplet states, leading to nonradiative decay back to the ground state.[23, 88] Additionally, excitonic or charge-separated states can decay both radiatively and nonradiatively.[19, 85 23, 88] Therefore, singlet and triplet exciton recombination, charge carrier recombination, and emissive trap states[19, 85] could all be contributing to the observed PIB signal. Regardless of the source of the PIB signal, the longer CgCN lifetime indicates slower excited-state decay. The combined effects of interplanar distance, intraplanar conjugation, and defect density on radiative and nonradiative processes may be creating a "Goldilocks" zone where rapid charge recombination is surpassed via excited state trapping, but photocatalytic activity is preserved as the excited states are only in "shallow" traps. Interestingly, a clear photophysical difference is seen in the PIB, while the PIA decay traces are almost indistinguishable. If the PIA is mainly comprised of absorbative free charge carrier states, the evolution of free charge carriers (ie. charge carrier trapping and recombination) only represents a portion of the photocatalytically important processes. More mechanistic studies are needed to help establish relationships between specific excited-state species and photochemical processes.

The transmissive TA lifetimes trend with observed photochemical behavior, suggesting the PIB feature represents photophysical processes that have a profound, measurable impact on Rhd B photodegradation rates, reinforcing the connectivity of photophysical properties, chemical

characteristics, and structural characteristics collectively affecting the observed photocatalytic activity.

Conclusion

Resolving the structure-function relationships in organic functional materials, like gCN, is paramount for optimizing photocatalytic and optoelectronic properties. In this study, we observed the complicated interplay of chemical, structural, and optical characteristics with photocatalytic activity by measuring physical observables. These observables included the degree of crystallinity, interplanar spacing, intraplanar conjugation, percent oxygen, optical absorption onsets, QYs, PL lifetimes, and TA lifetimes. We found no correlation between photocatalytic performance and the measured structural, chemical, optical steady-state, or TRPL observables. However, PIB TA lifetimes predicted the high catalytic performance of CgCN compared to UgCN and MgCN. While there are reported correlations between photocatalytic activity and certain material properties like chemical defects, polymeric structure, QYs, and PL lifetimes, this work suggests that these physical observables are not routinely reliable, stand-alone measurements for predicting certain photophysical processes like charge separation and recombination in gCN.

Weak correlations between photocatalytic activity and many chemical, structural, and optical properties likely result from many confounding factors. Observed photocatalytic behavior is affected by a myriad of catalytic, material, and optical properties. Disentangling the effects of one property from another is difficult and requires corroborating findings through complementary techniques. We suggest more studies that focus on amassing the excited state dynamics in well-characterized gCN. Photocatalytic gCN models may also benefit from

characterizing specific excited-state dynamics in controlled systems mimicking popular photocatalytic schemes. Elucidating excited-state dynamics in systems resembling “real-world” reaction environments may unmask critical photocatalytic variables and considerations.

CHAPTER FOUR

ULTRAFAST CHARGE INJECTION IN SILVER-MODIFIED GRAPHITIC CARBON NITRIDE

Contribution of Authors and Co-Authors

Manuscript in Chapter Four

Author: Emma K. Orcutt

Contributions: Performed steady-state and time-resolved optical measurements and analyzed the results. Wrote and edited the manuscript.

Co-Author: Shelton J.P. Varapragasam

Contributions: Synthesized the materials presented in this work.

Co-Author: Zöe C. Peterson

Contributions: Helped collect steady-state optical measurements.

Co-Author: Erik M. Grumstrup

Contributions: Assisted with analysis and editing of the manuscript for final submission.

Manuscript Information

Orcutt, Emma K.; Grumstrup, Erik M.

Status of Manuscript:
☐ Prepared for submission to a peer-reviewed journal
☐ Officially submitted to a peer-reviewed journal
☐ Accepted by a peer-reviewed journal
☒ Published in a peer-reviewed journal

ACS Applied Materials and Interfaces
Issue 12
10.1021/acsami.2c22870

Abstract

Graphitic carbon nitride (gCN) is a promising organic platform for driving light-activated charge transfer reactions in a number of valuable photocatalytic cycles. A primary limitation of gCN as a photocatalyst is its short excited state lifetime, which is mediated by a high density of trap and defect sites that result in rapid excited state decay and low photocatalytic efficiency. To enhance catalytic activity, gCN is often functionalized with a metal co-catalyst, however, the mechanism by which metal cocatalysts enhance reactivity has not been clearly established. In this work, excited state dynamics of gCN and silver modified gCN are compared using ultrafast transient absorption and time-resolved photoluminescence spectroscopies. In silver modified gCN, an ultrafast spectral shift in the silver plasmon resonance provides direct spectral evidence of electron transfer from gCN to the silver nanoparticles. The electron transfer rate is competitive with other non-radiative relaxation pathways, with electron transfer yields approaching 50%, thus providing an effective strategy for mitigating losses associated with defects and trap sites.

Introduction

Photoactive organic semiconductors are increasingly important frameworks for photocatalytically activated chemical reclamation, organic synthesis, and energy production due to their high degree of tunability and abundant precursors.[13, 30, 89] One particularly promising photocatalytic material is graphitic carbon nitride (gCN), with its tunable electronic structure, activity under visible light, and low toxicity.[56, 89-93] Despite these advantages, gCN's photocatalytic activity is limited by short excited state lifetimes and low charge mobility.[65, 94, 95] To address these limitations, significant efforts has been directed toward optimization of the

chemical and structural characteristics of gCN through, for example, leveraging different precursors[51, 74] or via tuning of synthetic and exfoliation approaches. [16, 95, 96] Another widely utilized strategy functionalizes gCN with metal nanoparticle co-catalysts, including Zn, Pt, Fe, Co, and Ag.[20, 93, 94, 97-101] The observed activity enhancement observed in these hybrid materials is typically attributed to charge separation across the gCN/metal interface, which is believed to mitigate charge recombination and yield long-lived redox active exited states.[102-105]

Despite the widespread assumption that electron transfer (eT) from gCN to a metal co-catalyst is competitive with other catalytically-inactive excited state relaxation pathways, there is little direct and unambiguous experimental evidence that supports this picture. Numerous studies have employed time-resolved photoluminescence (TRPL) to elucidate interfacial charge transfer in gCN. However, as comprehensively reviewed by Godin et al., TRPL kinetics provide an incomplete probe of eT processes.[18] Indeed, relative to pristine gCN, gCN functionalized with a cocatalyst is just as likely to exhibit a shorter PL lifetime as a longer one.[18] This conflicting behavior in PL lifetime likely stems from rapid relaxation to non-radiative states, intrinsic material heterogeneity, and the introduction of new interfacial states upon functionalization.

An alternative technique for studying eT in gCN/metal systems is transient absorption (TA) spectroscopy. Because of the technique's sensitivity to non-emissive states and its exceptional time resolution, TA is a clear choice for elucidating possible ultrafast eT mechanisms. Surprisingly, only a few authors have reported TA studies of metal/gCN systems.[19, 22, 106] Godin and coworkers compared pristine gCN with Pt/gCN using TA and concluded from broadband spectral comparisons that eT likely occurs on the ns timescale.[19] Khan et. al. concluded from a kinetic analysis of a broad photoinduced absorption (PIA) that eT occurs on

the 10 ps timescale, although metal-semiconductor interfacial trapping was not ruled out.[22] Recently, Tong and coworkers, also comparing Pt/gCN to gCN via TA spectroscopy, monitored the kinetics of the same PIA as Ref. 28 and attributed a short lifetime component in Pt/gCN ($\tau \sim$ 1 ps) to eT.[106]

While these works are consistent with an eT mechanism, they do not provide direct evidence that the metal acts as an electron sync. Instead, the kinetics of broad gCN-derived transient spectral features are monitored, and any observed decrease in the lifetime in Pt/gCN (relative to unmodified gCN) is ascribed to the eT process. A challenge with such kinetic analyses is the co-evolving electron trapping, transport, and relaxation dynamics which are convolved together with the eT dynamics occurring on the same timescales. These kinetic challenges, together with the fact that there are no clear spectral signatures of the charge separated state in Pt/gCN, perhaps explains why reported timescales for eT in Pt/gCN span three orders of magnitude (1 ps – 1 ns).[19, 22, 106]

To overcome these limitations, this work utilizes time-resolved emission and absorption spectroscopies to elucidate eT in silver functionalized gCN (Ag/gCN). The use of silver nanoparticles, instead of the commonly used Pt or Pd cocatalysts, provides an unambiguous spectral handle with which to monitor the eT dynamics: by time resolving spectral shifts in the Ag nanoparticle surface plasmon resonance after gCN photoexcitation, we directly monitor eT from photogenerated gCN states.[107] Comparisons of broadband TA spectra from gCN and Ag/gCN show that eT occurs on sub picosecond timescales, providing direct evidence that metal nanoparticle cocatalysts provide a pathway to a charge-separated state that is competitive with other catalytically inactive relaxation pathways.

Steady State Spectroscopy

A comparison of the ground state absorption spectra from gCN and Ag/gCN suspensions are shown in Fig. 17A. The water suspensions are prepared by mechanical exfoliation of bulk gCN powders polymerized from a urea precursor as detailed in supporting information. The exfoliation procedure employed for the two samples and their absorption spectra are consistent with few-layer gCN particles, sometimes referred to as gCN "nanosheets" in previous reports.[108, 109] Both spectra have similar profiles at wavelengths shorter than 320 nm, with Ag/gCN exhibiting a significant absorption from 350 – 400 nm, attributed to the surface plasmon resonance (SPR) of the photo-deposited silver nanoparticles.[110-112] Figure 17B shows a comparison of the difference spectrum, obtained by subtracting the two absorption spectra in panel A. Also plotted in Fig. 17B is a modeled surface plasmon resonance (SPR) spectrum for silver nanoparticles. The modeled SPR spectrum is calculated by combining the experimentally measured dielectric function[113] of silver to account for interband transitions and the off-resonance Drude response to account for the particle size dependent SPR linewidth (see Appendix B).[111, 112, 114] The good agreement between the two spectra, particularly at wavelengths red of the silver interband transitions, confirms that the prominent shoulder from 350-400 nm, as well as the low amplitude tail that extends beyond 650 nm results from the SPR of the deposited silver nanoparticles. Note however, that the good agreement between the two spectra is obtained only when a 1 nm diameter particle size is assumed in the model. When the Ag particle diameter is parameterized as 30 nm, which reflects the average diameter obtained from transmission electron microscopy images (Fig. B1), the modeled SPR is far narrower than what is obtained experimentally, likely indicating that the Ag nanoparticles are polycrystalline, or that the

suspended Ag/gCN particles used for optical studies tend to have smaller Ag particle size than those imaged with TEM.

Figure 17C shows steady state photoluminescence (PL) spectra collected from absorption-matched (at 315 nm) suspensions of gCN (black) and Ag/gCN (blue). Integration of the PL spectra for both samples shows that the quantum yield for Ag/gCN is quenched by 56% relative to gCN (Table B1). While lower intensity, the Ag/gCN PL spectrum is nearly identical in shape to that of gCN, suggesting that although functionalization of gCN with silver nanoparticles does lead to a lower overall PL quantum, it does not appear to significantly perturb the unquenched radiative states of the gCN system. Corresponding excitation spectra, collected by monitoring PL at 475 nm are shown in Fig. 17D. Comparison of the gCN excitation spectrum (black) with its ground state absorption spectrum (light grey) shows qualitative agreement, which suggests that for excitation at wavelengths, $\lambda_{ex} > 300$ nm, the photogenerated states follow similar relaxation pathways and produce the same fraction of emissive states. On the other hand, for $\lambda_{ex} < 300$ nm, the excitation spectrum and the absorption spectrum differ, consistent with a higher relative PL quantum yield for higher energy excited states.

Comparison of the excitation spectra of Ag/gCN (blue) to that of gCN shows they are qualitatively different in their shape. For $\lambda_{ex} < 375$ nm, PL is quenched upon Ag functionalization – at 340 nm, the PL from Ag/gCN is quenched by 20% and at 300 nm, by nearly 50% (Appendix B). This decrease in PL intensity at higher energies is consistent with an eT process from the photoexcited gCN to the Ag nanoparticles. In contrast, at excitation wavelengths, $\lambda_{ex} > 375$ nm, the emission intensity for the Ag/gCN is higher than for gCN (Appendix B). While signal to noise is low in this spectral region due to weak absorption, the

inversion in the quantum yield for Ag/gCN suggests that plasmonic energy transfer leading to excited gCN states may be a minor excitation pathway in these hybrid systems.

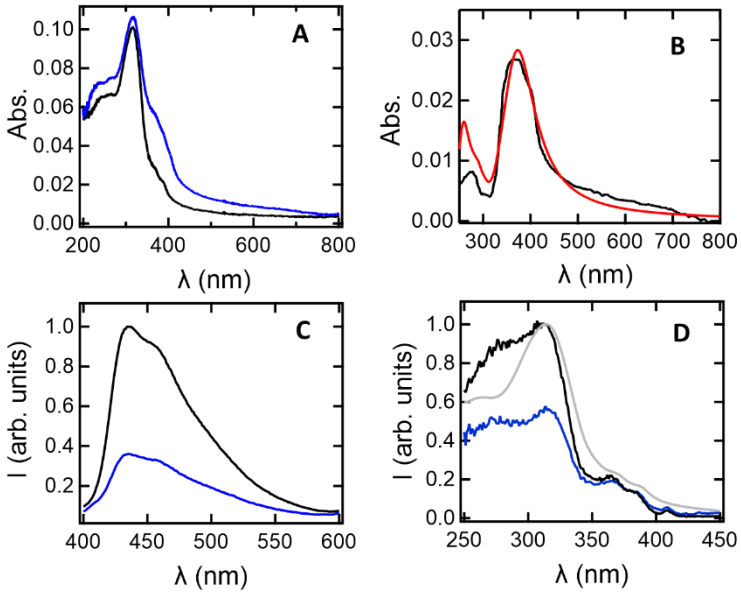

Figure 17: A) Ground state absorption spectra of gCN (black) and Ag/gCN (blue). B) Difference spectrum (black) obtained by subtracting absorption spectra in panel A. The red trace shows a modeled SPR spectrum. C) Emission spectra of gCN (black) and Ag/gCN (blue) collected after 315 nm excitation D) Excitation spectra monitoring the emission wavelength, λ_{em} = 475 nm, for gCN (black) and Ag/gCN (blue). Also shown is the ground state absorption spectrum of gCN (gray), reproduced from panel A.

Time-Resolved Spectroscopy

To evaluate whether electron transfer is responsible for the observed steady state PL quenching of Ag/gCN, we next turned to time-correlated single photon counting (TCSPC). Time-resolved PL kinetics were collected from suspensions of gCN and Ag/gCN at two emission wavelengths (λ_{em}: 440 nm, 530 nm) using two excitation wavelengths (λ_{ex}: 315 nm, 360 nm). Previous work has suggested that gCN PL arises primarily from excitonic states, and the PL kinetics reflect an equilibrium with a manifold of midgap trap states which undergo non-radiative

recombination.[19] The time-resolved PL traces along with fits to a modified stretched exponential model are shown in Fig. 18. Fit-determined parameters and associated errors are presented in Table B2. Note that previous authors have demonstrated power-law decay in the TRPL traces, particularly at timescales longer than 10 ns.[19, 23] However, log-log plots of the TRPL traces shown in Fig. 18 are nonlinear, indicating that for this set of materials, a power law model is not appropriate. Although in all cases, the kinetics are well fit with a triple exponential model, we instead fit the TRPL kinetics in Fig. 18 to a stretched exponential function (convolved with the instrument IRF) as it has fewer parameters (three instead of six) and is based on a physically plausible model in which a continuous distribution of decay rates contributes to the observed kinetics.[44, 115]

For gCN, the PL decay kinetics at the peak (λ_{em} = 440 nm, Fig. 18A) and red edge (λ_{em} = 530 nm, Fig. 18B) of the emission band are nearly independent of excitation wavelength. This behavior suggests that regardless of the excitation wavelength, the manifold of states through which the initially generated excited states relax is the same, at least on timescales longer than the instrument response (~100 ps). This result is consistent with the close match between the excitation spectrum and ground state absorption spectrum shown in Fig. 17D, which shows that the PL quantum yield at 440 nm is independent of excitation wavelength. In Ag/gCN, similar excitation energy-independent kinetics are observed at λ_{em} = 530 nm (Fig. 18D). In contrast, at λ_{em} = 440 nm, the kinetic decay observed after 315 nm excitation is qualitatively slower than that at 360 nm excitation, suggesting that the energy of the initially populated states strongly impacts the branching ratio of excited state relaxation.

A quantitative comparison of the TRPL traces for gCN (Figs. 18A,B) and Ag/gCN (Figs. 18C,D) reveals other important differences. In all cases, the fit-determined ensemble average time constant, $\langle\tau\rangle$, decreases upon silver functionalization (see SI for calculation of $\langle\tau\rangle$). For example, at λ_{em} = 530 nm after 315 nm excitation, $\langle\tau\rangle$ = 0.95 ± 0.03 ns for Ag/gCN (Fig. 18D) and $\langle\tau\rangle$ = 2.02 ± 0.14 ns (Fig. 18B) for gCN. This difference in $\langle\tau\rangle$ primarily arises from early time dynamics (< 2 ns), suggesting that additional non-radiative pathways compete with those available in the unmodified gCN system. While it is possible that the competitive pathway is electron transfer, it is challenging to ascribe the faster kinetics, by themselves, to eT. Relaxation via other non-radiative pathways like those that might occur through, for example, Ag/gCN interfacial defect states, would similarly lead to faster decaying TRPL kinetics.

The excitation energy dependence of the Ag/gCN PL kinetics at λ_{em} = 440 nm (Fig. 18C) poses a further challenge to interpretation. Based on the steady-state excitation spectra shown in Fig. 17D (and Fig. B2(B)), it is known that PL in Ag/gCN is more strongly quenched for 315 nm photoexcitation than for 360 nm photoexcitation, suggesting that higher energy excitation yields a greater fraction of eT states. Given the discussion of the preceding paragraph, a higher eT yield and qualitatively *slower* TRPL kinetics for λ_{ex} = 315 nm (relative to λ_{ex} = 360 nm) appear to be contradictory. We suspect this apparent contradiction derives from two causes. First, as we describe in detail below, electron transfer to the Ag nanoparticles occurs on ultrafast (< 1 ps) timescales, far below the time resolution of the TCSPC instrument employed for these measurements and certainly much faster than the natural radiative lifetime of gCN. Therefore, at short times, kinetic evidence of (ultrafast) electron transfer will be convolved with the IRF of the TCSPC instrument, yielding a kinetic decay that is only sensitive to slower (~ ns) timescale

dynamics. Indeed, fits to the kinetics in panel C to the stretched exponential model recovers time constants significantly below the instrument response (τ_{315} = 7.6 ps and τ_{375} = 7.5 ps), strongly suggesting ultrafast excited state dynamics are occurring which are not resolved by TRPL measurements.

Although the instrument time resolution explains why the two kinetics traces in panel C appear similar at early times, it does not explain why the λ_{ex} = 315 nm decay is slower for times > ~ 1 ns. One possible explanation for the difference in behavior is back electron transfer (beT) from the Ag nanoparticles to re-form emissive states in gCN. Although beT would be expected for both excitation wavelengths, the larger population of charge transfer states produced for λ_{ex} = 315 (Fig. 17D) would yield a greater contribution to PL from beT at long times. A beT process would also help explain the relatively poor fit of the stretched exponential model to the λ_{ex} = 315 TRPL trace at long times (Fig. 18C, black solid line), when the observed population would have both sink (nonradiative relaxation) and source (beT) terms. On the other hand, if the slower kinetics for 315 nm excitation are a result of beT, it raises the question of why the kinetics on the red edge of the emission band (λ_{em} = 530 nm, Fig. 18D) are (nearly) independent of excitation energy. One possibility is that the beT rate is smaller for the lower energy gCN sites that emit at 530 nm, perhaps due to energetic mismatch or fast hole transport away from those sites.

The above discussion highlights the difficulty of interpreting the TRPL kinetics in gCN and the hybrid Ag/gCN system. In the case of the materials studied in this manuscript, an unambiguous assignment of one particular kinetic parameter (i.e. lifetime) to eT is impossible without other spectroscopic probes. This task is made even more difficult by the highly

heterogenous nature of these systems and by excited state transport, both of which result in non-exponential decay kinetics.[44]

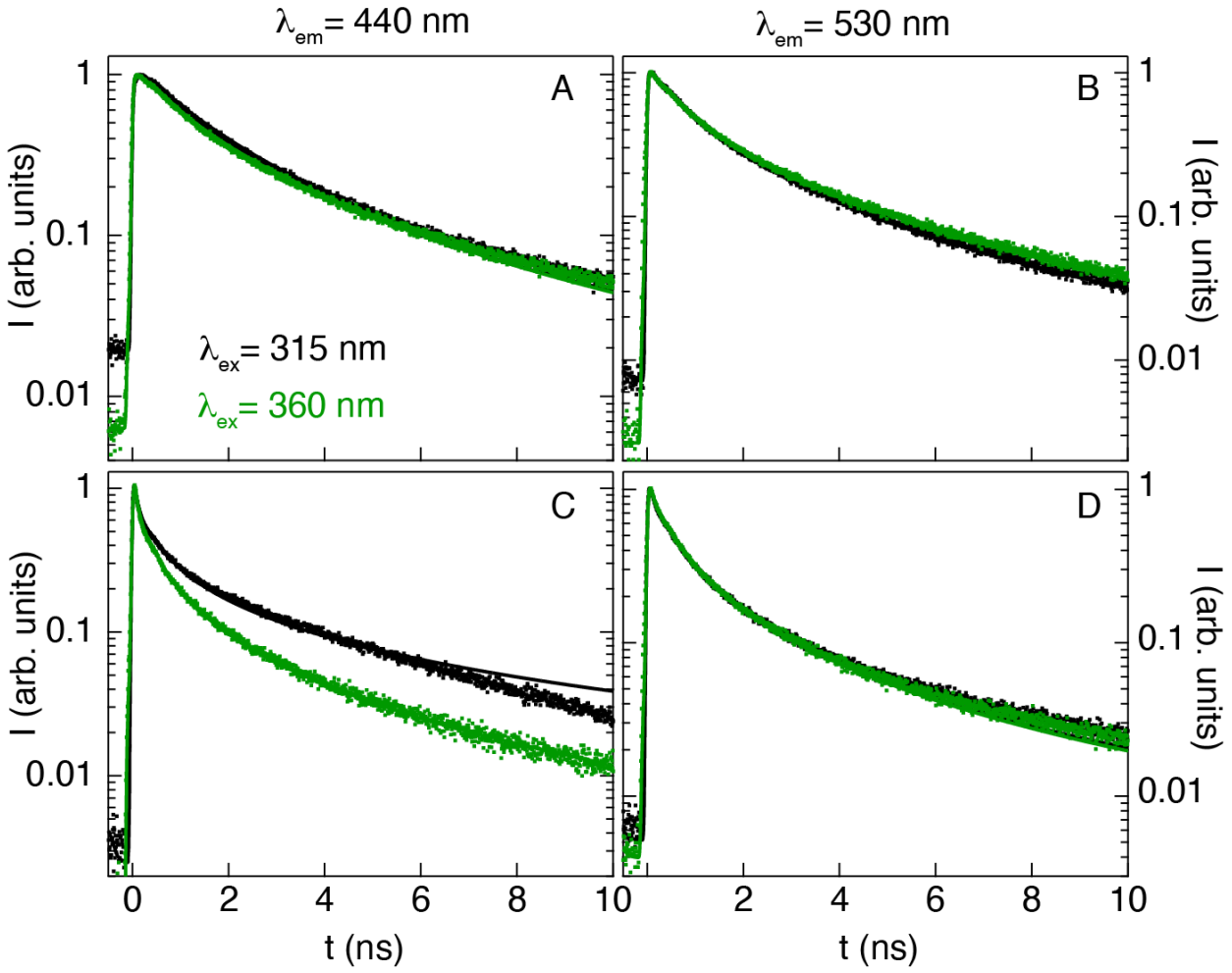

Figure 18: TRPL traces collected at emission wavelengths 440 nm and 530 nm for gCN (A, B) and Ag/gCN (C, D). In each panel, the different color traces correspond to 315 nm (black) and 360 nm (green) excitation wavelengths.

Therefore, to further elucidate the difference in excited state dynamics between gCN and Ag/gCN, we next turned to broadband transient absorption spectroscopy. Both samples were photoexcited using a 343 nm pump pulse produced through third harmonic generation of the 1035 nm fundamental. The photoexcited samples were probed with a broadband continuum

spanning 490 – 800 nm generated in a yttrium aluminum garnet (YAG) crystal. For both samples, decay kinetics were confirmed to be power independent at the excitation fluence of 32 $\mu J/cm^2$. Figure 19 A compares chirp-corrected transient spectra obtained at $\Delta t = 0$ ps. For both systems, the spectra are dominated by a broad photoinduced absorption (PIA) that extends beyond the 750 nm edge of our detection range. Previous authors have assigned this PIA primarily to electrons which form upon ultrafast (~ 200 fs) charge separation after photoexcitation.[16, 19, 23]

Although at the earliest temporal delays, gCN and Ag/gCN have nearly identical transient spectra, the spectra evolve to be dramatically different by $\Delta t = 0$ ps. As shown in panel B of Fig.19, the PIA that characterizes the charge separated state continues to grow for gCN, particularly at wavelengths red of 600 nm. In contrast, for Ag/gCN, the PIA rapidly decays, and we observe an evolution of the PIA into a bleach at wavelengths shorter than 575 nm. Panel C compares spectrally integrated kinetics from 510 nm – 560 nm for both systems. While the kinetics from gCN rise within the instrument response and remain nearly unchanged, the initial PIA rapidly evolves into a bleach for Ag/gCN. Fits to the kinetics show that the growth of the bleach occurs in $1/k = 390 \pm 80$ fs.

Given the results described above from steady state and TRPL spectroscopies, we hypothesized that the ultrafast spectral evolution that occurs in Ag/gCN was due to electron transfer (eT) from gCN to the Ag nanoparticles. This eT would be expected to produce two effects on the observed spectra. First, the broad photoinduced absorption stemming from charge separated electrons should decay as they are transferred from gCN to the Ag nanoparticles. Second, as electron density is increased in the Ag nanoparticles, their surface plasmon resonance

(SPR) should blueshift, since the plasma frequency scales $\omega_p \sim \sqrt{n}$, where n is the free electron density. [107, 116] Both effects would lead to a net decrease in photoinduced absorption in the spectral region probed, as observed in Fig.19.

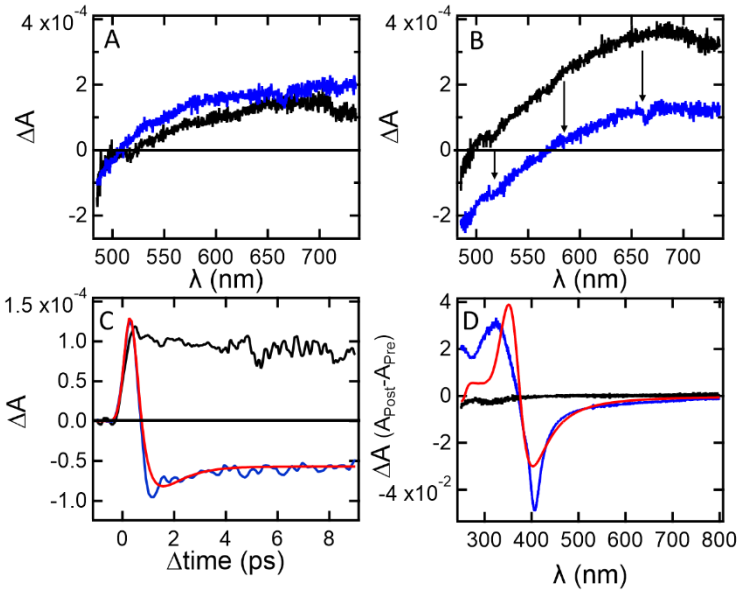

Figure 19: Comparison of transient absorption spectra from gCN (black) and Ag/gCN (blue) at A) Δt = 0 ps and B) t = 2 ps after the arrival of the pump. Arrows added to highlight the decay of the PIA and growth of the bleach between 500 and 550 nm. C) Kinetics averaged from 510-560 nm for gCN (black) and Ag/gCN (blue). A fit to the Ag/gCN kinetics with a biexponential model convolved with the instrument response is shown in red. The fit-determined bleach growth occurs in 1/k = 390 ± 80 fs. D) Difference between absorption spectra for both Ag/gCN (blue) and gCN (black) obtained post- and pre- chemical reduction. Plotted in red is a calculated difference spectrum of the SPR after a 0.3% increase in electron density (red).

To confirm that eT from gCN to the Ag nanoparticles was responsible for the observed spectral evolution, we chemically reduced gCN and Ag/gCN using $NaBH_4$. The differential spectra, calculated by subtracting the pre-reduced spectrum from that collected after addition of the $NaBH_4$, are shown in Fig.19D. For gCN, the addition of 0.1 equivalents of $NaBH_4$ produced little difference in the absorption spectrum (black trace). On the other hand, addition of $NaBH_4$ to Ag/gCN results in the derivative-like feature in the differential spectrum (blue). The proximity of

this derivative-like feature to the Ag SPR (Fig. 17B) suggests that it arises from a blueshift of the Ag SPR upon chemical reduction. A comparison of the differential spectrum from pre- and post-$NaBH_4$ addition with the calculated differential spectrum obtained by shifting and subtracting the modeled SPR mode shown in Fig. 17B qualitatively reproduces the lineshape, particularly at wavelengths longer than 380 nm where interband transitions (of Ag or gCN) are not expected to significantly contribute.

Due to the blue-edge cutoff of the probe continuum, we are unable to probe in the spectral region where changes associated with the plasmon shift would be most apparent (< 450 nm). However, the transient spectra do probe the broad tails of the SPR (extending to ~ 750 nm, Fig. 19D), which would be expected to bleach upon photoreduction. It is this ultrafast blue-shifting of the SPR to which we attribute the rapid spectral evolution seen in Figs. 19B,C for the Ag/gCN system. Given that exciton mobility is known to be low in gCN (10^{-6} to 10^{-4} cm^2 V^{-1} s^{-1}) [22, 23], the ultrafast (1/k ~ 390 fs) plasmon shift observed suggests that eT occurs only for those excited states that are in close proximity to the Ag nanoparticles. While eT from states initially photogenerated far from an Ag nanoparticle is possible, those states would require transport to a proximal site. It may be that the decrease in PL lifetime (on timescales less than ~ 2 ns) observed for Ag/gCN (Fig. 19) derive from such a “transport-limited” eT process.

On longer timescales, the broad PIA characteristic of excited electrons in gCN decays over the 3.2 ns time window accessible on our instrument. Figure 20A compares kinetics from gCN (black) and Ag/gCN (blue) integrated from 710-750 nm. Also shown in Fig. 20A are fits to the data with a biexponential model. For delay times up to 500 ps, the kinetics traces are similar, with Ag/gCN decaying with a time constant, τ_1 = 166 +/- 3 ps and gCN decaying with τ_1 = 142

+/- 3 ps. At longer times, the two traces diverge, with Ag/gCN decaying more slowly (τ_2 = 4.47 +/- 0.07 ns) than gCN (τ_2 = 2.23 +/- 0.02 ns). We attribute the slower decay in Ag/gCN to back electron transfer from the charge separated state to reform an emissive gCN state.

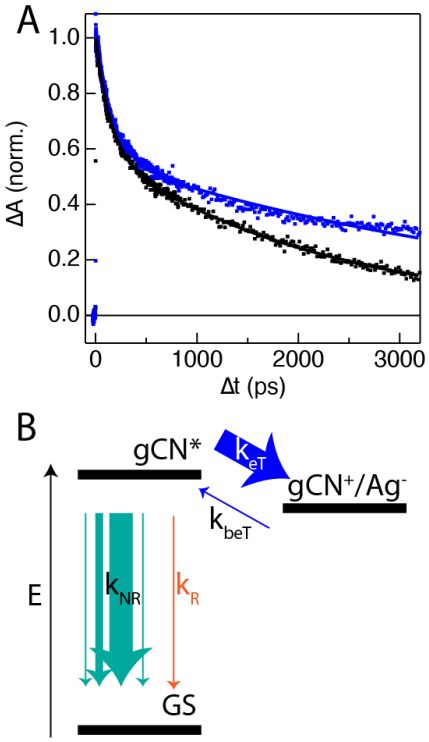

Figure 20: A) TA kinetic traces (dots) and biexponential fits (line) averaged from 710-750 nm for gCN (black) and Ag/gCN (blue). B) Simplified scheme outlining relaxation pathways for photoexcited gCN in contact with an Ag nanoparticle. Larger arrow widths illustrate fast processes, narrow arrow widths, slow processes.

Figure 20B shows a simplified scheme that summarizes the spectroscopic findings of this work. Photoexcitation of gCN produces excited states that undergo both radiative and nonradiative decay. Consistent with previous authors, our TRPL results indicate that the nonradiative decay is best described by a distribution of relaxation rates,[19, 44] likely reflecting the chemically and structurally heterogeneous nature of gCN suspensions. In the presence of an Ag cocatalyst, ultrafast (< 1 ps) electron transfer to the silver nanoparticles competes with rapid

excited state relaxation/trapping intrinsic to gCN. Our results suggest that the eT process is sufficiently rapid that ~ 50% of initially photogenerated states undergo electron transfer (for λ_{ex} ~ 300 nm). Whether this eT yield is limited by intrinsic material properties (i.e. immobilized/trapped excited states), or whether it reflects a subpopulation of gCN nanosheets that remain unfunctionalized remains uncertain. There is some evidence from TRPL that eT continues to occur on the nanosecond timescale, perhaps limited by charge transport in gCN, but it is difficult to disentangle these slower eT dynamics from other excited state relaxation processes occurring on similar timescales, one of which may be back electron transfer.

Conclusion:

Dispersed suspensions of pristine gCN and Ag/gCN were compared using a suite of steady state and time-resolved spectroscopic techniques. Time-resolved photoluminescence kinetics provide some indirect evidence for eT from gCN to Ag nanoparticles, however interpretation is complicated by limited time resolution and unrelated dynamics (beT, non-radiative relaxation) occurring on similar timescales. Transient absorption spectroscopy, with its improved time resolution and sensitivity to non-emissive states, provided an unambiguous probe of the eT process. By monitoring the SPR spectral blueshift associated with increased electron density on the Ag nanoparticles, eT from gCN was found to occur on sub picosecond timescales. The rapid eT process is competitive with other (presumably non-photocatalytic) relaxation processes, resulting in a large fraction of charge separated states primed for interfacial redox chemistry. In sum, these results provide a direct, quantitative description of how metal functionalization enhances catalytic activity of gCN. They also suggest that very high quantum

yields of photochemically active states can be produced in metal/gCN systems with appropriate material design.

CHAPTER FIVE

PORPHYRIN-DERIVED SUPRAMOLECULAR ASSEMBLIES: EXCITED STATE DYNAMICS IN SOLUTION PHASE AND THE SOLID STATE

Introduction

Porphyrin systems have historically captured scientific attention due to their prevalence in nature and versatile applications for medical, photocatalytic, optical, and optoelectronic fields.[117-120,27] The optical tunability and efficient energy transfer of porphyrins enable many industrial applications.[118] Like other organic functional materials, fabricating well-ordered porphyrin aggregates is difficult due to weak noncovalent interactions between monomers. Heterogeneous aggregation pathways can result in structurally disordered materials with complicated electronic coupling, unfavorable excited-state dynamics, and sub-optimal device properties.

In this chapter, we study the optical properties of a novel zinc porphyrin (ZnP) monomer (See Fig. 21(a)). This large monomer was designed to have hydrophobic, hydrophilic, and aromatic groups with reactive hydroxyl species to facilitate anti-solvation techniques, monomeric tethering, and enhanced optical properties. Large oligomeric substituents, poly(p-phenyleneethynylenes) (PPE), are bonded directly to the *meso* positions of the ZnP macrocycle. The optical effect of adding these side chains to the ZnP is unclear. A 2016 study monitored the steady-state absorption of porphyrins with 0-4 *meso* phenyl group substituents and observed that all Q-band absorptions were red-shifted, and strictly excitonic Q-band peaks decreased in

intensity.[26] If relatively small phenyl substituents noticeably change the optical properties of a porphyrin macrocycle, one could hypothesize that large oligomeric PPE side chains, like the ones shown in Fig. 21(a), could drastically affect the optical properties of the macrocycle.

The chemical and structural characteristics of PPE oligomers lead to unique properties, including quadratic coupling,[121] dynamic excited state lifetimes,[122] symmetry swapping,[123] and vibrational strong coupling.[124] These properties lead to a wide range of physical observables. Quadratic coupling between the ground and excited states can result in photoinduced structural rearrangements, which is evident in weak Stokes shifts.[121] PPE oligomers have dynamic excited-state lifetimes that nearly double as PPE conjugation lengths decrease[122] and quantum yields that vary vastly (0.94-0.19) as a function of structure and symmetry.[123] Due to the varying optical properties of a stand-alone PPE oligomer, elucidating the optical properties of our PPE functionalized ZnP monomer is a formidable task.

Self-assembly is a naturally occurring process in porphyrins and is driven by π-stacking and other noncovalent interactions such as hydrogen bonding and electrostatic interactions. Previous porphyrin aggregation studies have shown that aggregation in porphyrins results in J-coupling,[125-127] H-coupling,[120] and rapid energy transfer [15, 128, 129] as local aggregation, dipole-dipole interactions, and strong excitonic coupling affect the optical properties of the material. These three photophysical phenomena can lead to drastically different physical observables.[120, 130] For example, H-coupling leads to forbidden optical transitions, and consequently, excited state lifetimes are longer in the H-coupled aggregates compared to J-coupled aggregates.[15]

Porphyrins show promise as solid-state sensors; however, there is a lack of research comparing how optical properties, like fluorescence and excited-state dynamics, change between

solution and solid states.[131-133] While there are studies evaluating the optical properties of polymer thin films, these studies do not compare the optical properties between the solution and solid state.[25, 134, 135] In solution, the dipole-dipole interactions between the solute and solvent can play a significant role in the excited-state decay of a monomer.[136] In the solid state, excited state dynamics are driven by monomer-monomer interactions, where nanoscale defects can have macroscopic consequences on structural characteristics and excited state transport.[137] Therefore, the photophysical properties and electronic structure of porphyrin thin films are difficult to predict from liquid measurements.

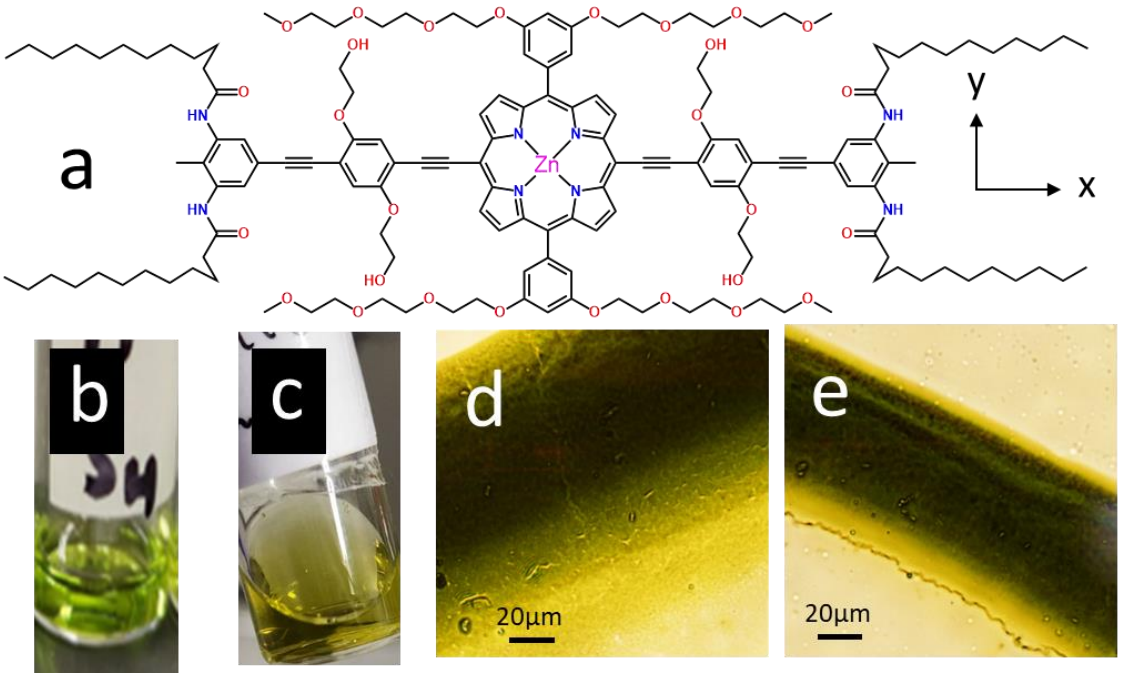

Figure 21: The (a) chemical structure of the novel ZnP derivative studied in this work. Pictures of the solution phase monomer (b) and (c) aggregate samples. Bright-field microscope images of the thin film (d) aggregate (AF) and (e) monomer (MF) samples.

This chapter describes optical measurements made on four ZnP samples (Fig. 21(b-e)), aimed at elucidating the interplay of chemical and intermolecular structure on excited state functionality from isolated monomers to condensed phase materials. First, we study the ZnP

monomer in solution (Fig. 22(left)) to investigate the effects of the PPE side chain coupling to the primary electronic structure of the porphyritic core. We then induce self-aggregation to form well-ordered molecular aggregates to investigate how intermolecular coupling affects excited state decay (Fig. 22(middle)). Finally, we form solid-state thin films (Fig. 22(right)) from both the solvated monomer and from the pre-assembled aggregate to understand the role of pre-aggregation on material structure and functionality. To do so, we employ both time-resolved and steady-state spectroscopic techniques to measure ground-state absorption, steady-state emission, photoluminescent (PL) lifetimes, and transient absorption (TA) spectra. The results presented here illustrate our current understanding of this complicated ZnP system and inform future works.

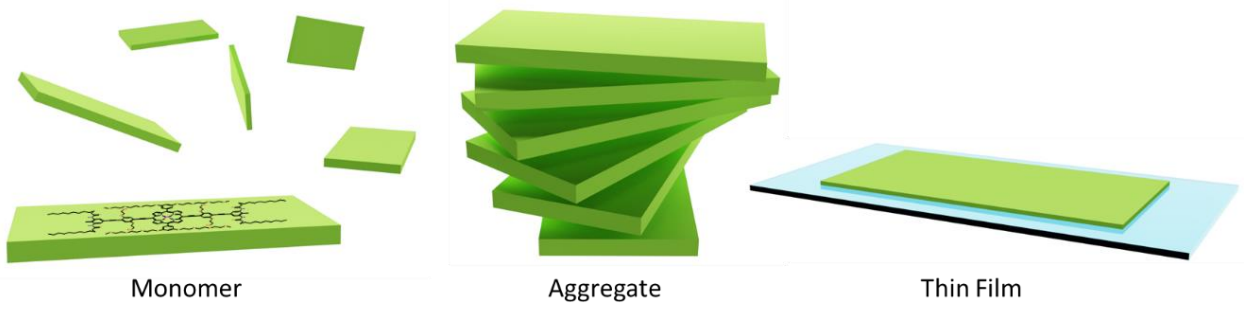

Figure 22: A representation of the changing systems between (left) solution-phase ZnP monomer, the (middle) solution-phase ZnP aggregate, and the (right) thin films of the monomer and aggregate. See the Sample Preparation section for more details.

Sample preparation:

Liquid-phase monomer samples were prepared by dissolving ~1 mg of the monomer (Fig. 21(a)) in 2 mL of tetrahydrofuran to achieve a nominal molarity of 191 μM. To prepare the liquid phase aggregate samples, 1 mg of the monomer was dissolved in a 3:7 ratio of

tetrahydrofuran:methylcyclohexane and allowed to sit for 4-7 days before optical measurements were performed. The solutions prepared here are referred to as the "monomer" (Fig. 21(b)) and "aggregate" (Fig. 21(c)), respectively.

The solid-state samples were created by drop casting a solvated monomer and self-assembled aggregate solution. To prepare the thin films, approximately 40 uL of the solution was drop-cast onto a glass slide and allowed to evaporate under ambient conditions for 30 minutes. These steps resulted in thin films with a coffee ring-like deposition pattern. To mitigate damage to the thin films during optical measurements, the samples were spin coated (3000 rpm) with 20 uL of a 10% wt/wt of styrene-ethylene-butylene-styrene polymer in toluene. The slide was then placed on a 40°C hotplate for 1 hour to evaporate any solvent. The thin film from the aggregate solution (Fig. 21(d)) and the thin film from the monomer solution (Fig. 21(e)) are referred to as the "TM" and "TA", respectively.

Results

Monomer Steady-State Characterization

The ground-state absorption spectrum of the monomer is shown in Fig. 23(a). The near UV absorption at $\lambda<400$ nm matches previously reported PPE ground state absorption spectra.[121, 122] A strong absorption feature at 467 nm results from Soret band transitions. Finer absorption features around 570, 618, 637, and 675 nm are attributed to Q-band transitions. The blue arrows shown in Fig. 23(a) point to the transitions mentioned above. Due to the asymmetric spectral profile of the Soret band absorption, PL measurements were taken at several excitation energies. The samples were excited with 450 nm and 470 nm light, respectively, and PL spectra were collected. The normalized emission spectra are plotted in Fig. 23(b). In the 450 nm emission

spectra, there are clearly visible peaks at 641 nm and 680 nm, with a smaller signal at 748 nm. Near 700 nm there appears to be signal intensity that does not scale similarly to the 680 nm peak at varying excitation wavelength, suggesting another emissive state is contributing to the overall signal. Interestingly, the relative intensities of the five emission peaks change drastically with varying excitation wavelengths, especially when the two excitation wavelengths are relatively similar in energy (87 meV). The five blue arrows in Fig. 23(b) indicate the four previously mentioned emission peaks and a fifth emission peak that becomes more apparent in PL spectra with 470 nm to 520 nm excitation energies. The broad signal at $\lambda<600$ qualitatively matches previously reported optical studies of PPE oligomers.[121, 122]

To further elucidate the cause of nonuniform changes in emission peak intensities, PL measurements were taken to monitor changes to PL intensity of 640, 680, and 748 nm energy radiative transitions at various excitation energies. The resulting excitation spectra are plotted in Fig. 23(c) and compared to the normalized ground state absorption spectrum. The excitation spectra of the PL experiment measuring 680 nm (green trace) and 745 nm (dotted green trace) radiative decay matches the ground-state absorption spectrum (black trace) well with the max peak intensity at 469 nm. However, the 640 nm excitation spectrum (blue) peaks noticeably bluer at 453 nm. The energetic difference between the peak of the green and blue excitation spectra is ~753 cm^{-1}.

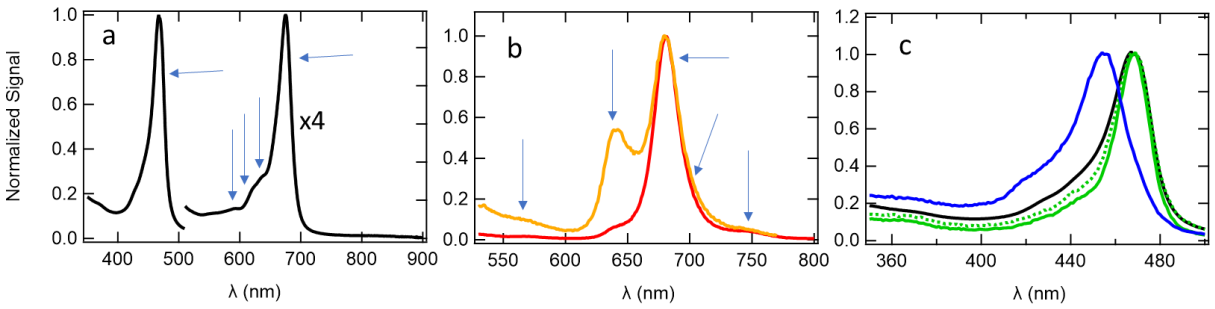

Figure 23: The (a) normalized ground state absorption spectrum of the monomer (black) with the Q-band intensity scaled up by a factor of 4. The (b) emission spectra of the monomer after 450 nm (orange) and 470 nm (red) energy excitation. The (c) excitation spectra of the monomer collecting 640 (blue), 680 (green), and 745 nm (dotted green) emitted light, respectively. The monomer ground state absorption spectrum is shown in black for comparison. Blue arrows point to transitions directly mentioned in the body of the text.

Monomer Time-Resolved Characterization

PL lifetimes were measured using Time-Correlated Single Photon Counting (TCSPC) spectroscopy at various excitation and emission wavelengths. The excitation wavelengths used were 375, 457, and 465 nm. These excitation energies were used to selectively excite the PPE side chains, the higher energy Soret band transitions, and lower energy Soret band transitions, respectively. Figure 24(a-c) compares 640 nm (a), 680 nm (b), and 745 nm (c) PL decay kinetics after exciting the monomer at 375, 457, and 465 nm (black, blue, and red traces, respectively). These same decay traces shown from panels a-c were rearranged to form panels d-f. While the comparison in Fig. 24(a-c) helps visualize how excitation energies affect PL decay from a particular state, Fig. 24(d-e) compares emissive decays at specific excitation energies.

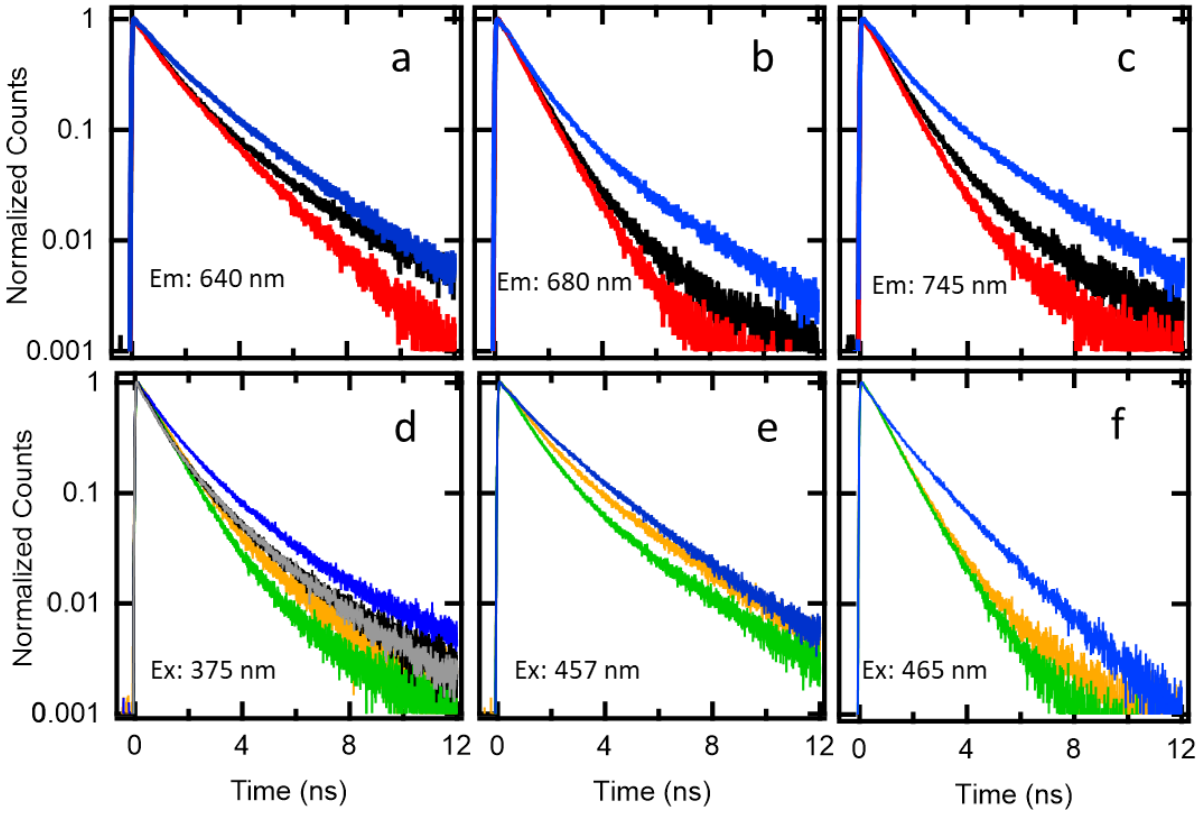

Figure 24: The PL decays of the monomer monitoring (a) 640, (b) 680, and (c) 745 nm radiative decay after exciting the sample with 375 (black), 457 (blue), and 465 nm (red) light. The monomer PL decays exciting at (d) 375, (e) 457, and (f) 465 nm measuring 440 (black), 490 (grey), 640 (blue), 680 (green), and 745 nm (orange) radiative decay.

The PL traces shown in Fig. 24 were fit using a double or a biexponential fitting model (see Appendix A) and the resulting fits are given in Table 4. The PL decay fits from 465 nm excitation experiments were removed from Table 4. for simplicity and because they generally fit to similar lifetimes and fractional amplitudes as the PL traces from the 457 nm excitation experiments. The 375 nm PL traces at all emission energies were able to fit to a double exponential decay while the 457 nm PL traces would only fit using a triple exponential decay to publishable standards ($0.9xx < \chi^2 > 1.1xx$). The two PL lifetimes from 375 nm excitations were approximately 0.8 ns and 2 ns while the three PL lifetimes from 457 nm excitation are

approximately 0.5 ns, 1.0 ns, and 2.7 ns, though there are clear lifetime differences between PL lifetimes at various emissions, especially between 640 nm PL decays and 680 nm PL decays. The fitted PL lifetimes (τ_x) after exciting to 375 nm at all detected emission wavelengths are approximately twice as long (τ_1~ 0.8 ns, τ_2~ 2 ns) compared the PL decays after exciting to 457 nm (τ_1~ 0.4 ns, τ_2~ 1 ns). The amplitude-averaged PL lifetimes at every detected emission wavelength and excitation energy were calculated.[138] Surprisingly, the average PL lifetimes over these dynamically ranging experimental parameters varies from 1.0 ns to 1.4 ns, and they appear largely indistinguishable from one another within error. However, we believe this is a function of the short lifetime component and not a reflection of photophysical similarities.

Table 4: Fitted PL lifetimes (τ_x), fractional amplitudes (a_x), and average PL lifetimes ($<\tau_{avg}>$) of the monomer sample.

	Em: 640 nm		Em: 680 nm		Em: 745 nm	
	Ex: 375 nm	Ex: 457 nm	Ex: 375 nm	Ex: 457 nm	Ex: 375 nm	Ex: 457 nm
a_1	0.56 (±0.02)	0.18(±0.09)	0.91 (±0.01)	0.24 (±0.04)	0.84 (±0.01)	0.1 (±0.2)
a_2	0.444 (±0.008)	0.40 (±0.01)	0.09 (±0.03)	0.632 (±0.009)	0.16 (±0.02)	0.65 (±0.01)
a_3	NA	0.416 (±0.007)	NA	0.12 (±0.01)	NA	0.278 (±0.009)
τ_1 (ns)	0.78 (±0.01)	0.24 (±0.03)	0.87 (±0.01)	0.54 (±0.02)	0.86 (±0.01)	0.40 (±0.08)
τ_2 (ns)	2.07 (±0.01)	1.14 (±0.02)	2.03 (±0.03)	1.083 (±0.008)	2.12 (±0.02)	1.00 (±0.01)
τ_3 (ns)	NA	2.49 (±0.01)	NA	3.00 (±0.03)	NA	2.71 (±0.03)
$<\tau_{avg}>$ (ns)	1.3 (±0.2)	1.5 (±0.2)	1.0 (±0.2)	1.2 (±0.3)	1.1 (±0.2)	1.4 (±0.3)

Monomer steady-state emission spectra reveal a broad emission for wavelengths < 500 nm, which is qualitatively similar to published PPE oligomer PL spectra.[121, 122] We hypothesized that this broad emission originates from the PPE substituents. To test this hypothesis, we measured 440 nm and 490nm PL decays by directly exciting monomer transitions with 375 nm light. The 440 nm and the 490 nm PL decays have a high degree of overlap (Fig. 25(d), black and

grey traces), indicating that these emissive states had similar origins and decays after originating in the PPE sidechain.

The monomer was evaluated using broadband TA spectroscopy to directly monitor radiative and nonradiative decay with high temporal resolution (~300 fs). All TA measurements were collected exciting at 515 nm to ensure that the PPE sidechains were not directly excited. However, the optical absorption coefficient of the monomer is extremely weak at 515 nm (see Fig. 23(a)). The pathways we access at this excitation energy are unclear. We may be exciting into the Soret band or the Q-bands. Figure 25(a) shows the emission spectrum collected after exciting the sample with 520 nm light with two distinct emission peaks at 568 and 681 nm. The excited state spectrum (Δt=1.5 ps), and the ground state absorbance spectrum of the monomer are also shown. Shortly after photoexcitation, we observe a positive feature centered at 680.4 nm overlapped with a broad photoinduced absorption (PIA) from 550 nm – 800 nm. There are fine features in the PIA near 558, 604, and 753 nm. The 604 nm peak originates from the Ramen C-H stretch of the DMF solvent. The 753 nm feature energetically matches with previously observed red Q-band emission (see Fig. 23(b)). The transmissive feature around 680 nm is likely a convolution of ground state bleaching, spontaneous emission, and stimulated emission. For convenience, we will refer to the 680 nm feature as the “transmissive peak”.

Excited state spectra before, during photoexcitation, and at various time delays relative to photoexcitation are shown in Fig. 25(b). There appears to be little relaxation in any absorptive or transmissive feature. Averaged kinetic traces were taken from the transmissive peak (681 nm - 691 nm), blue PIA (640 nm - 650 nm) feature, and red PIA (767 nm - 777 nm) feature and are shown in Fig. 25(c). The transmissive and red PIA kinetics were fit with a single exponential

with an X offset. A y-offset, fractional amplitude, and single lifetime component of the transmissive peak decay were 0.942(±0.001), 0.063(±0.003), and 146(±17) ps, respectively. The small fractional amplitude coefficient indicates that a large portion of the excited states contributing to the long-lived transmissive feature have long lifetimes (>1 ns) that cannot be resolve in the presented kinetic decays. The strong pre t0 signal (Fig 25(b), black trace) suggests that these transmissive states still exist 1 μs after photoexcitation. A y-offset, fractional amplitude, and single lifetime component of 0.780(±0.001), 0.171(±0.004), and 53(±3) ps, respectively, were found to fit the red PIA decay kinetics. Attempts were made to fit the red PIA decay to a double exponential decay (with a y-offset) using a positive and negative fractional amplitude coefficient to model both the initial signal decay at shorter times (<100 ps) and the small signal growth at longer times (>200 ps), respectively. However, the best fit using this model resulted in a y-offset of 0.80(±0.03), a positive fractional amplitude and corresponding lifetime of 0.120(±0.007) and 71(±3) ps, and a negative fractional amplitude and corresponding lifetime of 0.05(±0.01) and 700(±1100) ps. The large error of the 700 ps lifetime component and the small fractional amplitude of this fit indicate that this model is not appropriate for the decay processes occurring in this specific wavelength region. The blue PIA was fit to a double exponential with a y-offset. The resulting fit coefficients were 0.34(±0.01) for the y-offset, 0.120(±0.007) and 23(±3) ps for the initial fractional amplitude and decay lifetime, and 0.53(±0.01) and 577(±35) ps for the second fractional amplitude and decay lifetime.

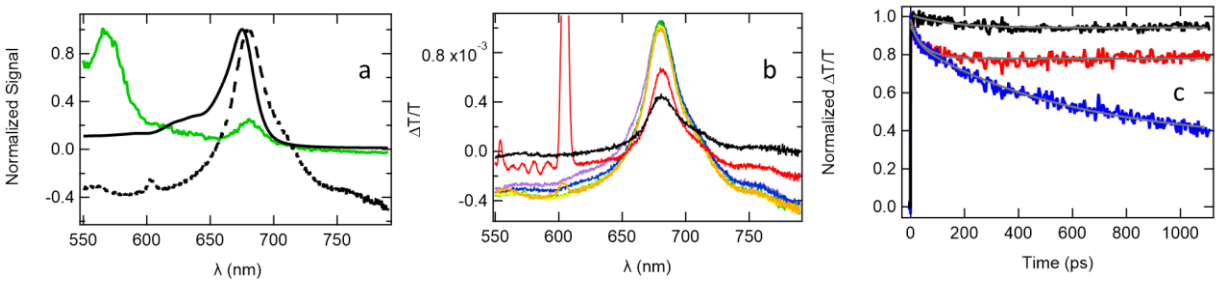

Figure 25: An (a) overlay of the monomer ground state absorption (solid black trace), 520 nm emission spectrum (green trace), and excited state spectra (Δt=1.5 ps, dotted black trace). Monomer (b) excited state spectra at various time delays: pre t0 (black), t0 (red), 0.5 (orange), 1.5 (yellow), 5 (green), 100 (blue), and 1000 (purple) ps. Averaged monomer TA (c) kinetics from the red PIA (red), blue PIA (blue), and transmissive peak (black) features with the fits shown in grey.

Aggregate Steady-State Characterization

The ground-state absorption spectrum of the aggregate is shown in Fig. 26(a), which blue arrows indicating specific features reported in the text. There is a noticeable absorption peak around 460 nm, corresponding to Soret band transitions. There is a slight feature near 586 nm and a broad absorption feature centered around 662 nm with noticeable fine features around 654 and 678 nm.

To simplify the PL comparison between the monomer and aggregate, we used identical PL parameters catered to the monomer sample. The aggregate steady-state emission spectra are shown in Fig. 26(b) after exciting with 450 nm (orange) and 470 nm (red) excitations. The emission spectra have three noticeable emission peaks near 563, 647, and 669 nm. The blue arrows point to the transitions mentioned above. Excitation spectra are shown in Fig. 26(c). The 640 nm excitation spectrum peaks near 455 nm, while the 680 and 745 nm emission spectra peak near 462 nm. The energetic difference between the peak excitations when detecting 640 nm and

680 nm emission wavelengths (green vs blue peaks, Fig. 26) is approximately 333 cm^{-1}, which is approximately 420 cm^{-1} less than the split seen in the monomer sample.

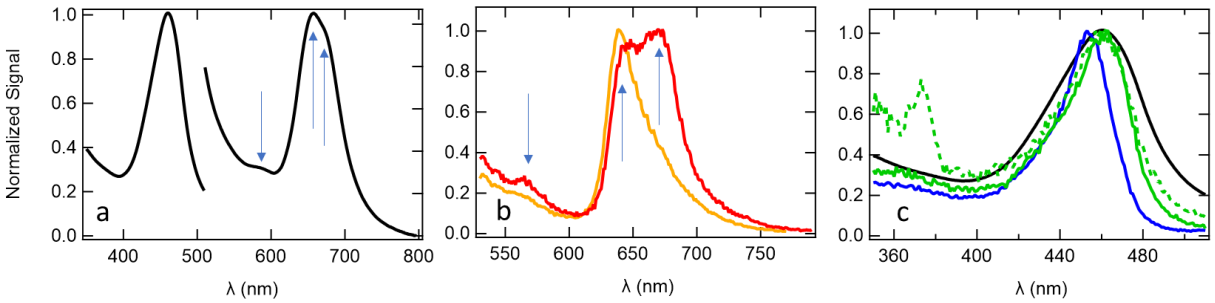

Figure 26: The (a) ground state absorption of the aggregate (black trace) and the (b) emission spectra from 450 nm (orange trace) and 470 nm (red trace) energy excitations with blue arrows pointing to the transitions mentioned above. The (c) excitation spectra resulting from 640 nm (blue trace), 680 nm (solid green trace), and 745 nm (dotted green trace) emission with the overlayed ground state absorption spectra (black trace). Blue arrows indicate the features discussed in the text.

Aggregate Time-Resolved Characterization

The time-resolved PL decays of the aggregate were taken using the same experimental parameters used for the monomer and are shown in Fig. 27. Panels a-c compare PL decays from various excitation energies at a particular detected emission. Due to the relatively low quantum yield of the aggregate, collecting PL decays using a 465 nm photoexcitation was only feasible when detecting 680 nm emission wavelengths, which is why there is only a red decay trace in panel b. The PL decays were fit using an exponential decay and the instrument response function. The amplitude-average PL lifetimes were calculated from these fits and are given in Table 5. The amplitude average lifetimes, regardless of the excitation energy or detected emission, fall between 0.9 ns to 1.3 ns and appear relatively similar within the calculated error of ~0.25 ns. While the traces are not identical, the PL decays appear more homogenous compared to

the PL traces seen after exciting the monomer with 375 nm and 457 nm light.

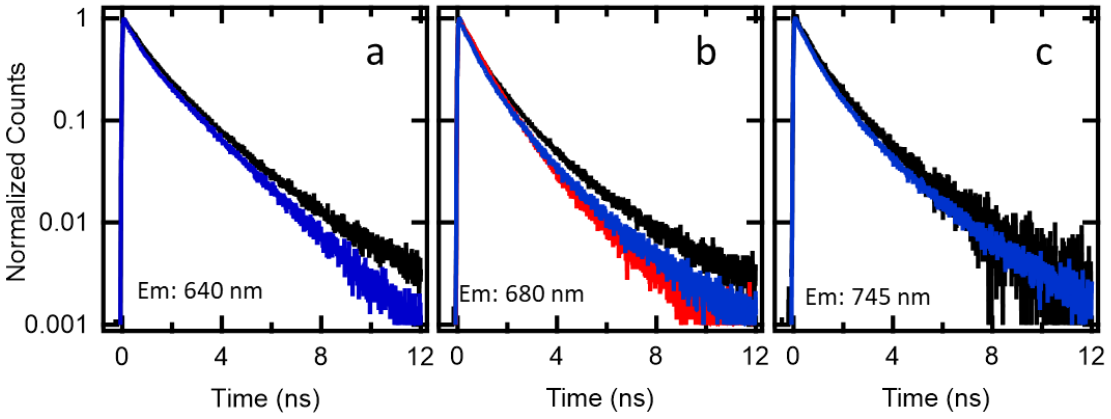

Figure 27: The PL decays of the aggregate samples monitoring (a) 640, (b) 680, and (c) 745 nm emission wavelengths after 375 (black), 457 (blue), and 465 nm (red) energy photoexcitation.

Table 5: The amplitude average PL lifetimes of the aggregate sample after photoexciting the side chain (375 nm) and the higher energy Q-band (457 nm).

Excitation (nm)	$\tau_{640\ nm}$(ns)	$\tau_{680\ nm}$(ns)	$\tau_{745\ nm}$(ns)
375	1.3 (±0.3)	1.0 (±0.3)	1.2 (±0.3)
457	1.1 (±0.2)	0.8 (±0.2)	0.9 (±0.2)

Although PL spectroscopy indicates that the aggregate is weakly emissive, the PL may arise from the low concentration of monomers in equilibrium with the aggregates. Therefore, to directly probe the excited-state dynamics of the aggregate, we next turned to TA spectroscopy. Figure 28(a) compares the aggregate emission spectrum at 520 nm excitation (green), the ground state absorption (black), and the excited-state (dashed black) spectra of the aggregate. Like the monomer, there appears to be a broad PIA feature with a transmissive peak near 670 nm. The 520 nm emission spectrum indicates that spontaneous and stimulated aggregate emission should not contribute to the transmissive pump-probe signal. Therefore, the transmissive peak is likely a convolution of aggregate GSA and monomer emission, though we predict the signal contribution

from emissive monomer decay to be negligible due to the weak signal seen in the 520 nm emission spectra. The evolution of the excited state spectra is shown in Fig. 28(b). Besides the noticeable C-H Raman stretch of the DMF solvent around 610 nm, the excited state spectra are relatively smooth. The decays fit to a double exponential with an X offset, and the amplitude average lifetimes were calculated for the blue PIA, red PIA, and the transmissive peak to be 13(±3) ps, 25(±8) ps, and 8(±3) ps, respectively. The calculated y-offsets of the blue and red PIA decays were 0.014(±0.003) ps and 0.038(±0.008) ps, respectively. However, the calculated y-offset of the transmissive decay is 0.107(±0.002) ps. Considering the fitted traces were first background corrected and normalized, a 0.1 offset is significant and indicates that a long-lived excited state process is contributing to the transmissive pump-probe signal. Similar behavior was seen in the monomer, suggesting this signal may be monomer GSA. The kinetic decays of the transmissive peak and the blue PIA are relatively similar. However, the average lifetime of the red PIA is twice as long as the other decays.

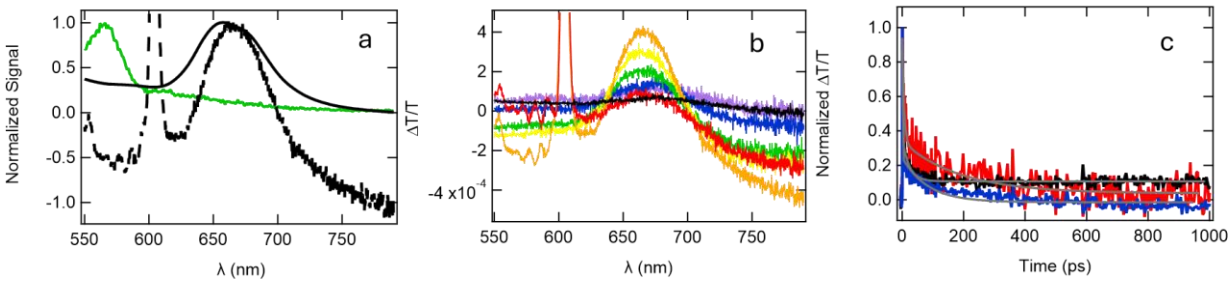

Figure 28: An (a) overlay of the aggregate ground state absorption (solid black trace), 520 nm emission spectrum (green trace), and excited state spectra (Δt=1.5 ps, dotted black trace). Aggregate (b) excited state spectra at various time delays: pre t0 (black), t0 (red), 0.5 (orange), 1.5 (yellow), 5 (green), 100 (blue), and 1000 (purple) ps. Averaged aggregate TA (c) kinetics from the red PIA (red), blue PIA (blue), and transmissive peak (black) features with the fits shown in grey.

Thin Film Monomer and Aggregate Characterization

The ground state absorption spectra of the MF and AF are shown in Fig. 29(a). The peak of the Soret band absorption is at 458.2 nm and 464.3 nm in the AF and MF, respectively, an energy difference of ~286 cm^{-1}. Both the thin film samples were found to be non-emissive when tested with a commercial Fluorimeter. Pump-probe measurements were taken on both films. The excited state spectra taken from 9 separate locations on the AF and MF, respectively, were normalized relative to the highest signal of the transmissive peak 0.5 of after photoexcitation and are shown in Fig. 29 (b). While some variation occurs, qualitatively, these excited-state spectra have the same spectral profiles. The normalized transmissive and blue PIA decays from four locations on the MF and AF, respectively, were averaged and plotted against the standard deviations of the averaged trace (See Fig. 29(c,d)). The average kinetic traces were then fit with a double exponential with an X offset. The blue PIA average lifetimes are 22(±5) ps and 19(±4) ps for the AF and the MF, respectively. The transmissive peak average lifetimes are 33(±6) ps and 30(±6) ps for the AF and the MF, respectively. The average lifetimes and the decay traces both suggest that the excited state dynamics in the thin films are identical, despite the difference in the absorption properties of the material.

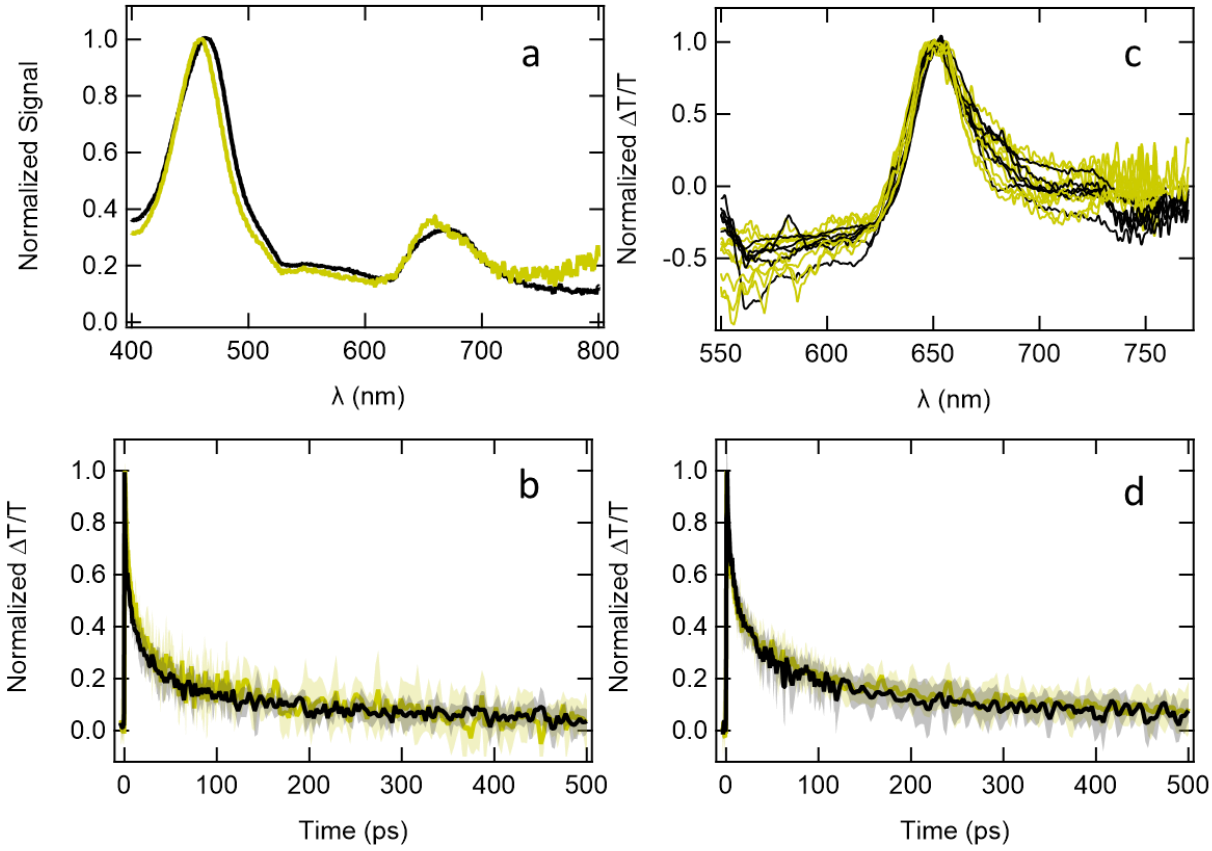

Figure 29: The (a) ground state absorption spectra, (b) pump-probe spectra at Δt=0.5 ps, (c) kinetic blue PIA decay, and the (d) kinetic transmissive decay of the MF (black traces) and AF (yellow traces).

Discussion

Monomer in Solution

Metalated porphyrins have higher symmetry (D_{4H}) than free-base porphyrins (D_{2H}), which can be seen in the chemical structures of metalated and free-base porphyrins shown in Fig. 30(a). This molecular symmetry preserves degeneracy between electronic bands. Metalated porphyrins have three main bands in the optical absorption spectrum, shown in Fig. 30(c). An intense peak from the ground state to Soret band ($E_0 \rightarrow E_2$) transitions, and two lower energy peaks that arise from the $v = 0 \rightarrow 1$ and $v = 0 \rightarrow 2$ bands of the ground state to Q-band

($E_0 \rightarrow E_1$) transitions. Soret band absorptions appear at higher energy wavelengths (<500 nm), and Q-band absorptions appear at lower energy wavelengths (500 nm<λ>750 nm).[129, 130] In free-base porphyrins, the electronic bands are not degenerate. The Soret bands and Q-bands split (Fig. 30(b)), and the absorption spectrum of a free-base porphyrin has five peaks: one high-energy absorption relating to the Soret bands and four Q-bands absorptions. The Soret band split like the Q-bands, but the broad lineshape and energetically similar transitions make the two optical transitions indiscernible (see Fig. 30(d)).[117],[24]

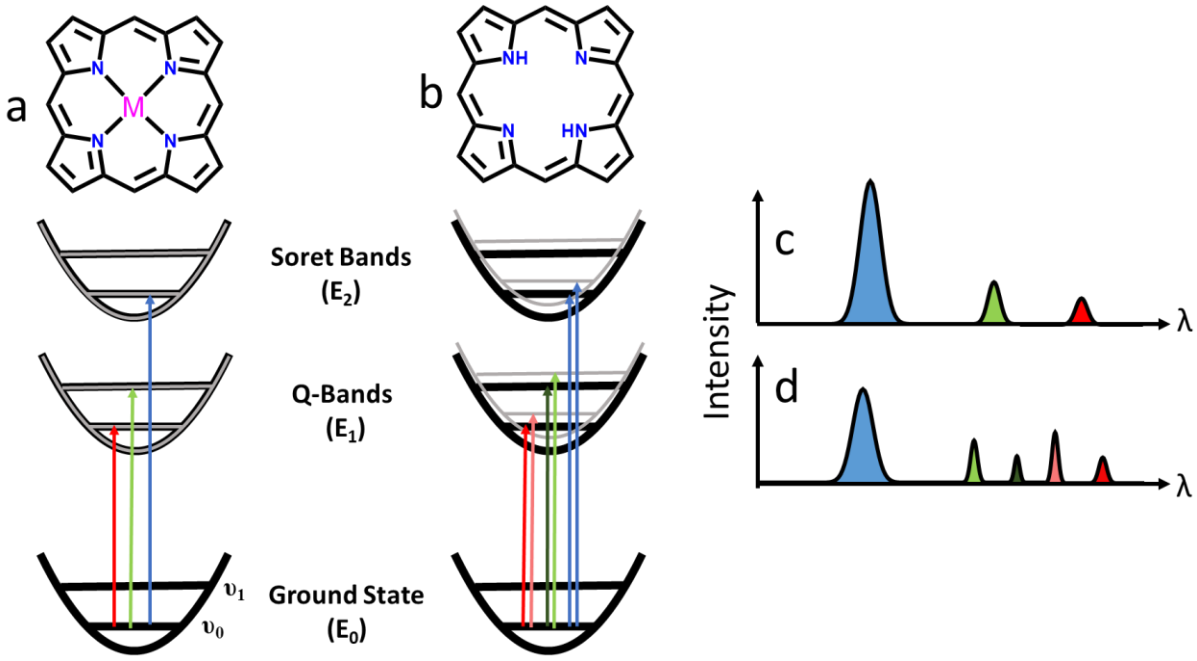

Figure 30: The macrocycle and energy level diagram of a (a) metalated porphyrin and (b) free-base porphyrin with arrows indicating absorption peaks. Representative absorption plots for metalated and free-base porphyrins are given in panels (c) and (d), respectively.

The center of the monomer is a rigid planar ZnP core consisting of four pyrrole rings connected through methine bridges. There are 26 electrons in the planar core with 18 π-electrons within the aromatic ring system called the macrocycle.[24] Light absorption in porphyrins arises from π-π transitions in the macrocycle.[139] The substituents of interest in this work are PPE

substituents with *para* hydroxyethyl groups and *meta* amide-linked decyl chains because they are linked to the porphyrin core through triple bonds

The ZnP monomer studied in this work is metalated, and thus, we would predict the electronic structure to consist of degenerate Soret and Q-bands.[24] However, we observe five absorption peaks in the ground state absorption spectrum. It should be noted that the ground state monomer absorption spectrum is significantly broadened relative to the energy level illustration in Fig. 30, making spectral interpretation difficult. However, the appearance of >3 ground-state absorption peaks (Fig.23(a)) in the monomer and the energetically offset peaks in the excitation spectra (Fig. 23(c)) detected at various emission wavelengths indicates that π-orbital hybridization between the PPE side chains and the porphyrin macrocycle breaks the symmetry of the Soret and Q-bands.

The steady-state monomer measurements were used to construct an energy level diagram, shown in Fig. 31. The vibrational energies of the Q-bands and ground state were determined using the ground-state absorption and emission spectra. The excitation spectra confirmed Soret bands splitting and assigned radiative transitions. For the rest of this chapter, transitions assigned on the left of the band diagram in Fig. 24 will be referenced as “higher energy” transitions from the “higher energy” Soret and Q-bands. Transitions and bands assigned on the right of the band diagram in Fig. 31 will be referenced using the phrase “lower energy.” These titles refer to the energetic effect splitting had on the original energy of the degenerate state.

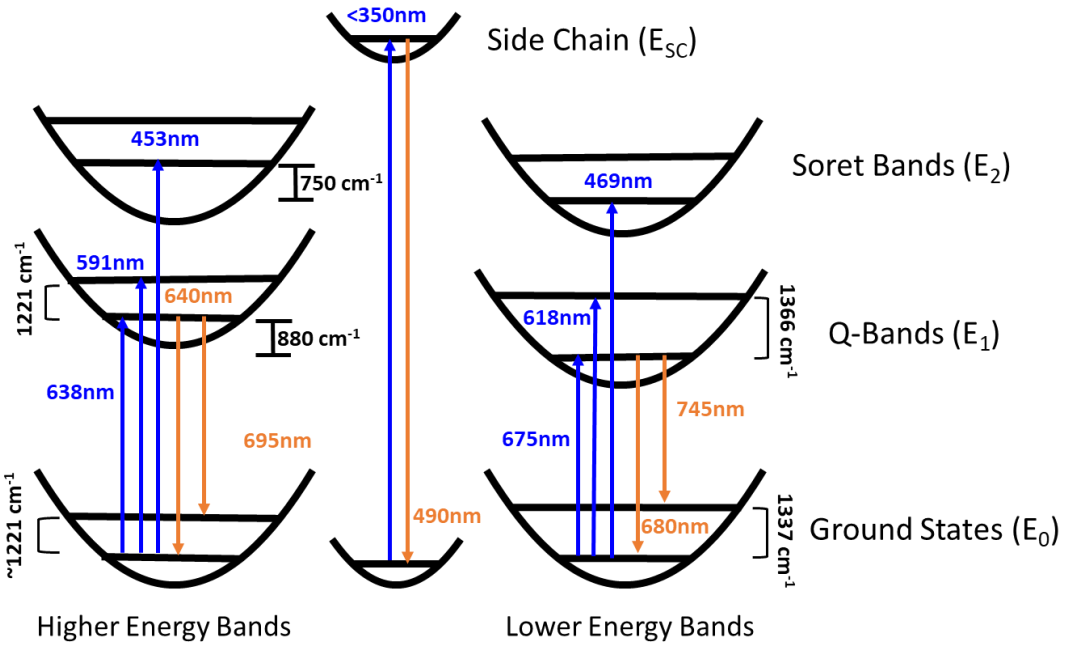

Figure 31: The proposed band diagram for the ZnP monomer. Blue lines represent optical absorptions, and the orange lines represent radiative relaxations. The ground states (E_0), Q-bands (E_1), and Soret bands (E_2) on the left and right sides are referred to as the "higher-energy bands" and "lower-energy bands" throughout Chapter 5.

By formulating a band energy diagram from steady-state absorption and PL measurements, the relationships between the nondegenerate transitions in the porphyrin macrocycle and PPE side chains are easier to visualize. The nuclear rearrangement energy of the higher energy Q-bands is lower than the nuclear rearrangement energy of the lower energy Q-band (51.4 cm^{-1} vs 108.9 cm^{-1}, respectively) and the PL amplitude average lifetimes from higher energy Q-bands decays are larger compared to the lower energy Q-band transitions (457 nm Ex.: 1.5 (±0.2) ps vs 1.2 (±0.3) ps, respectively), which suggesting that the lower energy Q-bands states and ground states are more strongly coupled together. The energetic differences between υ_0 and υ_1 in lower energy ground states and Q-band are 1366 cm^{-1} and 1337 cm^{-1}, respectively. The energetic difference between υ_0 and υ_1 in blue Q-band is 1221 cm^{-1}, which was used to predict

the υ_0 and υ_1 energy difference in the higher energy ground state. Using this assignment, we predict that the high-intensity, asymmetric feature in the PL monomer spectrum is a convolution of two transitions: a weak, higher-energy Q-band vibronic relaxation and a strong, lower-energy Q-band electronic relaxation. The energy differences between vibrational states are on the same order of magnitude observed in other porphyrin systems.[27, 127] The splitting energies between the higher energy and lower energy Soret and Q-bands are approximately 750 cm^{-1} and 880 cm^{-1}, respectively. The smaller splitting energy between the Soret bands indicates improved electronic overlap between the higher-energy and lower-energy Soret bands which would promote internal conversion between the two Soret bands.

While the band diagram is useful for visualizing the origin of electronic transitions, time-resolved spectroscopies help determine rates and branching ratios using decay lifetimes and fractional amplitudes. In the absence of a quencher, the lowest singlet excited state in porphyrins mainly decays through three pathways: fluorescence (f), internal conversion (ic), and intersystem crossing (isc). The lifetime of the singlet excited state (τ_s) decreases as the rates of any of these three processes increase, as shown in Eq. 6.[27]

Eq. 6: $\tau_s = \frac{1}{k_f + k_{ic} + k_{isc}}$

Regardless of excitation or probed emission, the PL decays are similar for ~1 ns before diverging (Fig. 24). Referring to Eq. 6, similar PL decays suggest that the combined fluorescence, intersystem crossing, and internal conversion rates stay consistent between the probed systems. Additionally, higher and lower energy bands must be coupled because exciting the lower energy Soret band transitions (465 nm) results in a higher energy Q-band PL decay (640 nm), and exciting higher energy Soret band transitions (457 nm) results in lower energy Q-

band PL decay (680 nm/745 nm), which corroborate the excitation spectra shown in Fig. 23(c). However, the coupling between the side chains and higher and lower energy ZnP bands appears disproportional. The similarity between the black and red PL traces (Fig. 24(a-c)) suggests a stronger coupling between the PPE bands and the lower energy Q-bands. Overall, the observed PL lifetimes corroborate the proposed monomer band diagram and suggest that there is electronic coupling between the macrocycle and the PPE side chains and nondegenerate Soret and Q-bands.

To monitor how the excited states evolve on a fs-timescale, pump-probe spectra and kinetics were measured and provided evidence of GSB, SE, and PIA. The red PIA and the blue PIA have noticeably dissimilar relaxations. We hypothesized that energy transfer from higher energy Q bands to the lower energy Q bands leads to the measured decay of the blue side of the PIA and the additional lifetime component observed, and the growth of the red side of the PIA signal at later decay times (>200 ps). To test this hypothesis, we fit the red PIA kinetics with a double exponential decay (with a y-offset) using a positive and negative fractional amplitude coefficient. While the best fit from this decay model did not yield physically meaningful fitting components, we hypothesize that wavelength averaging in regions where GSA is present convolutes the detected signal with contributions for two physical processes. The fitted y-offset of ~0.94 and the small fractional amplitude (~0.06) of the fitted 146 nm lifetime component of the transmissive peak decay indicate that there is a long-lived excited state process relating to the GSA of the Q-bands.

A seminal paper by Martin Gouterman outlined the origin of electronic transitions in porphyrins using group theory. In brief, he outlines how the spectra of porphyrins can be discussed using a four-orbital model where the properties of the two highest-filled and two

empty π orbitals can explain the properties of a porphyrin absorption spectrum.[139] Both steady-state and time-resolved optical measurements show that the ZnP macrocycle is hybridized with π PPE orbitals. Referencing Gouterman's model, the orbital energy of the lowest unoccupied PPE π orbital must be similar in energy to the empty π orbitals of the Zn P macrocycle, allowing hybridization to occur.

Solution Phases Monomer vs Aggregate

Aggregating porphyrins dramatically affects the observed optical properties of the materials.[126, 127 140]The aggregates in solution are chemically identical to the monomers. Therefore, any optical differences should be a consequence of aggregation. While the aggregate sample aged for >4 days, the resulting sample is in equilibrium with concentrations of both the monomer and aggregate. While unavoidable, the presence of monomer in the aggregate sample makes determining the photophysical properties of the aggregate extremely difficult, especially for PL spectroscopies. The relatively high quantum yield of the monomer means even small concentrations of monomer in the sample could drastically affect the measured aggregate emission and excitation spectra.

Figure 32(a) compares the normalized ground-state absorption of both the aggregate and the monomer. The aggregate Soret and Q-band absorptions appear broader and blue-shifted compared to the monomer absorptions. The blue spectral shift between the Soret bands of the monomer and aggregate is approximately 303 cm^{-1} indicating the H-like coupling of the ZnP monomer transition dipoles upon aggregation. Figure 32(b) compares the monomer and aggregate emission spectra at 460 nm (solid) and 470 nm (dashed). The observed counts were normalized to the lamp profile during measurements and the optical density of the sample at the

excitation wavelength. Therefore, the relative emission counts are qualitatively indicative of the quantum yield of the material at a particular excitation. When H-aggregation occurs, radiative relaxations become forbidden. Regardless of the excitation energy employed, the aggregate sample exhibits a lower quantum yield compared to the monomer sample, congruent with H-aggregation. The observed emission from the aggregate could arise from residual monomer in the sample or imperfect H-aggregation. Due to the similar behavior and spectral profile of the 640 nm emission spectra in both samples, we hypothesize that this blue Q-band emission is nominally unperturbed by aggregation.

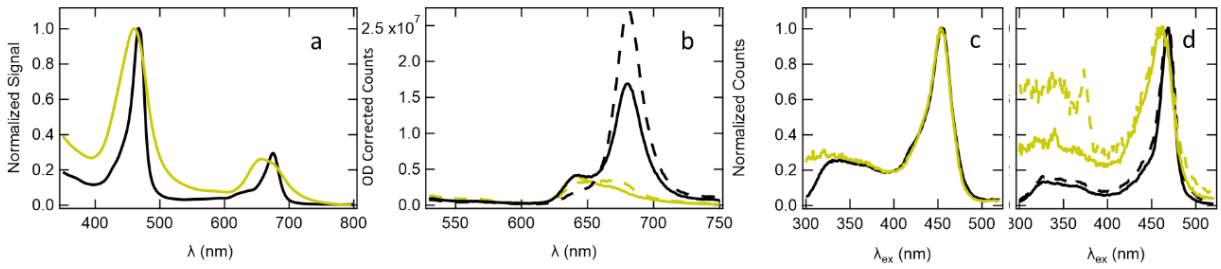

Figure 32: Normalized (a) ground state absorption spectra of the monomer and aggregate. Optical density corrected (b) emission spectra from exciting the samples using 460 nm (solid) and 470 nm (~~dotted~~dashed) light. Excitation spectra detecting (c) 640 nm and (d) 680 nm (solid) and 745 nm (dashed) emitted light. All data from the monomer and aggregate are shown in black and yellow, respectively.

The PL decay kinetics of the monomer are compared to those of the aggregate in Fig. 33. When excited at 375 nm, the PL decays at 640 nm and 745 nm are almost identical (Fig. 33(a) and (c)). In Eq. 6, the single lifetime is a product of nonradiative intersystem crossing and internal conversion, along with radiative fluorescence processes. Similar PL lifetimes indicate that similar excited-state processes are occurring. Because the quantum yield of the H-aggregated monomers is relatively small (Fig. 32(b)), the PL decay in the aggregate sample is likely from monomer emission. However, the PL lifetimes of the monomer and aggregate

samples do not always match, indicating that the electronic structure of the monomer is affected by H-aggregated particles in solution. We also previously observed in Fig. 27 that the PL decays of the aggregate at particular emission energies look relatively similar, a characteristic that was not observed in the monomer (Fig. 24). While the traces are not identical, the increased overlap between PL traces suggests, referring back to Eq. 6, that the sum of the excited state rates are more homogeneous, regardless of what transitions are being excited or what radiative transmissions are being detected. The homogenized excited state behavior may be indicative of improved long-range electronic order in the supramolecular assemblies.[141] Weak noncovalent interactions and dipole-dipole interactions lead to poorly aggregated monomers, which leads to heterogeneous excited state behavior due to local, heterogeneous electronic structures. Improved long-range electronic ordering would lead to more structurally uniform aggregates, fewer local electronic perturbations, and homogenized excited-state behavior as we observed.

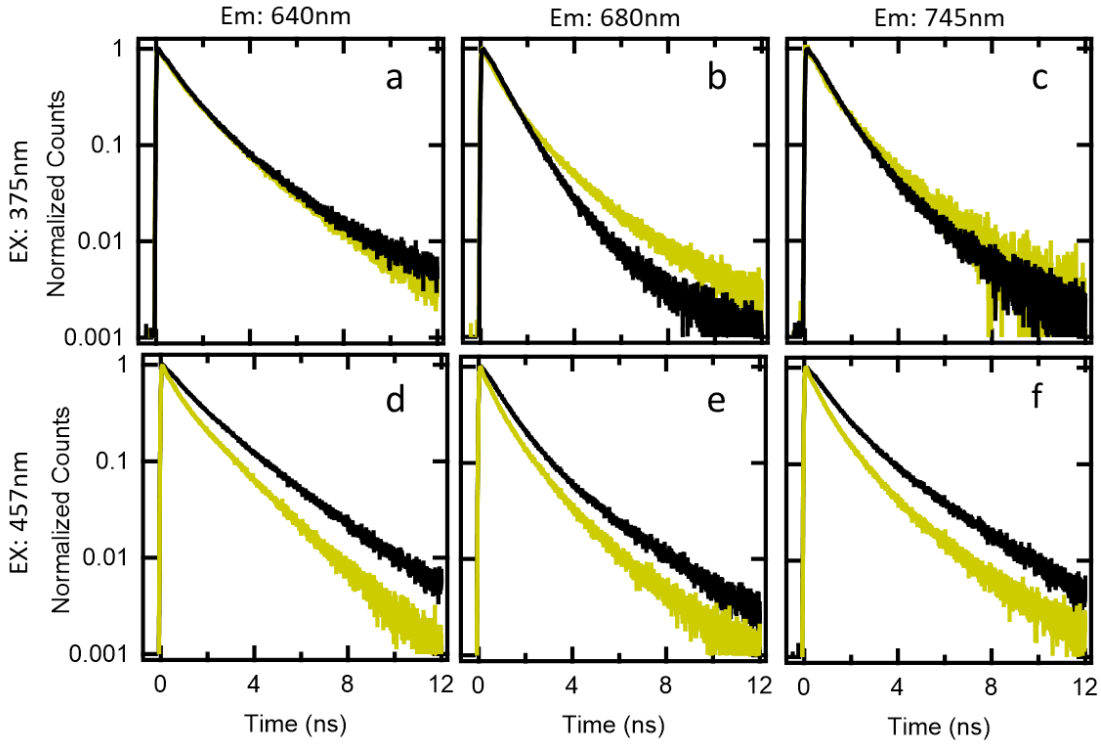

Figure 33: A comparison of the monomer (black) and the aggregate (yellow) PL decays at various emission wavelengths.

The solution-phase TA kinetics monitoring the transient signal change of the transmissive peak, blue PIA, and red PIA are overlayed in Fig. 34. The calculated average lifetimes for all the decay traces are given in the previous monomer and aggregate characterization sections. While each decay trace reflects complicated photophysics and branching ratios, there is one unanimous trend. The excited-state lifetimes of the aggregated ZnP aggregate are always faster compared to the monomeric sample, a characteristic of stronger intermolecular coupling in organic supramolecular assemblies.[11, 15, 142]

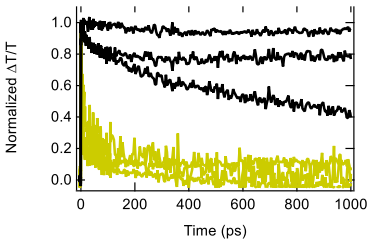

Figure 34: Kinetic TA decays of the monomer (black) and the aggregate (yellow) taken from blue PIA, red PIA, and transmissive pump-probe features.

Solution Phase Aggregate vs Thin Film Monomer

We predicted that the aggregate and the MF materials would have the most similar electronic structure. When preparing the MF, monomers in solution are initially drop-cast onto a substrate. However, evaporating solvent forces the monomers to interact as ZnP crystallites form. Figure 35 monitors the blue shift of the transient pump-probe feature from the monomer sample

(688.1 nm), to the aggregate sample (672.5 nm), to the thin film samples (650.5 nm). Overall, there was a 841 cm^{-1} (104 meV) change in energy, indicating that H-aggregates continue forming as ZnP monomers aggregate and crash out of solution to form thin films.

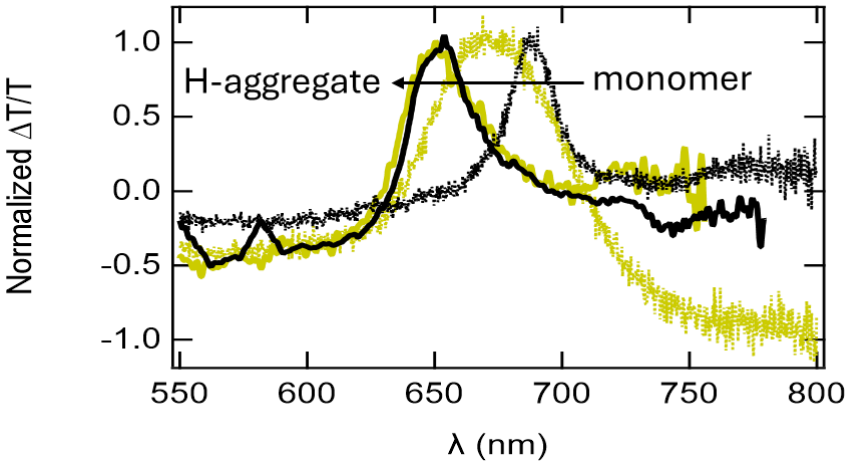

Figure 35: The pump-probe spectra of the liquid phase (dotted) and thin film (solid) monomer (black) and aggregate (yellow) samples. The line direction highlights the spectral blue shift between samples, which is indicative of H-aggregation. The pump-probe spectra were taken ~ 1 ps after photoexcitation.

Thin Film Monomer vs Aggregate

We hypothesized that pre-aggregating the ZnP monomers before solid-state deposition would lead to more structurally homogenous ZnP supramolecular assemblies with improved π-π ordering. However, based on the identical pump-probe decays (~650.5 nm) and spectral decay (average transmissive peak lifetimes: 30(±6) ps and 33(±6) ps, respectively) of the MF and AF (Fig. 29), pre-aggregating the ZnP monomer prior to thin-film drop casting had no apparent effect on the excited state properties of the thin film samples.

Future Work

While great strides have been made in understanding the structure-function relationship between the PPE substituent, aggregation, and thin film formation, several excited-state processes remain ambiguous. I propose the following work to address two questions regarding excited-state dynamics in ZnP.

Question 1: How do the branching ratios of radiative and nonradiative processes change at different excitation energies?

Work 1: I propose measuring the PL decay from higher-energy and lower-energy Q-bands after exciting the monomer and aggregate samples using a 500 nm excitation beam. Exciting samples at 515 nm in TA measurements affect the branching ratios of the decaying excited states, which is seen in this work as additional lifetime components appear in 457 nm excitation PL decays (higher-energy Soret band transitions) compared to the two lifetime components measured in the 375 nm excitation decays (PPE side chain transitions), highlighting the strong coupling effects between electronic states in ZnP-PPE systems. I hypothesize that exciting into the very edge of the Soret band will lead to rapid internal conversion to Q-band states, which will appear as shorter PL lifetimes, particularly from lower energy Q-band transitions due to stronger electronic coupling.

Work 2: I propose measuring pump-probe spectra and kinetics on the monomer, aggregate, TM, and TA samples using a 343 nm pump pulse. We observed that exciting the monomer with 375 nm light results in PL decay from Q-band states. Therefore, exciting into the side chains directly should result in pump-probe spectra with additional spectral features and lifetime components specific to PPE-related excited state dynamics. As mentioned in the introduction, photoexciting PPE oligomers has led to structural and optical changes of the

oligomeric chains, specifically quadratic coupling where photoinduction reduces the torsion of the PPE oligomer, making it more planar.[121] I hypothesize that photoinduction will lead to more planer PPE side chains, transiently improving the electronic overlap between adjacent monomers, which will increase the electronic coupling between the monomers and result in more homogenous excited state decay. When comparing pump-probe data between the 515 nm and 343 nm pump excitations, I predict that the transient electronic will be stronger in the aggregate sample compared to the thin film samples due to the reduced structural confinement of the aggregated monomer in the solution phase compared to the solid state.

Question 2: Are the monomer and aggregate thin films emissive?

Work 3: It was unclear if the lack of detected emission in the MF and AF is a consequence of the sample or instrumental limitations. We predict that PL in the thin film samples is suppressed by H-aggregation, and I propose testing this hypothesis by attempting to measure PL on a newly home-built diffuse reflectance spectrometer. This system was able to collect emissions from graphitic carbon nitride powders, which have low quantum yields (0.5% - 3%, see Ch. 3 and 4).

Conclusions

In summary, the relationship between chemical and intermolecular structure on excited state functionality plays a critical role in applying porphyrins to real-world systems. However, the structure-function relationship between excited-state dynamics and electronic configurations changes from isolated monomers in solution to condensed phase materials. This change is not well understood. In this work, we identified 1) how the sidechains affect the optical properties of a ZnP monomer, 2) how aggregation affects solution phase photophysics, and 3) how the

photophysical properties of the monomer and the aggregate evolve from the solution phase to the solid state using steady-state and time-resolved spectroscopies. First, the optical properties of the solution phase ZnP monomer were compared to traditional porphyrin models to understand the effect of the aromatic PPE side chains on the porphyrin macrocycle. We observed π orbital hybridization between the PPE and porphyrin macrocycle, and that the Soret and Q-band transitions of the ZnP monomer were not degenerate, as predicted for a metalated porphyrin. Second, the optical properties of the ZnP monomer and aggregate in solution were compared. Ground state and excited state absorption spectra of the aggregate showed blue-shifted Soret and Q-band peaks relative to the monomer spectra, suggesting H-aggregation. Finally, the optical properties of the solid film aggregate and monomers (AF and MF) were compared. Signs of H-aggregation can be seen in the pump-probe spectra of both the AF and MF. However, optical comparisons between the AF and MF suggest that pre-aggregating the ZnP monomers before casting thin films has a negligible effect on the observed optical properties.

While there are still significant gaps in understanding the photophysical processes and complicated coupling mechanisms in aggregated porphyrin assemblies, this work is a critical checkpoint to consolidate current findings, challenge initial hypotheses, and inform future directions.

CHAPTER SIX

CONCLUSION

Understanding the effect of electronic perturbations on the structure-function relationship in OFMs is challenging due to strong nuclear coupling and structural heterogeneity. Strong electron-nuclear interactions lead to unfavorable photophysical properties, including rapid charge recombination, low excited-state mobility, and heterogeneous decay. The excited state processes in OFMs can be measured using a combination of steady-state and time-resolved optical measurements, which can inform specific modifications designed to hinder unfavorable photophysical decay. The theory and optical designs of the two time-resolved spectroscopies most commonly employed in this work, liquid-phase transient absorption (TA) spectroscopy and time-correlated single photon counting (TCSPC) spectroscopy, were outlined in Ch. 2.

To better understand the intrinsic photophysical processes in OFM, we elucidated complicated structure-function relationships of graphitic carbon nitride (gCN), an organic photocatalyst, by correlating 22 chemical, structural, and optical properties to the measured photoreduction of Rhd B in Ch. 3. We found that TA lifetimes were the only physical observable that correlated with photochemical activity. Therefore, caution is warranted when reporting photophysical pathways in the context of photochemical reactions if direct photophysical measurements are unavailable.

Due to the intrinsic photophysical limitations of OMFs, works addressed in Ch. 4 and Ch. 5 were designed to mitigate the effects of strong nuclear coupling on the structure-function relationships in gCN and a ZnP monomer assembly. In Ch. 4, we resolved a charge transfer process between the photoexcited gCN and an Ag co-catalyst by employing both steady-state

spectroscopy and liquid-phase TA spectroscopy. This charge transfer process facilitates charge separation, reduces rapid charge recombination rates, and improves photocatalytic behavior. In Ch. 5, a novel ZnP monomer was engineered through the addition of large meta poly(p-phenyleneethynylenes) (PPE) substituents to increase the π-orbital coupling between ZnP monomers. We found that the PPE side chains coupled to the aromatic ZnP macrocycle, breaking the symmetry of the system and leading to nondegenerate optical transitions. Observed blue shifts between the Soret and Q-band absorptions of the monomer vs. the aggregate samples in solution suggest that monomers form H-aggregates, where the transition dipole moments of monomers align parallel to each other. We predicted that pre-aggregating the monomer in solution would lead to more heterogeneous excited-state decays. However, our findings show that pre-aggregation before solid-state deposition does not enhance long-range electronic structure in ZnP thin films.

In conclusion, strong nuclear coupling in OFMs leads to unfavorable, heterogeneous photophysical decay processes that can be mitigated through robust chemical and structural modification. The photophysical effect of modifications can be fundamentally understood by carefully utilizing both steady-state and time-resolved spectroscopies.

APPENDICES

APPENDIX A:

SUPPORTING INFORMATION FOR CHAPTER 3: CORRELATING PHOTOCHEMICAL BEHAVIOR WITH MATERIAL AND OPTICAL PROPERTIES IN GRAPHITIC CARBON NITRIDE

Calculations and Corrections

Photocatalytic study- background corrections

The absorbance spectra taken during the photodegradation measurements were background-subtracted to remove absorbance losses from light scattering off the catalysts. To do this, the absorbance spectrum of the catalyst is matched to the baseline of a "raw" supernatant spectrum by multiplying the catalyst spectrum by a scaler and subtracting a y-offset (Fig. A1(a)). The rescaled catalyst spectrum is then subtracted from the raw supernatant spectrum to generate a baseline-corrected spectrum (Fig. A1(b)). It should be noted that the samples used to collect a representative catalyst spectrum were prepared using the same sonication and centrifuge conditions as the supernatant solutions.

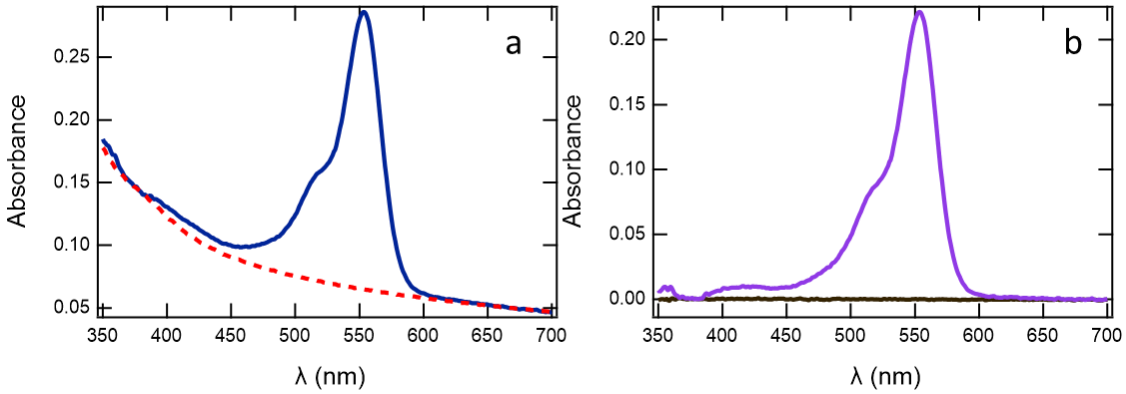

Figure A1: Comparisons of the a) baseline agreement between the raw supernatant spectrum (blue) and the rescaled catalyst spectrum (dashed red) and b) the baseline-corrected spectrum (purple) compared to a blank measurement (grey).

Photoluminescence Quantum Yield (ΦPL) Calculation

The of ΦPL of the samples were calculated using the following Eq. A1[143]:

$$\Phi_{PL} = \Phi_s = \Phi_r \frac{I_s A_r n_s^2}{I_r A_s n_r^2} \qquad \text{Eq. A1}$$

where Φ is the fluorescence quantum yield, I is the integrated area under an emission curve, A is the absorption at the excitation wavelength, and n is the index of refraction. The values corresponding to the sample and the reference are differentiated using s and r subscripts, respectively. Coumarin 151 was used as the reference.[144] The emission spectra used in these calculations have been normalized to a reference silicon diode profile to account for the lamp profile and temporal fluctuation. It should be noted that the ΦPL calculated at 400 nm does not account for the entire emission area due to the experimental constraints of detecting fluorescence near the excitation energy.

Photoreduction Quantum Yield (ΦPR) Calculation

The ΦPR, or apparent quantum yield, was calculated using the following Eq. 2:

$$\Phi_{PR} = \frac{\#reacted\ Rhd\ B\ molecules}{\#photons\ absorped} * \frac{1}{m_{XgCN}} \qquad \text{Eq. A2}$$

where the total number of reacted Rhodamine B (Rhd B) molecules is divided by the total number of photons absorbed by the reaction over the entire 180-minute photocatalytic cycle. The number of reacted Rhd B molecules was calculated using Beer's law and the absorption change between the initial and final absorption spectra from the photocatalytic study. The number of photons was calculated using the power density of the 385 nm LED, and the circumference of the reaction beaker. We assumed that all photons would eventually be absorbed due to the thickness of our reaction (~3in). This assumption may decrease the calculated ΦPR; however, we anticipate this difference to affect each sample measurement similarly and not perturb our ability to compare ΦPR between samples. The ΦPR was normalized to the mass of catalyst (mXgCN) in the reaction in mg.

Additional Figures

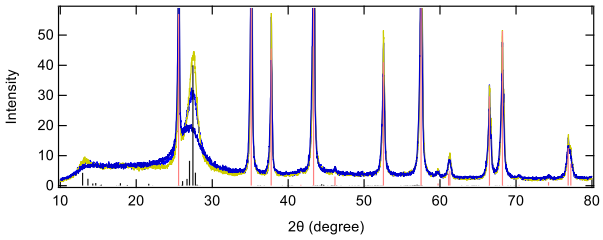

Figure A2: The full XRD patterns of MgCN (yellow), CgCN (green), and UgCN (blue). The red and black lines represent diffraction peaks of corundum (ICDD# 04-014-1368) and orthorhombic gCN (ICDD# 00-066-0813) references from the International Centre for Diffraction Data.

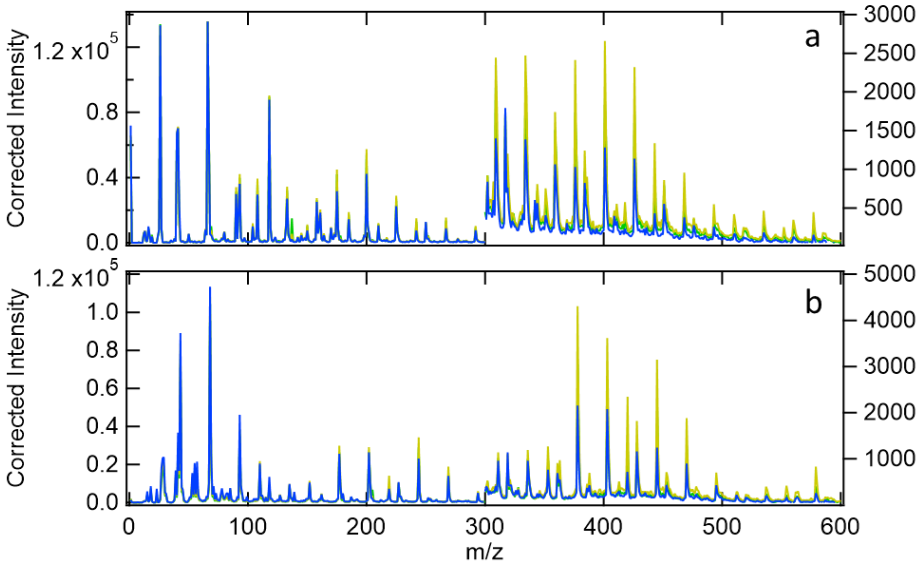

Figure A3: The full (a) negative and (b) positive ToF-SIM spectra of MgCN (yellow), CgCN (green), and UgCN (blue). Two vertical axes are used to exaggerate peaks at higher m/z values (>300 m/z).

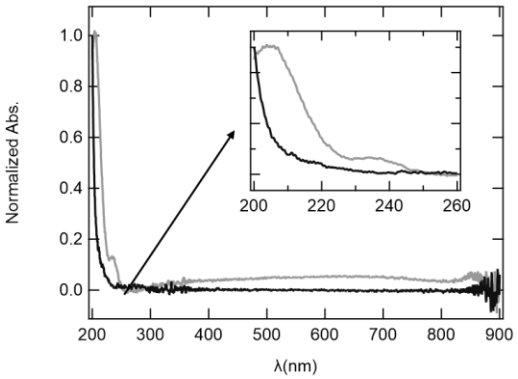

Figure A4: The normalized steady-state absorption of melamine (gray) and urea (black). Both optical samples were prepared by briefly sonicating ~1 mg of powder in 5 mL of 18 μΩ water and diluted with 18 μΩ water to OD ~0.1 in a 1 cm quartz cuvette.

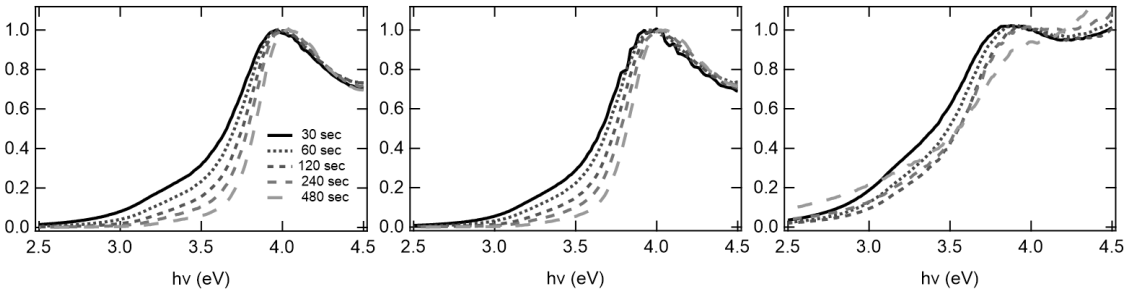

Figure A5: Normalized Tauc plots of MgCN (left), CgCN (middle), and UgCN (right) taken at various centrifugation times (30, 60, 120, 240, and 480 seconds) assuming direct, allowed transitions.

Additional Tables

Table A1: The fifteen top oxygen and non-oxygen-containing species (m/z < 200) with the highest percent contributions. Percent contributions were calculated by dividing the corrected area of each peak by the total corrected area of the entire scan.

Oxygen species	UgCN	CgCN	MgCN	Non-Oxygen species	UgCN	CgCN	MgCN
C_4H_2O-	7.38	6.89	6.51	CN-	7.44	6.84	6.49
$C_6H_2N_2O$-	4.74	4.48	4.29	H-	4.00	3.21	3.21
C_3HNO-	3.62	3.39	3.31	CHN_2-	3.91	3.57	3.47
$C_{12}H_8O_3$-	1.90	2.71	2.35	CN_2-	3.72	3.38	3.26
C_6H_2O-	1.62	1.58	1.63	C_2H-	0.46	0.33	0.38
$C_5H_4N_2O$-	1.49	1.88	1.78	CH-	0.40	0.33	0.36
CNO-	1.26	0.62	0.52	C-	0.27	0.29	0.27
O-	0.53	0.45	0.42	C_3HN_2-	0.25	0.25	0.26
C_6H_2NO-	0.53	0.53	0.56	C_2-	0.24	0.20	0.22
C_4H_2NO-	0.28	0.28	0.27	C_2N-	0.14	0.11	0.12
OH-	0.27	0.20	0.21	$C_{16}H_{11}N$-	0.07	0.11	0.13
$C_7H_9O_5$-	0.25	0.28	0.26	CH_2-	0.06	0.04	0.05
CHNO-	0.08	0.05	0.06	NH-	0.05	0.05	0.05
CHO_2-	0.05	0.05	0.06	C_2HN-	0.04	0.04	0.04
$C_2H_3O_2$-	0.03	0.04	0.05	C_2N_2-	0.04	0.04	0.04

Table A2: The calculated absorption onsets using ground-state transmission spectra assuming both indirect, allowed and direct, allowed transitions. The experiment was run in triplicate. The average and standard deviations of measurements are given at all centrifugation times (30, 60, 120, 240, and 480 seconds) and across all data sets.

		480 seconds		240 seconds		120 seconds		60 seconds		30 seconds		ALL		
		Avg.	STDEV	**Avg**	STDEV	**Avg**	STDEV	**Avg**	STDEV	**Avg**	STDEV	**Avg**	STDEV	Δ
Indirect, allowed	U	**3.3**	0.1	**3.26**	0.07	**3.30**	0.04	**3.20**	0.08	**3.10**	0.06	**3.23**	0.10	0.2
	C	**3.673**	0.004	**3.619**	0.009	**3.558**	0.008	**3.489**	0.004	**3.46**	0.04	**3.56**	0.08	0.2
	M	**3.69**	0.03	**3.64**	0.04	**3.58**	0.04	**3.50**	0.03	**3.42**	0.06	**3.56**	0.10	0.3
Direct, allowed	U	**2.3**	0.6	**2.20**	0.29	**2.26**	0.15	**1.94**	0.31	**1.70**	0.18	**2.07**	0.38	0.6
	C	**3.231**	0.010	**3.115**	0.019	**2.946**	0.010	**2.738**	0.029	**2.41**	0.22	**2.89**	0.31	0.8
	M	**3.22**	0.08	**3.12**	0.07	**2.95**	0.08	**2.71**	0.09	**2.44**	0.11	**2.89**	0.30	0.8

Table A3: The fit-determined parameters of the TA kinetic traces fit using a double exponential with an X offset.

		A1	±A1	A2	±A2	τ1	±τ1	τ2	±τ2	x	τAvg	±τAvg
PIA	MgCN	0.43671	0.0231	0.36786	0.0152	75.207	7.83	720.39	81.3	8.003	370	90
	CgCN	0.40535	0.0157	0.47708	0.00967	78.398	6.19	1083.8	104	3.84778	622	113
	UgCN	0.30862	0.0207	0.48173	0.0128	73.189	9.78	747.61	59.2	7.85945	484	112
PIB	MgCN	0.2112	0.0106	0.54435	0.00354	29.027	2.73	671.56	13.7	8.003	492	78
	CgCN	0.51127	0.038	0.091558	0.0286	1965.4	533	240.99	71	11.8711	1703	730
	UgCN	0.59835	0.0127	0.21731	0.00378	2028.2	87.1	76.359	2.73	7.85937	1508	238

APPENDIX B:

SUPPORTING INFORMATION FOR CHAPTER 4:

ULTRAFAST CHARGE INJECTION IN SILVER-MODIFIED GRAPHITIC CARBON NITRIDE

Materials

Urea (Sigma-Aldrich, >98%), Methanol (Fisher chemical, HPLC grade, 0.2 micron filtered), AgNO3 (Alfa Division, 99.9%) were used as supplied.

Material Synthesis:

gCN preparation

To synthesize bulk gCN, 10 g of ground urea was added to a ceramic crucible and placed in a tube furnace. The furnace was heated to 550 °C using a ramp rate of 5 °C/min and held at temperature for 3 hours. The product was cooled to room temperature and the resulting yellow-colored powder was ground using a mortar and pestle before storage. All heating and cooling processes occurred under an ambient atmosphere. This method was adopted from previously reported methods.[145]

Ag/gCN preparation

Silver metal nanoparticles were deposited onto gCN via photoreduction. [146, 147] 50 mL of millipore water (18.2 MΩ) was added to 50 mg of the above-synthesized gCN in a 100 mL round bottom flask and ultrasonically treated for 3 hrs. To achieve 12.7 wt% Ag/gCN, 10 mg of AgNO3 and 5 mL methanol were added to the suspension and sonicated for an additional 15 minutes. The round-bottom flask was then sealed with a rubber septum and a stir bar. The suspension was stirred and purged with N2 gas for 1 hour. The mixture was then placed in a UV photoreactor and irradiated for 2 hours with continuous stirring. After photoreduction, the reaction mixture was centrifuged at 3900 rpm for 8 minutes and the collected Ag/gCN precipitate was washed 4 times with millipore water (18.2 MΩ) and once with methanol. The washed Ag/gCN was then

dispersed in methanol and set under a gentle nitrogen stream. The remaining light purple Ag/gCN power was dried in a 60 °C oven overnight, transferred to a scintillation vial, and stored in an inert atmosphere when not in use.

Sample Preparation for Optical Measurements

Approximately 2.5 mg of photocatalyst and roughly 5 mL of millipore water were added to a disposable scintillation vial and sonicated for 3 hours. The sonicated mixture was centrifuged at 3500 rpm for 3 minutes and the supernatant was collected. This process was repeated until no visible precipitation was present after centrifuging. The transparent yellow and light purple supernatant of the gCN and Ag-gCN respectively was diluted to the desired optical density using millipore water.

Instrumentation

UV-Vis absorption was measured with a Shimadzu UV-3101PC in a 1 cm quartz cuvette. Spectra were collected every 0.2 nm from 200 nm-800nm.

Steady-state photoluminescence spectra were collected using a Horiba Fluorolog-3 on samples with optical densities near or below 0.1 (1 cm quartz cuvette) at their peak absorption wavelength.

Time-correlated single photon counting (TCSPC) spectroscopy was used to measure the photoluminescence lifetimes of the samples prepared with an optical density of ~0.1 (1 cm quartz cuvette). The excitation beam was derived from a Ti:sapphire oscillator (Coherent Chameleon, 80 MHz, 85 fs pulse duration, 680-1040 nm wavelength range). To generate higher energy excitation wavelengths, the frequency of the initial beam was doubled (345-520 nm

excitations) or tripled (230-346 nm excitations) in a nonlinear crystal. The repetition rate of beam was then reduced to 4 MHz using a Conoptics model 350-10 electro-optic modulator. Long pass filters were placed directly before the detector to prevent detection of scattered excitation photons. Picoquant PicoHarp 300 and FluoTime 200 software were used for data collection. A least squares fitting routine written in Mathematica was used to fit the TCSPC kinetics to a discrete convolution of the measured instrument response function with a modified stretched exponential function, Eq. B1.[115]

$$I(t) = A\ exp\left[1 - \left(1 + \frac{t}{\tau_0}\right)^{\beta}\right] \qquad \text{Eq.B1}$$

Here A, τ_0, β are fitting parameters. The ensemble average lifetime, $\langle\tau\rangle$ is calculated according to,

$$\langle\tau\rangle = \frac{e}{\beta}\Gamma\left(\frac{1}{\beta}, 1\right)\tau_0 \qquad \text{Eq. B2}$$

where $\Gamma(x, b)$ is the incomplete gamma function.[115]

Liquid phase femtosecond transient absorption (TA) spectra were collected on a home built transient absorption instrument. Pump and probe pulses were derived from a commercial ultrafast fiber laser (Coherent Monaco 1035, 40 Watt, 1 MHz, 272 fs pulse duration, 1035±5 nm). The pump beam was modulated with an acousto-optic modulator at 16.125 kHz, coupled onto a 600 mm delay stage, and frequency tripled in a pair of type-I BBO crystals. The resultant 345 nm light was attenuated using neutral density filters and focused onto the sample using a spherical 500 mm focal length aluminum mirror.

The probe was generated by focusing a portion of the 1035 fundamental into an yttrium aluminum garnet (YAG) crystal and collimated using reflective optics. Magic angle polarization was set with a broadband waveplate, and the probe was focused and overlapped with the pump

using a 250 mm FL spherical mirror. Transmitted probe light was coupled into a homebuilt spectrograph based on camera lenses (Nikon, 35 mm FL, F1.8) and imaged onto a high speed line camera synched to collect lines at 62.5 kHz, four times the frequency of the pump modulation, to collect both "pump on" and "pump off" lines (on, on, off, off). The unconventional modulation scheme was used to eliminate systematic noise introduced by the line camera's dual ADCs when subsequent lines are subtracted.

Chemical Reduction

Samples were prepared with an optical density of approximately 0.5 (1 cm quartz cuvette) at peak absorption. A 11 mM sodium borohydride solution (SBH) was prepared directly before use with millipore water (18.2 MΩ). Under continual stirring, 50 μL aliquots of SBH were added to the sample solution and an absorbance spectrum was taken (~3 min collection time) before the addition of the next aliquot. A total of 250 μL of SBH was added, however little spectral change was detected after addition of the first aliquot of SBH.

Calculations and Modeling

Quantum yield calculation: The quantum yields of the samples were calculated using a|e using UV-Vis-IR Spectral Software 1.2 by FluorTools.[148] The software calculates the QY yield of a sample using the following Eq. B3 [143 148]:

$$\Phi_s = \Phi_r \frac{I_s A_r n_s^2}{I_r A_s n_r^2} \qquad \text{Eq. B3}$$

where Φ is the fluorescence quantum yield, I is the integrated area under an emission curve, A is the absorption at the excitation wavelength, and n is the index of refraction. The values

corresponding to the sample and the reference are differentiated using s and r subscripts, respectively. Coumarin 151 was used as the reference.[144] The emission spectra used in these calculations have been normalized to a reference silicon diode profile to account for the lamp profile and temporal fluctuation.

Surface Plasmon model

Under the dipole approximation, the nanoparticle extinction coefficient depends on the dielectric function of both the nanoparticle and the surrounding medium, as given by Eq. B4. [111, 112, 114] Here ε_m is the dielectric constant of the medium surrounding the sphere, λ is the light wavelength, and the real and imaginary parts of the dielectric function of the metal are given by ε' and ε'' respectively.

$$C_{ext} \propto \frac{1}{\lambda} \frac{\varepsilon_m^{3/2} \varepsilon''}{(\varepsilon' + 2\varepsilon_m)^2 + \varepsilon''^2} \qquad \text{Eq. B4}$$

At wavelengths far from the interband resonances, the Drude model provides an accurate description of the wavelength dependent dielectric function, however near resonance, it is necessary to account for contributions from interband transitions. To do so, we use a dielectric function in Eq. B4 that is defined by a linear combination of the experimentally-measured bulk Ag dielectric function and a Drude model that allows for parameterization of particle size dependent scattering, Eq. B5.

$$\varepsilon = \varepsilon' + i\varepsilon'' = \varepsilon_{bulk} - \varepsilon_{Drude}(r = bulk) + \varepsilon_{Drude}(r = 1\ nm) \qquad \text{Eq. B5}$$

Here ε_{bulk} is the measured bulk Ag dielectric function[113], ε_{Drude} is the theoretical Drude dielectric function, which has particle size (r) dependence in the dephasing term, as per Eqs. S6a,b:

$$\varepsilon'_{Drude}(\omega;r) = \varepsilon_{opt} - \frac{\omega_p^2}{\omega^2+\Gamma(r)^2} \qquad \text{Eq. B6a}$$

$$\varepsilon''_{Drude}(\omega;r) = \frac{\omega_p^2\,\Gamma(r)}{\omega^3+\omega\,\Gamma(r)^2} \qquad \text{Eq. B6b}$$

In Eqs. B6a and B6b, ε_{opt} is the high optical dielectric constant (ε_{opt} = 3 was used as a best fit to ε'_{bulk} at λ > 500nm), ω_p is the plasma frequency, and $\Gamma(r) = \Gamma_{bulk} + 3v_f/4r$[149], with v_f the Fermi velocity and Γ_{bulk} = 1/(18 fs)[113].

Additional Figures and Tables

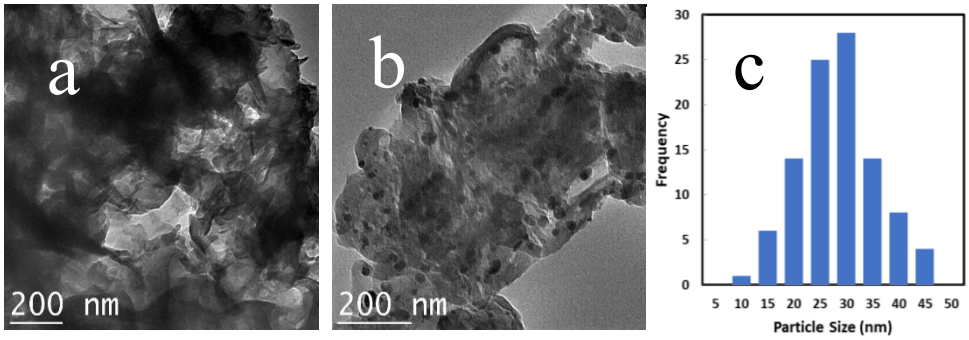

Figure B1: a) TEM images of gCN and b)Ag/gCN and c) Ag particle size distribution.

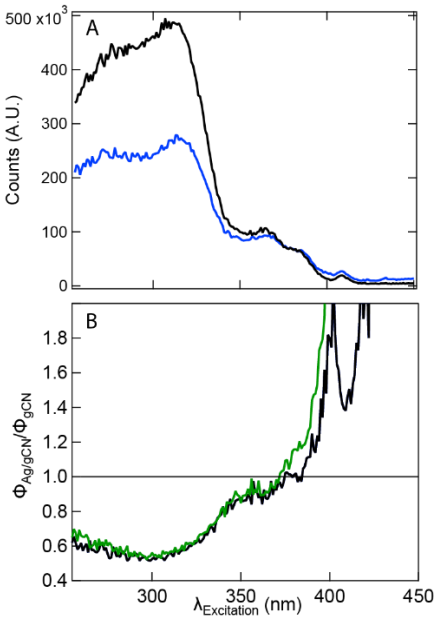

Figure B2: A) Excitation spectra reproduced from Fig. 17. B) Quantum yield ratio at λem = 475 nm (black), obtained by dividing the Ag/gCN excitation spectrum in panel A (blue) by that of gCN (black, panel A). The green trace in panel B shows analogous data for λem = 425 nm.

Table B1: Quantum yields calculated for gCN and Ag/gCN at 315 nm using a coumarin 151 reference.

	As	**Is**	**Ar**	**Ir**	**QY**	**% Quenched**
gCN	0.10	2.7E+08	0.034	1.6E+08	0.0057	
Ag/gCN	0.10	1.2E+08	0.034	1.6E+08	0.0025	56.1

Table B2: Best-fit parameters from stretched exponential fitting of TCSPC data.

			Excitation wavelength (nm)			
			315 nm		360 nm	
			gCN	Ag/gCN	gCN	Ag/gCN
Emission Wavelength (nm)	440 nm	A	0.125 ± 0.001	0.200 ± 0.002	0.114 ± 0.001	0.188 ± 0.002
		τ (ns)	0.263 ± 0.003	0.0076 ± 0.0003	0.222 ± 0.007	0.0075 ± 0.0003
		β	0.436 ± 0.002	0.223 ± 0.001	0.400 ± 0.004	0.254 ± 0.002
	530 nm	A	0.117 ± 0.001	0.148 ± 0.001	0.110 ± 0.001	0.130 ± 0.001
		τ	0.75 ± 0.02	0.075 ± 0.001	0.443 ± 0.009	0.068 ± 0.002
		β (ns)	0.589 ± 0.007	0.348 ± 0.002	0.474 ± 0.004	0.342 ± 0.002

CUMULATIVE REFERENCES CITED

(1) *Functional Organic Materials*. European Journal of Organic Chemistry, 2017. https://chemistry-europe.onlinelibrary.wiley.com/doi/toc/10.1002/(ISSN)1099-0690.Functional-organic-materials (accessed 2025 3/24/2025).

(2) Adachi, C. Third-generation organic electroluminescence materials. *Japanese Journal of Applied Physics* **2014**, *53* (6), Review. DOI: 10.7567/jjap.53.060101.

(3) Yin, R. N.; Lv, J. J. New Functional Organic Materials and Their Photoelectric Applications: A New Open Special Issue of Materials. *Materials* **2022**, *15* (10), Editorial Material. DOI: 10.3390/ma15103444.

(4) Bothe, M.; Pilar Montero-Rama, M.; Viterisi, A.; Cambarau, W.; Stenta, C.; Palomares, E.; Marsal, L. F.; von Delius, M. Second-Generation Azafullerene Monoadducts as Electron Acceptors in Bulk Heterojunction Solar Cells. *Synthesis-Stuttgart* **2018**, *50* (4), 764-771, Article. DOI: 10.1055/s-0036-1591871.

(5) Li, Y.; Guo, Q.; Ding, Z.; Jiang, H.; Yang, H.; Du, W.; Zheng, Y.; Huo, K.; Shaw, L. L. MOFs-Based Materials for Solid-State Hydrogen Storage: Strategies and Perspectives. *Chemical Engineering Journal* **2024**, *485*, Review. DOI: 10.1016/j.cej.2024.149665.

(6) Wood, L. *OLED Market Trends and Revenue Projections by Product Type, Technology, Panel Size, Application, Vertical and Region*. Research and Markets, 2024. https://www.globenewswire.com/news-release/2024/11/27/2988371/28124/en/OLED-Market-Trends-and-Revenue-Projections-by-Product-Type-Technology-Panel-Size-Application-Vertical-and-Region.html (accessed 3/25/2025).

(7) Aly, S. M.; Carraher, C. E. J.; Harvey, P. D. *Introduction to Photophysics and Photochemistry*; John Wiley & Sons, 2010.

(8) Carter, R. L. *Molecular Symmetry and Group Theory*; Wiley, 1997.

(9) Price, M. B.; Hume, P. A.; Ilina, A.; Wagner, I.; Tamming, R. R.; Thorn, K. E.; Jiao, W. T.; Goldingay, A.; Conaghan, P. J.; Lakhwani, G.; et al. Free charge photogeneration in a single component high photovoltaic efficiency organic semiconductor. *Nature Communications* **2022**, *13* (1), Article. DOI: 10.1038/s41467-022-30127-8.

(10) Zhang, C.; Liu, R.; Mak, C. H.; Zou, X.; Shen, H. H.; Leu, S. Y.; Ji, L.; Hsu, H. Y. Photophysics of organic photovoltaic devices: a review. *Journal of Photonics for Energy* **2018**, *8* (2). DOI: 10.1117/1.JPE.8.021001.

(11) Caplins, B. W.; Mullenbach, T. K.; Holmes, R. J.; Blank, D. A. Intermolecular Interactions Determine Exciton Lifetimes in Neat Films and Solid State Solutions of Metal-Free Phthalocyanine. *Journal of Physical Chemistry C* **2015**, *119* (49), 27340-27347, Article. DOI: 10.1021/acs.jpcc.5b09817.

(12) Stevens, M. A.; Silva, C.; Russell, D. M.; Friend, R. H. Exciton dissociation mechanisms in the polymeric semiconductors poly(9,9-dioctylfluorene) and poly(9, 9-dioctylfluorene-co-benzothiadiazole). *Physical Review B* **2001**, *63* (16), Article. DOI: 10.1103/PhysRevB.63.165213.

(13) Wasielewski, M. R. Self-Assembly Strategies for Integrating Light Harvesting and Charge Separation in Artificial Photosynthetic Systems. *Accounts of Chemical Research* **2009**, *42* (12), 1910-1921, Review. DOI: 10.1021/ar9001735.

(14) Bittner, E. R.; Silva, C. Concerning the stability of biexcitons in hybrid HJ aggregates of π-conjugated polymers. *Journal of Chemical Physics* **2022**, *156* (18). DOI: 10.1063/5.0090515.

(15) Verma, S.; Ghosh, A.; Das, A.; Ghosh, H. N. Ultrafast Exciton Dynamics of J- and H-Aggregates of the Porphyrin-Catechol in Aqueous Solution. *Journal of Physical Chemistry B* **2010**, *114* (25), 8327-8334, Article. DOI: 10.1021/jp101643c.

(16) Corp, K. L.; Schlenker, C. W. Ultrafast Spectroscopy Reveals Electron-Transfer Cascade That Improves Hydrogen Evolution with Carbon Nitride Photocatalysts. *J Am Chem Soc* **2017**, *139* (23), 7904-7912. DOI: 10.1021/jacs.7b02869.

(17) Orcutt, E. K.; Varapragasam, S. J.; Andriolo, J. M.; Peterson, Z. C.; Skinner, J. L.; Grumstrup, E. M. Ultrafast Charge Injection in Silver-Modified Graphitic Carbon Nitride. *Acs Applied Materials & Interfaces* **2023**, *15* (12), 15478-15485, Article. DOI: 10.1021/acsami.2c22870.

(18) Mitchell, E.; Law, A.; Godin, R. Interfacial charge transfer in carbon nitride heterojunctions monitored by optical methods. *Journal of Photochemistry and Photobiology C: Photochemistry Reviews* **2021**, *49*. DOI: 10.1016/j.jphotochemrev.2021.100453.

(19) Godin, R.; Wang, Y.; Zwijnenburg, M. A.; Tang, J. W.; Durrant, J. R. Time-Resolved Spectroscopic Investigation of Charge Trapping in Carbon Nitrides Photocatalysts for Hydrogen Generation. *Journal of the American Chemical Society* **2017**, *139* (14), 5216-5224, Article. DOI: 10.1021/jacs.7b01547.

(20) Varapragasam, S. J. P.; Andriolo, J. M.; Skinner, J. L.; Grumstrup, E. M. Photocatalytic Reduction of Aqueous Nitrate with Hybrid Ag/g-C3N4 under Ultraviolet and Visible Light. *Acs Omega* **2021**, *6* (50), 34850-34856. DOI: 10.1021/acsomega.1c05523.

(21) Dong, H. F.; Oganov, A. R.; Zhu, Q.; Qian, G. R. The phase diagram and hardness of carbon nitrides. *Scientific Reports* **2015**, *5*. DOI: 10.1038/srep09870.

(22) Khan, M. A.; Maity, P.; Al-Oufi, M.; Al-Howaish, I. K.; Idriss, H. Electron Transfer of the Metal/Semiconductor System in Photocatalysis. *The Journal of Physical Chemistry C* **2018**, *122* (29), 16779-16787. DOI: 10.1021/acs.jpcc.8b03741.

(23) Merschjann, C.; Tschierlei, S.; Tyborski, T.; Kailasam, K.; Orthmann, S.; Hollmann, D.; Schedel-Niedrig, T.; Thomas, A.; Lochbrunner, S. Complementing Graphenes: 1D Interplanar Charge Transport in Polymeric Graphitic Carbon Nitrides. *Adv Mater* **2015**, *27* (48), 7993-7999. DOI: 10.1002/adma.201503448 From NLM PubMed-not-MEDLINE.

(24) Smith, K. M. *PORPHYRINS AND METALLO PORPHYRINS*; 1975.

(25) Kuzmin, S. M.; Chulovskaya, S. A.; Parfenyuk, V. I. Effect of substituent structure on formation and properties of poly-hydroxyphenyl porphyrin films obtained by superoxide-assisted method. *Electrochimica Acta* **2020**, *342*. DOI: 10.1016/j.electacta.2020.136064.

(26) Mandal, A. K.; Taniguchi, M.; Diers, J. R.; Niedzwiedzki, D. M.; Kirmaier, C.; Lindsey, J. S.; Bocian, D. F.; Holten, D. Photophysical Properties and Electronic Structure of Porphyrins Bearing Zero to Four meso-Phenyl Substituents: New Insights into Seemingly Well Understood Tetrapyrroles. *Journal of Physical Chemistry A* **2016**, *120* (49), 9719-9731, Article. DOI: 10.1021/acs.jpca.6b09483.

(27) Taniguchi, M.; Lindsey, J. S.; Bocian, D. F.; Holten, D. Comprehensive review of photophysical parameters (ε, Φ_f, τ_s) of tetraphenylporphyrin (H₂TPP) and zinc tetraphenylporphyrin (ZnTPP) - Critical benchmark molecules in photochemistry and photosynthesis. *Journal of Photochemistry and Photobiology C-Photochemistry Reviews* **2021**, *46*, Review. DOI: 10.1016/j.jphotochemrev.2020.100401.

(28) Zuehlsdorff, T. J.; Isborn, C. M. Modeling absorption spectra of molecules in solution. *International Journal of Quantum Chemistry* **2019**, *119* (1), Article; Proceedings Paper. DOI: 10.1002/qua.25719.

(29) Abou-Hatab, S.; Carnevale, V.; Matsika, S. Modeling solvation effects on absorption and fluorescence spectra of indole in aqueous solution. *Journal of Chemical Physics* **2021**, *154* (6), Article. DOI: 10.1063/5.0038342.

(30) Stout, B.; Bonod, N. Gustav Mie: the man, the theory. *Photoniques* **2020**, *101*, 22-26. DOI: 10.1051/photon/202010122.

(31) Acquista, C. VALIDITY OF MODIFYING MIE THEORY TO DESCRIBE SCATTERING BY NONSPHERICAL PARTICLES. *Applied Optics* **1978**, *17* (24), 3851-3852, Note. DOI: 10.1364/ao.17.003851.

(32) Hamm, P. *Principles of Nonlinear Optical Spectroscopy: A Practicle Approach*; 2005.

(33) Berera, R.; van Grondelle, R.; Kennis, J. T. M. Ultrafast transient absorption spectroscopy: principles and application to photosynthetic systems. *Photosynthesis Research* **2009**, *101* (2-3), 105-118, Review. DOI: 10.1007/s11120-009-9454-y.

(34) Wahl, M. *Time-Correlated Single Photon Counting*; PicoQuant.

(1) Hamm, P. *Principles of Nonlinear Optical Spectroscopy: A Practicle Approach*; 2005.

(2) Berera, R.; van Grondelle, R.; Kennis, J. T. M. Ultrafast transient absorption spectroscopy: principles and application to photosynthetic systems. *Photosynthesis Research* **2009**, *101* (2-3), 105-118, Review. DOI: 10.1007/s11120-009-9454-y.

(3) Wahl, M. *Time-Correlated Single Photon Counting*; PicoQuant.

(1) *Functional Organic Materials*. European Journal of Organic Chemistry, 2017. https://chemistry-europe.onlinelibrary.wiley.com/doi/toc/10.1002/(ISSN)1099-0690.Functional-organic-materials (accessed 2025 3/24/2025).

(2) Adachi, C. Third-generation organic electroluminescence materials. *Japanese Journal of Applied Physics* **2014**, *53* (6), Review. DOI: 10.7567/jjap.53.060101.

(3) Yin, R. N.; Lv, J. J. New Functional Organic Materials and Their Photoelectric Applications: A New Open Special Issue of Materials. *Materials* **2022**, *15* (10), Editorial Material. DOI: 10.3390/ma15103444.

(4) Bothe, M.; Pilar Montero-Rama, M.; Viterisi, A.; Cambarau, W.; Stenta, C.; Palomares, E.; Marsal, L. F.; von Delius, M. Second-Generation Azafullerene Monoadducts as Electron Acceptors in Bulk Heterojunction Solar Cells. *Synthesis-Stuttgart* **2018**, *50* (4), 764-771, Article. DOI: 10.1055/s-0036-1591871.

(5) Li, Y.; Guo, Q.; Ding, Z.; Jiang, H.; Yang, H.; Du, W.; Zheng, Y.; Huo, K.; Shaw, L. L. MOFs-Based Materials for Solid-State Hydrogen Storage: Strategies and Perspectives. *Chemical Engineering Journal* **2024**, *485*, Review. DOI: 10.1016/j.cej.2024.149665.

(6) Wood, L. *OLED Market Trends and Revenue Projections by Product Type, Technology, Panel Size, Application, Vertical and Region*. Research and Markets, 2024. https://www.globenewswire.com/news-release/2024/11/27/2988371/28124/en/OLED-Market-Trends-and-Revenue-Projections-by-Product-Type-Technology-Panel-Size-Application-Vertical-and-Region.html (accessed 3/25/2025).

(7) Aly, S. M.; Carraher, C. E. J.; Harvey, P. D. *Introduction to Photophysics and Photochemistry*; John Wiley & Sons, 2010.

(8) Carter, R. L. *Molecular Symmetry and Group Theory*; Wiley, 1997.

(9) Price, M. B.; Hume, P. A.; Ilina, A.; Wagner, I.; Tamming, R. R.; Thorn, K. E.; Jiao, W. T.; Goldingay, A.; Conaghan, P. J.; Lakhwani, G.; et al. Free charge photogeneration in a single component high photovoltaic efficiency organic semiconductor. *Nature Communications* **2022**, *13* (1), Article. DOI: 10.1038/s41467-022-30127-8.

(10) Zhang, C.; Liu, R.; Mak, C. H.; Zou, X.; Shen, H. H.; Leu, S. Y.; Ji, L.; Hsu, H. Y. Photophysics of organic photovoltaic devices: a review. *Journal of Photonics for Energy* **2018**, *8* (2). DOI: 10.1117/1.JPE.8.021001.

(11) Caplins, B. W.; Mullenbach, T. K.; Holmes, R. J.; Blank, D. A. Intermolecular Interactions Determine Exciton Lifetimes in Neat Films and Solid State Solutions of Metal-Free Phthalocyanine. *Journal of Physical Chemistry C* **2015**, *119* (49), 27340-27347, Article. DOI: 10.1021/acs.jpcc.5b09817.

(12) Stevens, M. A.; Silva, C.; Russell, D. M.; Friend, R. H. Exciton dissociation mechanisms in the polymeric semiconductors poly(9,9-dioctylfluorene) and poly(9, 9-dioctylfluorene-co-benzothiadiazole). *Physical Review B* **2001**, *63* (16), Article. DOI: 10.1103/PhysRevB.63.165213.

(13) Wasielewski, M. R. Self-Assembly Strategies for Integrating Light Harvesting and Charge Separation in Artificial Photosynthetic Systems. *Accounts of Chemical Research* **2009**, *42* (12), 1910-1921, Review. DOI: 10.1021/ar9001735.

(14) Bittner, E. R.; Silva, C. Concerning the stability of biexcitons in hybrid HJ aggregates of π-conjugated polymers. *Journal of Chemical Physics* **2022**, *156* (18). DOI: 10.1063/5.0090515.

(15) Verma, S.; Ghosh, A.; Das, A.; Ghosh, H. N. Ultrafast Exciton Dynamics of J- and H-Aggregates of the Porphyrin-Catechol in Aqueous Solution. *Journal of Physical Chemistry B* **2010**, *114* (25), 8327-8334, Article. DOI: 10.1021/jp101643c.

(16) Corp, K. L.; Schlenker, C. W. Ultrafast Spectroscopy Reveals Electron-Transfer Cascade That Improves Hydrogen Evolution with Carbon Nitride Photocatalysts. *J Am Chem Soc* **2017**, *139* (23), 7904-7912. DOI: 10.1021/jacs.7b02869.

(17) Orcutt, E. K.; Varapragasam, S. J.; Andriolo, J. M.; Peterson, Z. C.; Skinner, J. L.; Grumstrup, E. M. Ultrafast Charge Injection in Silver-Modified Graphitic Carbon Nitride. *Acs Applied Materials & Interfaces* **2023**, *15* (12), 15478-15485, Article. DOI: 10.1021/acsami.2c22870.

(18) Mitchell, E.; Law, A.; Godin, R. Interfacial charge transfer in carbon nitride heterojunctions monitored by optical methods. *Journal of Photochemistry and Photobiology C: Photochemistry Reviews* **2021**, *49*. DOI: 10.1016/j.jphotochemrev.2021.100453.

(19) Godin, R.; Wang, Y.; Zwijnenburg, M. A.; Tang, J. W.; Durrant, J. R. Time-Resolved Spectroscopic Investigation of Charge Trapping in Carbon Nitrides Photocatalysts for Hydrogen Generation. *Journal of the American Chemical Society* **2017**, *139* (14), 5216-5224, Article. DOI: 10.1021/jacs.7b01547.

(20) Varapragasam, S. J. P.; Andriolo, J. M.; Skinner, J. L.; Grumstrup, E. M. Photocatalytic Reduction of Aqueous Nitrate with Hybrid Ag/g-C3N4 under Ultraviolet and Visible Light. *Acs Omega* **2021**, *6* (50), 34850-34856. DOI: 10.1021/acsomega.1c05523.

(21) Dong, H. F.; Oganov, A. R.; Zhu, Q.; Qian, G. R. The phase diagram and hardness of carbon nitrides. *Scientific Reports* **2015**, *5*. DOI: 10.1038/srep09870.

(22) Khan, M. A.; Maity, P.; Al-Oufi, M.; Al-Howaish, I. K.; Idriss, H. Electron Transfer of the Metal/Semiconductor System in Photocatalysis. *The Journal of Physical Chemistry C* **2018**, *122* (29), 16779-16787. DOI: 10.1021/acs.jpcc.8b03741.

(23) Merschjann, C.; Tschierlei, S.; Tyborski, T.; Kailasam, K.; Orthmann, S.; Hollmann, D.; Schedel-Niedrig, T.; Thomas, A.; Lochbrunner, S. Complementing Graphenes: 1D Interplanar Charge Transport in Polymeric Graphitic Carbon Nitrides. *Adv Mater* **2015**, *27* (48), 7993-7999. DOI: 10.1002/adma.201503448 From NLM PubMed-not-MEDLINE.

(24) Smith, K. M. *PORPHYRINS AND METALLO PORPHYRINS*; 1975.

(25) Kuzmin, S. M.; Chulovskaya, S. A.; Parfenyuk, V. I. Effect of substituent structure on formation and properties of poly-hydroxyphenyl porphyrin films obtained by superoxide-assisted method. *Electrochimica Acta* **2020**, *342*. DOI: 10.1016/j.electacta.2020.136064.

(26) Mandal, A. K.; Taniguchi, M.; Diers, J. R.; Niedzwiedzki, D. M.; Kirmaier, C.; Lindsey, J. S.; Bocian, D. F.; Holten, D. Photophysical Properties and Electronic Structure of Porphyrins Bearing Zero to Four meso-Phenyl Substituents: New Insights into Seemingly Well Understood Tetrapyrroles. *Journal of Physical Chemistry A* **2016**, *120* (49), 9719-9731, Article. DOI: 10.1021/acs.jpca.6b09483.

(27) Taniguchi, M.; Lindsey, J. S.; Bocian, D. F.; Holten, D. Comprehensive review of photophysical parameters (ε, Φ_f, τ_s) of tetraphenylporphyrin (H₂TPP) and zinc tetraphenylporphyrin (ZnTPP) - Critical benchmark molecules in photochemistry and photosynthesis. *Journal of Photochemistry and Photobiology C-Photochemistry Reviews* **2021**, *46*, Review. DOI: 10.1016/j.jphotochemrev.2020.100401.

(28) Xue, C. M.; Jin, S. Exceptionally Strong Electronic Coupling in Crystalline Perylene Diimides via Tuning. *Chemistry of Materials* **2011**, *23* (11), 2689-2692, Article. DOI: 10.1021/cm200413x.

(29) Zámecníková, M.; Nachtigallová, D. Photodynamic behavior of electronic coupling in a N-methylformamide dimer. *Physical Chemistry Chemical Physics* **2015**, *17* (18), 12356-12364, Article. DOI: 10.1039/c4cp04573d.

(30) Holten, D.; Bocian, D. F.; Lindsey, J. S. Probing electronic communication in covalently linked multiporphyrin arrays. A guide to the rational design of molecular photonic devices. *Accounts of Chemical Research* **2002**, *35* (1), 57-69. DOI: 10.1021/ar970264z.

(31) Wu, P.; Wang, J. R.; Zhao, J.; Guo, L. J.; Osterloh, F. E. Structure defects in g-C₃N₄ limit visible light driven hydrogen evolution and photovoltage. *Journal of Materials Chemistry A* **2014**, *2* (47), 20338-20344, Article. DOI: 10.1039/c4ta04100c.

(32) Zuehlsdorff, T. J.; Isborn, C. M. Modeling absorption spectra of molecules in solution. *International Journal of Quantum Chemistry* **2019**, *119* (1), Article; Proceedings Paper. DOI: 10.1002/qua.25719.

(33) Abou-Hatab, S.; Carnevale, V.; Matsika, S. Modeling solvation effects on absorption and fluorescence spectra of indole in aqueous solution. *Journal of Chemical Physics* **2021**, *154* (6), Article. DOI: 10.1063/5.0038342.

(34) Acquista, C. VALIDITY OF MODIFYING MIE THEORY TO DESCRIBE SCATTERING BY NONSPHERICAL PARTICLES. *Applied Optics* **1978**, *17* (24), 3851-3852, Note. DOI: 10.1364/ao.17.003851.

(35) Stout, B.; Bonod, N. Gustav Mie: the man, the theory. *Photoniques* **2020**, *101*, 22-26. DOI: 10.1051/photon/202010122.

(36) Algara-Siller, G.; Severin, N.; Chong, S. Y.; Björkman, T.; Palgrave, R. G.; Laybourn, A.; Antonietti, M.; Khimyak, Y. Z.; Krasheninnikov, A. V.; Rabe, J. P.; et al. Triazine-Based Graphitic Carbon Nitride: a Two-Dimensional Semiconductor. *Angewandte Chemie-International Edition* **2014**, *53* (29), 7450-7455, Article. DOI: 10.1002/anie.201402191.

(37) Ragupathi, V.; Panigrahi, P.; Subramaniam, N. G. Bandgap engineering in graphitic carbon nitride: Effect of precursors. *Optik* **2020**, *202*, Article. DOI: 10.1016/j.ijleo.2019.163601.

(38) Syed, J. A. S.; Zhang, X.-Y.; Ding, W.-J.; Li, A.-D. An overview of the current progress of graphitic carbon nitride and its multifunctional applications. *Journal of Environmental Chemical Engineering* **2022**, *10* (6), Article. DOI: 10.1016/j.jece.2022.108745.

(39) Hamm, P. *Principles of Nonlinear Optical Spectroscopy: A Practicle Approach*; 2005.

(40) Berera, R.; van Grondelle, R.; Kennis, J. T. M. Ultrafast transient absorption spectroscopy: principles and application to photosynthetic systems. *Photosynthesis Research* **2009**, *101* (2-3), 105-118, Review. DOI: 10.1007/s11120-009-9454-y.

(41) Wahl, M. *Time-Correlated Single Photon Counting*; PicoQuant.

(42) Liu, A. Y.; Cohen, M. L. PREDICTION OF NEW LOW COMPRESSIBILITY SOLIDS. *Science* **1989**, *245* (4920), 841-842, Article. DOI: 10.1126/science.245.4920.841.

(43) Lin, H. X.; Wu, J. M.; Zhou, F.; Zhao, X. L.; Lu, P. F.; Sun, G. H.; Song, Y. H.; Li, Y. Y.; Liu, X. Y.; Dai, H. X. Graphitic carbon nitride-based photocatalysts in the applications of environmental catalysis. *Journal of Environmental Sciences* **2023**, *124*, 570-590, Review. DOI: 10.1016/j.jes.2021.11.017.

(44) Merschjann, C.; Tyborski, T.; Orthmann, S.; Yang, F.; Schwarzburg, K.; Lublow, M.; Lux-Steiner, M. C.; Schedel-Niedrig, T. Photophysics of polymeric carbon nitride: An optical quasimonomer. *Physical Review B* **2013**, *87* (20). DOI: 10.1103/PhysRevB.87.205204.

(45) Wang, A. W.; Wang, C. D.; Fu, L.; Wong-Ng, W. N.; Lan, Y. C. Recent Advances of Graphitic Carbon Nitride-Based Structures and Applications in Catalyst, Sensing, Imaging, and LEDs. *Nano-Micro Letters* **2017**, *9* (4). DOI: 10.1007/s40820-017-0148-2.

(46) Wang, X. C.; Maeda, K.; Thomas, A.; Takanabe, K.; Xin, G.; Carlsson, J. M.; Domen, K.; Antonietti, M. A metal-free polymeric photocatalyst for hydrogen production from water under visible light. *Nature Materials* **2009**, *8* (1), 76-80, Article. DOI: 10.1038/nmat2317.

(47) Wang, X. C.; Maeda, K.; Chen, X. F.; Takanabe, K.; Domen, K.; Hou, Y. D.; Fu, X. Z.; Antonietti, M. Polymer Semiconductors for Artificial Photosynthesis: Hydrogen Evolution by Mesoporous Graphitic Carbon Nitride with Visible Light. *Journal of the American Chemical Society* **2009**, *131* (5), 1680-+, Article. DOI: 10.1021/ja809307s.

(48) Walsh, J. J.; Jiang, C.; Tang, J.; Cowan, A. J. Photochemical CO2 reduction using structurally controlled g-C3N4. *Phys Chem Chem Phys* **2016**, *18* (36), 24825-24829. DOI: 10.1039/c6cp04525a From NLM PubMed-not-MEDLINE.

(49) Tu, W. G.; Xu, Y.; Wang, J. J.; Zhang, B. W.; Zhou, T. H.; Yin, S. M.; Wu, S. Y.; Li, C. M.; Huang, Y. Z.; Zhou, Y.; et al. Investigating the Role of Tunable Nitrogen Vacancies in Graphitic Carbon Nitride Nanosheets for Efficient Visible-Light-Driven H₂ Evolution and CO₂ Reduction. *Acs Sustainable Chemistry & Engineering* **2017**, *5* (8), 7260-7268, Article. DOI: 10.1021/acssuschemeng.7b01477.

(50) Xavier, M. M.; Mohanapriya, S.; Divya, K. S.; Adarsh, N. N.; Nair, P. R.; Mathew, S. Exploring The Effect of Precursors of Polymeric Carbon Nitride Nanosheets on their Photo and Electrocatalytic Applications. *Chemistryselect* **2020**, *5* (41), 12679-12689. DOI: 10.1002/slct.202003541.

(51) Yang, L. R.; Liu, X. Y.; Liu, Z. G.; Wang, C. M.; Liu, G.; Li, Q. L.; Feng, X. X. Enhanced photocatalytic activity of g-C3N4 2D nanosheets through thermal exfoliation using dicyandiamide as precursor. *Ceramics International* **2018**, *44* (17), 20613-20619, Review. DOI: 10.1016/j.ceramint.2018.06.105.

(52) Huda, M. N.; Turner, J. A. Morphology-dependent optical absorption and conduction properties of photoelectrochemical photocatalysts for H₂ production: A case study. *Journal of Applied Physics* **2010**, *107* (12), Article. DOI: 10.1063/1.3428957.

(53) Martin, D. J.; Qiu, K. P.; Shevlin, S. A.; Handoko, A. D.; Chen, X. W.; Guo, Z. X.; Tang, J. W. Highly Efficient Photocatalytic H₂ Evolution from Water using Visible Light and Structure-Controlled Graphitic Carbon Nitride. *Angewandte Chemie-International Edition* **2014**, *53* (35), 9240-9245, Article. DOI: 10.1002/anie.201403375.

(54) Dong, H.; Guo, X. T.; Yang, C.; Ouyang, Z. Z. Synthesis of g-C3N4 by different precursors under burning explosion effect and its photocatalytic degradation for tylosin. *Applied Catalysis B-Environmental* **2018**, *230*, 65-76. DOI: 10.1016/j.apcatb.2018.02.044.

(55) Zhang, H.; Yu, A. Photophysics and Photocatalysis of Carbon Nitride Synthesized at Different Temperatures. *The Journal of Physical Chemistry C* **2014**, *118* (22), 11628-11635. DOI: 10.1021/jp503477x.

(56) Starukh, H.; Praus, P. Doping of Graphitic Carbon Nitride with Non-Metal Elements and Its Applications in Photocatalysis. *Catalysts* **2020**, *10* (10). DOI: 10.3390/catal10101119.

(57) Katsumata, H.; Higashi, F.; Kobayashi, Y.; Tateishi, I.; Furukawa, M.; Kaneco, S. Dual-defect-modified graphitic carbon nitride with boosted photocatalytic activity under visible light. *Scientific Reports* **2019**, *9*, Article. DOI: 10.1038/s41598-019-49949-6.

(58) Tong, X. A.; Shou, J. X.; Song, H.; Wang, Y. L.; Huang, L.; Yin, L. S. Ultrafast Electron Transfer from Crystalline g-C₃N₄ to Pt Revealed by Femtosecond Transient Absorption Spectroscopy. *Energy & Fuels* **2022**, *36* (19), 11532-11541. DOI: 10.1021/acs.energyfuels.2c01365.

(59) Sun, H. L.; Wei, K.; Wu, D.; Jiang, Z. F.; Zhao, H.; Wang, T. Q.; Zhang, Q.; Wong, P. K. Structure defects promoted exciton dissociation and carrier separation for enhancing photocatalytic hydrogen evolution. *Applied Catalysis B-Environmental* **2020**, *264*, Article. DOI: 10.1016/j.apcatb.2019.118480.

(60) Niu, P.; Qiao, M.; Li, Y. F.; Huang, L.; Zhai, T. Y. Distinctive defects engineering in graphitic carbon nitride for greatly extended visible light photocatalytic hydrogen evolution. *Nano Energy* **2018**, *44*, 73-81, Article. DOI: 10.1016/j.nanoen.2017.11.059.

(61) Kasap, H.; Caputo, C. A.; Martindale, B. C.; Godin, R.; Lau, V. W.; Lotsch, B. V.; Durrant, J. R.; Reisner, E. Solar-Driven Reduction of Aqueous Protons Coupled to Selective Alcohol Oxidation with a Carbon Nitride-Molecular Ni Catalyst System. *J Am Chem Soc* **2016**, *138* (29), 9183-9192. DOI: 10.1021/jacs.6b04325 From NLM PubMed-not-MEDLINE.

(62) Hong, Z.; Shen, B.; Chen, Y.; Lin, B.; Gao, B. Enhancement of photocatalytic H₂ evolution over nitrogen-deficient graphitic carbon nitride. *Journal of Materials Chemistry A* **2013**, *1* (38), 11754-11761, Article. DOI: 10.1039/c3ta12332d.

(63) Wang, Y.; Liu, X. Q.; Liu, J.; Han, B.; Hu, X. Q.; Yang, F.; Xu, Z. W.; Li, Y. C.; Jia, S. R.; Li, Z.; et al. Carbon Quantum Dot Implanted Graphite Carbon Nitride Nanotubes: Excellent

Charge Separation and Enhanced Photocatalytic Hydrogen Evolution. *Angewandte Chemie-International Edition* **2018**, *57* (20), 5765-5771, Article. DOI: 10.1002/anie.201802014.

(64) Qu, D.; Liu, J.; Miao, X.; Han, M. M.; Zhang, H. C.; Cui, Z.; Sun, S. R.; Kang, Z. H.; Fan, H. Y.; Sun, Z. C. Peering into water splitting mechanism of g-C₃N₄-carbon dots metal-free photocatalyst. *Applied Catalysis B-Environmental* **2018**, *227*, 418-424, Article. DOI: 10.1016/j.apcatb.2018.01.030.

(65) Gumber, S.; Agrawal, S.; Prezhdo, O. V. Excited State Dynamics in Dual-Defects Modified Graphitic Carbon Nitride. *Journal of Physical Chemistry Letters* **2022**, *13* (4), 1033-1041, Article. DOI: 10.1021/acs.jpclett.1c04152.

(66) Song, L. J.; Zheng, Y. J.; Chen, C. F. Sonication-assisted deposition-precipitation synthesis of graphitic C₃N₄/BiOCl heterostructured photocatalysts with enhanced rhodamine B photodegradation activity. *Journal of Materials Science-Materials in Electronics* **2017**, *28* (21), 15861-15869, Article. DOI: 10.1007/s10854-017-7480-7.

(67) Yan, S. C.; Li, Z. S.; Zou, Z. G. Photodegradation of Rhodamine B and Methyl Orange over Boron-Doped g-C₃N₄ under Visible Light Irradiation. *Langmuir* **2010**, *26* (6), 3894-3901, Article. DOI: 10.1021/la904023j.

(68) Honeychurch, K. C. Voltammetric Behaviour of Rhodamine B at a Screen-Printed Carbon Electrode and Its Trace Determination in Environmental Water Samples. *Sensors* **2022**, *22* (12), Article. DOI: 10.3390/s22124631.

(69) Yu, H. J.; Shi, R.; Zhao, Y. X.; Bian, T.; Zhao, Y. F.; Zhou, C.; Waterhouse, G. I. N.; Wu, L. Z.; Tung, C. H.; Zhang, T. R. Alkali-Assisted Synthesis of Nitrogen Deficient Graphitic Carbon Nitride with Tunable Band Structures for Efficient Visible-Light-Driven Hydrogen Evolution. *Advanced Materials* **2017**, *29* (16), Article. DOI: 10.1002/adma.201605148.

(70) Feret, F. R.; Roy, D.; Boulanger, C. Determination of alpha and beta alumina in ceramic alumina by X-ray diffraction. *Spectrochimica Acta Part B-Atomic Spectroscopy* **2000**, *55* (7), 1051-1061, Article; Proceedings Paper. DOI: 10.1016/s0584-8547(00)00225-1.

(71) Rohrer, G. *Structure and Bonding in Crystalline Materials*; Cambridge University Press, 2004.

(72) Li, H.; Wang, L. Z.; Liu, Y. D.; Lei, J. Y.; Zhang, J. L. Mesoporous graphitic carbon nitride materials: synthesis and modifications. *Research on Chemical Intermediates* **2016**, *42* (5), 3979-3998, Review. DOI: 10.1007/s11164-015-2294-9.

(73) Ismael, M.; Wu, Y.; Taffa, D. H.; Bottke, P.; Wark, M. Graphitic carbon nitride synthesized by simple pyrolysis: role of precursor in photocatalytic hydrogen production. *New Journal of Chemistry* **2019**, *43* (18), 6909-6920, Article. DOI: 10.1039/c9nj00859d.

(74) Shirman, R.; Bahuguna, A.; Sasson, Y. Effect of precursor on the hydrogen evolution activity and recyclability of Pd-Supported graphitic carbon nitride. *International Journal of Hydrogen Energy* **2021**, *46* (73), 36210-36220, Article. DOI: 10.1016/j.ijhydene.2021.08.178.

(75) Yuan, S. S.; Zhang, Q. T.; Xu, B.; Liu, S. X.; Wang, J. Q.; Xie, J.; Zhang, M.; Ohno, T. A new precursor to synthesize g-C3N4 with superior visible light absorption for photocatalytic application. *Catalysis Science & Technology* **2017**, *7* (9), 1826-1830, Article. DOI: 10.1039/c7cy00213k.

(76) Cui, L. F.; Fang, Z. R.; Liu, Y. F.; Chen, M. Y.; Yin, C. C.; Wang, J. J.; Wang, Z. G.; Dong, M. D.; Kang, S. F.; Liu, P. Moderate NaNO₂ etching enables easy crystallinity optimization of g-C₃N₄ with superior photoreduction performance. *Inorganic Chemistry Frontiers* **2019**, *6* (5), 1304-1311, Article. DOI: 10.1039/c9qi00113a.

(77) Wen, J.; Li, R. Y.; Lu, R.; Yu, A. C. Photophysics and Photocatalysis of Melem: A Spectroscopic Reinvestigation. *Chemistry-an Asian Journal* **2018**, *13* (8), 1060-1066, Article. DOI: 10.1002/asia.201800186.

(78) Tyborski, T.; Merschjann, C.; Orthmann, S.; Yang, F.; Lux-Steiner, M. C.; Schedel-Niedrig, T. Crystal structure of polymeric carbon nitride and the determination of its process-temperature-induced modifications. *Journal of Physics-Condensed Matter* **2013**, *25* (39), Article. DOI: 10.1088/0953-8984/25/39/395402.

(79) Qiu, P. X.; Xu, C. M.; Chen, H.; Jiang, F.; Wang, X.; Lu, R. F.; Zhang, X. R. One step synthesis of oxygen doped porous graphitic carbon nitride with remarkable improvement of photo-oxidation activity: Role of oxygen on visible light photocatalytic activity. *Applied Catalysis B-Environmental* **2017**, *206*, 319-327, Article. DOI: 10.1016/j.apcatb.2017.01.058.

(80) Negro, P.; Cesano, F.; Casassa, S.; Scarano, D. Combined DFT-D3 Computational and Experimental Studies on g-C₃N₄: New Insight into Structure, Optical, and Vibrational Properties. *Materials* **2023**, *16* (10), Article. DOI: 10.3390/ma16103644.

(81) Li, H. S.; Hu, H. Q.; Bai, C. L.; Bao, C. J.; Guo, F.; Feng, Z. B.; Liu, Y. J. The charge regulation of electronic structure and optical properties of graphitic carbon nitride under strain. *Rsc Advances* **2019**, *9* (13), 7464-7468, Article. DOI: 10.1039/c9ra00396g.

(82) Ye, C.; Li, J.-X.; Li, Z.-J.; Li, X.-B.; Fan, X.-B.; Zhang, L.-P.; Chen, B.; Tung, C.-H.; Wu, L.-Z. Enhanced Driving Force and Charge Separation Efficiency of Protonated g-C3N4 for Photocatalytic O2 Evolution. *ACS Catalysis* **2015**, *5* (11), 6973-6979. DOI: 10.1021/acscatal.5b02185.

(83) Zhang, H.; Chen, Y.; Lu, R.; Li, R.; Yu, A. Charge carrier kinetics of carbon nitride colloid: a femtosecond transient absorption spectroscopy study. *Phys Chem Chem Phys* **2016**, *18* (22), 14904-14910. DOI: 10.1039/c6cp01600f From NLM PubMed-not-MEDLINE.

(84) Meek, G. A.; Baczewski, A. D.; Little, D. J.; Levine, B. G. Polaronic Relaxation by Three-Electron Bond Formation in Graphitic Carbon Nitrides. *Journal of Physical Chemistry C* **2014**, *118* (8), 4023-4032, Article. DOI: 10.1021/jp412305y.

(85) Choudhury, B.; Paul, K. K.; Sanyal, D.; Hazarika, A.; Giri, P. K. Evolution of Nitrogen-Related Defects in Graphitic Carbon Nitride Nanosheets Probed by Positron Annihilation and Photoluminescence Spectroscopy. *Journal of Physical Chemistry C* **2018**, *122* (16), 9209-9219, Article. DOI: 10.1021/acs.jpcc.8b01388.

(86) Xu, J. X.; Ji, Q. J.; Yan, X. M.; Wang, C.; Wang, L. Ni(acac)₂/Mo-MOF-derived difunctional MoNi@MoO₂ cocatalyst to enhance the photocatalytic H₂ evolution activity of g-C₃N₄. *Applied Catalysis B-Environmental* **2020**, *268*, Article. DOI: 10.1016/j.apcatb.2020.118739.

(87) Dong, F.; Zhao, Z.; Xiong, T.; Ni, Z.; Zhang, W.; Sun, Y.; Ho, W.-K. In Situ Construction of g-C₃N₄/g-C₃N₄ Metal-Free Heterojunction for Enhanced Visible-Light Photocatalysis. *Acs Applied Materials & Interfaces* **2013**, *5* (21), 11392-11401, Article. DOI: 10.1021/am403653a.

(88) Rahman, M. Z.; Mullins, C. B. Understanding Charge Transport in Carbon Nitride for Enhanced Photocatalytic Solar Fuel Production. *Accounts of Chemical Research* **2019**, *52* (1), 248-257, Review. DOI: 10.1021/acs.accounts.8b00542.

(89) Kessler, F. K.; Zheng, Y.; Schwarz, D.; Merschjann, C.; Schnick, W.; Wang, X.; Bojdys, M. J. Functional carbon nitride materials — design strategies for electrochemical devices. *Nature Reviews Materials* **2017**, *2* (6). DOI: 10.1038/natrevmats.2017.30.

(90) Savateev, A.; Ghosh, I.; Konig, B.; Antonietti, M. Photoredox Catalytic Organic Transformations using Heterogeneous Carbon Nitrides. *Angew Chem Int Ed Engl* **2018**, *57* (49), 15936-15947. DOI: 10.1002/anie.201802472 From NLM PubMed-not-MEDLINE.

(91) Wang, Y.; Wang, X.; Antonietti, M. Polymeric graphitic carbon nitride as a heterogeneous organocatalyst: from photochemistry to multipurpose catalysis to sustainable chemistry. *Angew Chem Int Ed Engl* **2012**, *51* (1), 68-89. DOI: 10.1002/anie.201101182 From NLM PubMed-not-MEDLINE.

(92) Cao, S.; Low, J.; Yu, J.; Jaroniec, M. Polymeric photocatalysts based on graphitic carbon nitride. *Adv Mater* **2015**, *27* (13), 2150-2176. DOI: 10.1002/adma.201500033 From NLM PubMed-not-MEDLINE.

(93) Fu, J.; Yu, J.; Jiang, C.; Cheng, B. g-C3N4-Based Heterostructured Photocatalysts. *Advanced Energy Materials* **2018**, *8* (3). DOI: 10.1002/aenm.201701503.

(94) Chen, X. F.; Zhang, J. S.; Fu, X. Z.; Antonietti, M.; Wang, X. C. Fe-g-C3N4-Catalyzed Oxidation of Benzene to Phenol Using Hydrogen Peroxide and Visible Light. *Journal of the American Chemical Society* **2009**, *131* (33), 11658-+, Article. DOI: 10.1021/ja903923s.

(95) Zhao, C. X.; Chen, Z. P.; Xu, J. S.; Liu, Q. Q.; Xu, H.; Tang, H.; Li, G. S.; Jiang, Y.; Qu, F. Q.; Lin, Z. X.; et al. Probing supramolecular assembly and charge carrier dynamics toward enhanced photocatalytic hydrogen evolution in 2D graphitic carbon nitride nanosheets. *Applied Catalysis B-Environmental* **2019**, *256*, Article. DOI: 10.1016/j.apcatb.2019.117867.

(96) Wang, W. J.; Yu, J. C.; Shen, Z. R.; Chan, D. K. L.; Gu, T. g-C3N4 quantum dots: direct synthesis, upconversion properties and photocatalytic application. *Chemical Communications* **2014**, *50* (70), 10148-10150, Article. DOI: 10.1039/c4cc02543a.

(97) Maeda, K.; Wang, X. C.; Nishihara, Y.; Lu, D. L.; Antonietti, M.; Domen, K. Photocatalytic Activities of Graphitic Carbon Nitride Powder for Water Reduction and Oxidation under Visible Light. *Journal of Physical Chemistry C* **2009**, *113* (12), 4940-4947, Article. DOI: 10.1021/jp809119m.

(98) Pei, G. X.; Dzade, N. Y.; Zhang, Y.; Hofmann, J. P.; de Leeuw, N. H.; Weckhuysen, B. M. Identification of Photoexcited Electron Relaxation in a Cobalt Phosphide Modified Carbon Nitride Photocatalyst. *Chemphotochem* **2021**, *5* (4), 330-334. DOI: 10.1002/cptc.202000259.

(99) Yue, B.; Li, Q. Y.; Iwai, H.; Kako, T.; Ye, J. H. Hydrogen production using zinc-doped carbon nitride catalyst irradiated with visible light. *Science and Technology of Advanced Materials* **2011**, *12* (3), Article. DOI: 10.1088/1468-6996/12/3/034401.

(100) Zhang, G. G.; Huang, C. J.; Wang, X. C. Dispersing Molecular Cobalt in Graphitic Carbon Nitride Frameworks for Photocatalytic Water Oxidation. *Small* **2015**, *11* (9-10), 1215-1221. DOI: 10.1002/smll.201402636.

(101) Zhao, Z.; Sun, Y.; Dong, F. Graphitic carbon nitride based nanocomposites: a review. *Nanoscale* **2015**, *7* (1), 15-37. DOI: 10.1039/c4nr03008g From NLM Medline.

(102) Ishaq, T.; Yousaf, M.; Bhatti, I. A.; Ahmad, M.; Ikram, M.; Khan, M. U.; Qayyum, A. Photo-assisted splitting of water into hydrogen using visible-light activated silver doped g-C3N4 & CNTs hybrids. *International Journal of Hydrogen Energy* **2020**, *45* (56), 31574-31584, Article. DOI: 10.1016/j.ijhydene.2020.08.191.

(103) Munoz-Batista, M. J.; Fontelles-Carceller, O.; Ferrer, M.; Fernandez-Garcia, M.; Kubacka, A. Disinfection capability of Ag/g-C3N4 composite photocatalysts under UV and visible light illumination. *Applied Catalysis B-Environmental* **2016**, *183*, 86-95, Article. DOI: 10.1016/j.apcatb.2015.10.024.

(104) Paul, K. K.; Giri, P. K.; Sugimoto, H.; Fujii, M.; Choudhury, B. Evidence for plasmonic hot electron injection induced superior visible light photocatalysis by g-C3N4 nanosheets decorated with Ag-TiO2(B) and Au-TiO2(B) nanorods. *Solar Energy Materials and Solar Cells* **2019**, *201*, Article. DOI: 10.1016/j.solmat.2019.110053.

(105) Prasad, C.; Tang, H.; Liu, Q. Q.; Bahadur, I.; Karlapudi, S.; Jiang, Y. J. A latest overview on photocatalytic application of g-C3N4 based nanostructured materials for hydrogen production. *International Journal of Hydrogen Energy* **2020**, *45* (1), 337-379, Review. DOI: 10.1016/j.jhydene.2019.07.070.

(106) Tong, X.; Shou, J.; Song, H.; Wang, Y.; Huang, L.; Yin, L. Ultrafast Electron Transfer from Crystalline g-C3N4 to Pt Revealed by Femtosecond Transient Absorption Spectroscopy. *Energy & Fuels* **2022**. DOI: 10.1021/acs.energyfuels.2c01365.

(107) Wood, A.; Giersig, M.; Mulvaney, P. Fermi Level Equilibration in Quantum Dot−Metal Nanojunctions. *The Journal of Physical Chemistry B* **2001**, *105* (37), 8810-8815. DOI: 10.1021/jp011576t.

(108) Miao, H.; Zhang, G.; Hu, X.; Mu, J.; Han, T.; Fan, J.; Zhu, C.; Song, L.; Bai, J.; Hou, X. A novel strategy to prepare 2D g-C3N4 nanosheets and their photoelectrochemical properties. *Journal of Alloys and Compounds* **2017**, *690*, 669-676. DOI: 10.1016/j.jallcom.2016.08.184.

(109) Pareek, S.; Waheed, S.; Sharma, P.; Karak, S. Structural and optical properties of exfoliated graphene-like carbon nitride into nanosheets and quantum dots. *Materials Characterization* **2020**, *169*. DOI: 10.1016/j.matchar.2020.110646.

(110) Ge, L.; Han, C.; Liu, J.; Li, Y. Enhanced visible light photocatalytic activity of novel polymeric g-C3N4 loaded with Ag nanoparticles. *Applied Catalysis A: General* **2011**, *409-410*, 215-222. DOI: 10.1016/j.apcata.2011.10.006.

(111) Bhui, D. K.; Bar, H.; Sarkar, P.; Sahoo, G. P.; De, S. P.; Misra, A. Synthesis and UV-vis spectroscopic study of silver nanoparticles in aqueous SDS solution. *Journal of Molecular Liquids* **2009**, *145* (1), 33-37. DOI: 10.1016/j.molliq.2008.11.014.

(112) Mulvaney, P. Surface plasmon spectroscopy of nanosized metal particles. *Langmuir* **1996**, *12* (3), 788-800. DOI: 10.1021/la9502711.

(113) Yang, H. H. U.; D'Archangel, J.; Sundheimer, M. L.; Tucker, E.; Boreman, G. D.; Raschke, M. B. Optical dielectric function of silver. *Physical Review B* **2015**, *91* (23), Article. DOI: 10.1103/PhysRevB.91.235137.

(114) Jain, P. K.; Huang, X.; El-Sayed, I. H.; El-Sayed, M. A. Review of Some Interesting Surface Plasmon Resonance-enhanced Properties of Noble Metal Nanoparticles and Their Applications to Biosystems. *Plasmonics* **2007**, *2* (3), 107-118. DOI: 10.1007/s11468-007-9031-1.

(115) Berberan-Santos, M. N.; Bodunov, E. N.; Valeur, B. Mathematical functions for the analysis of luminescence decays with underlying distributions 1. Kohlrausch decay function (stretched exponential). *Chemical Physics* **2005**, *315* (1-2), 171-182. DOI: 10.1016/j.chemphys.2005.04.006.

(116) Kittel, C. *Introduction to Solid State Physics*; 2005.

(117) Kim, B. F.; Bohandy, J. SPECTROSCOPY OF PORPHYRINS

(118) Yatskou, M. M.; Koehorst, R. B. M.; Donker, H.; Schaafsma, T. J. Spectroscopic properties of a self-assembled zinc porphyrin tetramer I. Steady state optical spectroscopy. *Journal of Physical Chemistry A* **2001**, *105* (51), 11425-11431, Article. DOI: 10.1021/jp010410p.

(119) Takehara, Y.; Sakahara, H.; Masunaga, H.; Isogai, S.; Kodaira, N.; Takeda, H.; Saga, T.; Nakajima, S.; Sakata, I. Tumour enhancement with newly developed Mn-metalloporphyrin (HOP-9P) in magnetic resonance imaging of mice. *British Journal of Cancer* **2001**, *84* (12), 1681-1685. DOI: 10.1054/bjoc.2001.1802.

(120) Talanovaite, S.; Poderys, V.; Rotomskis, R.; Ieee. Spectral and Spatial Characteristics of TPPS3 and TPPS₄ Aggregates. In *14th International Conference Nanomaterials:*

Applications & Properties, Riga, LATVIA, Sep 08-13, 2024; 2024. DOI: 10.1109/nap62956.2024.10739762.

(121) Sluch, M. I.; Godt, A.; Bunz, U. H. F.; Berg, M. A. Excited-state dynamics of oligo(p-phenyleneethynylene):: Quadratic coupling and torsional motions. *Journal of the American Chemical Society* **2001**, *123* (26), 6447-6448, Article. DOI: 10.1021/ja0159012.

(122) Duvanel, G.; Grilj, J.; Schuwey, A.; Gossauer, A.; Vauthey, E. Ultrafast excited-state dynamics of phenyleneethynylene oligomers in solution. *Photochemical & Photobiological Sciences* **2007**, *6* (9), 956-963. DOI: 10.1039/b702647a.

(123) Swathi, K.; Sujith, M.; Divya, P. S.; Varghese, P. M.; Delledonne, A.; Huu, D.; Di Maiolo, F.; Terenziani, F.; Lapini, A.; Painelli, A.; et al. From symmetry breaking to symmetry swapping: is Kasha's rule violated in multibranched phenyleneethynylenes? *Chemical Science* **2023**, *14* (8), 1986-1996. DOI: 10.1039/d2sc05206g.

(124) Sandeep, K.; Joseph, K.; Gautier, J.; Nagarajan, K.; Sujith, M.; Thomas, K. G.; Ebbesen, T. W. Manipulating the Self-Assembly of Phenyleneethynylenes under Vibrational Strong Coupling. *Journal of Physical Chemistry Letters* **2022**, *13* (5), 1209-1214. DOI: 10.1021/acs.jpclett.1c03893.

(125) Li, Y.; Han, W.-W.; Liao, M.-X. Spectroscopic and Crystal Structural Analyses of Zinc (II) Tetraphenylporphyrin J-aggregates. *Acta Physico-Chimica Sinica* **2009**, *25* (12), 2493-2500, Article. DOI: 10.3866/pku.Whxb20091217.

(126) Kärnbratt, J.; Gilbert, M.; Sprafke, J. K.; Anderson, H. L.; Albinsson, B. Self-Assembly of Linear Porphyrin Oligomers into Well-Defined Aggregates. *Journal of Physical Chemistry C* **2012**, *116* (37), 19630-19635, Article. DOI: 10.1021/jp306237e.

(127) Zimmermann, J.; Siggel, U.; Fuhrhop, J. H.; Röder, B. Excitonic coupling between B and Q transitions in a porphyrin aggregate. *Journal of Physical Chemistry B* **2003**, *107* (25), 6019-6021, Letter. DOI: 10.1021/jp0340865.

(128) Urbani, M.; Grätzel, M.; Nazeeruddin, M. K.; Torres, T. Meso-Substituted Porphyrins for Dye-Sensitized Solar Cells. *Chemical Reviews* **2014**, *114* (24), 12330-12396. DOI: 10.1021/cr5001964.

(129) Akins, D. L.; Ozcelik, S.; Zhu, H. R.; Guo, C. Fluorescence decay kinetics and structure of aggregated tetrakis(p-sulfonatophenyl)porphyrin. *Journal of Physical Chemistry* **1996**, *100* (34), 14390-14396, Review. DOI: 10.1021/jp961013v.

(130) Verma, S.; Ghosh, H. N. Exciton Energy and Charge Transfer in Porphyrin Aggregate/Semiconductor (TiO₂) Composites. *Journal of Physical Chemistry Letters* **2012**, *3* (14), 1877-1884. DOI: 10.1021/jz300639q.

(131) Humphrey, J. L.; Kuciauskas, D. Contrasting Fe(III) tetrakis(4-hydroxyphenyl)porphyrin excited state dynamics in solution and solid states. *Journal of Physical Chemistry C* **2008**, *112* (5), 1700-1704, Article. DOI: 10.1021/jp076972b.

(132) Luo, L. Y.; Lo, C. F.; Lin, C. Y.; Chang, I. J.; Diau, E. W. G. Femtosecond fluorescence dynamics of porphyrin in solution and solid films:: The effects of aggregation and interfacial electron transfer between porphyrin and TiO₂. *Journal of Physical Chemistry B* **2006**, *110* (1), 410-419, Article. DOI: 10.1021/jp055365q.

(133) Malko, A.; Xu, S.; Wang, H. L.; Kohlman, R.; Smilowitz, L.; Klimov, V.; McBranch, D. W.; Nogues, J. L.; Moreshead, W.; Hagan, D.; et al. Femtosecond to nanosecond characterization of optical limiting mechanisms in power limiting liquids and solids. In *Symposium Z on Thin Films for Optical Waveguide Devices/Symposium PP on Materials for Optical Limiting III held at the 1999 MRS Fall Meeting*, Boston, Ma, 2000

Nov 30-Dec 03, 1999; 2000; Vol. 597, pp 437-445.

(134) Kuzmin, S. M.; Filimonova, Y. A.; Chulovskaya, S. A.; Parfenyuk, V. I. Morphology/potential-dependent electrochromic behaviour of poly (Hydroxyphenyl porphyrin) films. *Materials Chemistry and Physics* **2022**, *275*. DOI: 10.1016/j.matchemphys.2021.125214.

(135) Clavian, L. M.; Kumar, P. C. R.; Kumar, K. V. A.; Rao, D. N.; Shihab, N. K.; Sanjeev, G. Comprehensive Analysis on the Z-Scan Response of Thermally Evaporated CuTPP Thin Films in Terms of H Aggregation and Charge Transfer Dynamics. *Journal of Physical Chemistry C* **2024**, *128* (8), 3460-3472. DOI: 10.1021/acs.jpcc.3c06473.

(136) Karunakaran, V.; Prabhu, D. D.; Das, S.; Varughese, S. Transformation of photophysical properties from solution to solid state in alkoxy-cyano-diphenylacetylene molecules. *Physical Chemistry Chemical Physics* **2015**, *17* (28), 18768-18779, Article. DOI: 10.1039/c5cp02762d.

(137) Afrin, S.; Yang, X. Z.; Morris, A. J.; Grumstrup, E. M. Rapid Exciton Transport and Structural Defects in Individual Porphyrinic Metal Organic Framework Microcrystals. *Journal of the American Chemical Society* **2024**, *146* (7), 4309-4313, Article. DOI: 10.1021/jacs.3c12275.

(138) Sillen, A.; Engelborghs, Y. The correct use of "average" fluorescence parameters. *Photochemistry and Photobiology* **1998**, *67* (5), 475-486. DOI: 10.1562/0031-8655(1998)067<0475:Tcuofp>2.3.Co;2.

(139) Gouterman, M. SPECTRA OF PORPHYRINS. *Journal of Molecular Spectroscopy* **1961**, *6* (1), 138-&, Article. DOI: 10.1016/0022-2852(61)90236-3.

(140) Roeder, B.; Wabnitz, H. TIME-RESOLVED FLUORESCENCE SPECTROSCOPY OF HEMATOPORPHYRIN, MESOPORPHYRIN, PHEOPHORBIDE-A AND CHLORIN-E6 IN ETHANOL AND AQUEOUS-SOLUTION. *Journal of Photochemistry and Photobiology B-Biology* **1987**, *1* (1), 103-113, Article. DOI: 10.1016/1011-1344(87)80010-6.

(141) King, A. J.; Paulino, V. A.; Hollinbeck, S. R.; Tsironi, I.; Maleszka, J. A.; Olivier, J. H.; Grumstrup, E. M. Covalently Tethered Assemblies Improve Energetic Homogeneity and Exciton Transport in Organic Materials. *Acs Materials Letters* **2024**, *6* (4), 1404-1410, Article. DOI: 10.1021/acsmaterialslett.4c00279.

(142) Kakade, S.; Ghosh, R.; Palit, D. K. Excited State Dynamics of Zinc-Phthalocyanine Nanoaggregates in Strong Hydrogen Bonding Solvents. *Journal of Physical Chemistry C* **2012**, *116* (28), 15155-15166, Article. DOI: 10.1021/jp304369r.

(143) Maity, B.; Chatterjee, A.; Seth, D. Photophysics of a Coumarin in Different Solvents: Use of Different Solvatochromic Models. *Photochemistry and Photobiology* **2014**, *90* (4), 734-746. DOI: 10.1111/php.12258.

(144) Duncan, K. M.; Casey, A.; Gobrogge, C. A.; Trousdale, R. C.; Piontek, S. M.; Cook, M. J.; Steel, W. H.; Walker, R. A. Coumarin Partitioning in Model Biological Membranes: Limitations of log P as a Predictor. *Journal of Physical Chemistry B* **2020**, *124* (38), 8299-8308, Article. DOI: 10.1021/acs.jpcb.0c06109.

(145) Qin, J. Y.; Huo, J. P.; Zhang, P. Y.; Zeng, J.; Wang, T. T.; Zeng, H. P. Improving the photocatalytic hydrogen production of Ag/g-C3N4 nanocomposites by dye-sensitization under visible light irradiation. *Nanoscale* **2016**, *8* (4), 2249-2259, Article. DOI: 10.1039/c5nr06346a.

(146) Chan, S. C.; Barteau, M. A. Preparation of highly uniform Ag/TiO2 and Au/TiO2 supported nanoparticle catalysts by photodeposition. *Langmuir* **2005**, *21* (12), 5588-5595, Article. DOI: 10.1021/la046887k.

(147) Faisal, M.; Ismail, A. A.; Harraz, F. A.; Al-Sayari, S. A.; El-Toni, A. M.; Al-Assiri, M. S. Synthesis of highly dispersed silver doped g-C3N4 nanocomposites with enhanced visible-light photocatalytic activity. *Materials & Design* **2016**, *98*, 223-230, Article. DOI: 10.1016/j.matdes.2016.03.019.

(148) *a|e - UV-Vis-IR Spectral Software 1.2, FluorTools*. www.fluortools.com (accessed.

(149) Bohren, C. F.; Huffman, D. R. *Absorption and Scattering of Light by Small Particles*; 1983.